UNIVERSITY OF OKLAHOMA

GRADUATE COLLEGE

COMPACT ANTENNA TEST RANGE FOR MMWAVE METROLOGY APPLICATIONS

A THESIS

SUBMITTED TO THE GRADUATE FACULTY

in partial fulfillment of the requirements for the

Degree of

MASTER OF SCIENCE

By

Elizabeth Joyce
Norman, Oklahoma
2024

Downloaded from SHAREOK. Persistent Handle URL: https://hdl.handle.net/11244/340356

COMPACT ANTENNA TEST RANGE FOR MMWAVE METROLOGY APPLICATIONS

A THESIS APPROVED FOR THE
SCHOOL OF ELECTRICAL AND COMPUTER ENGINEERING

BY THE COMMITTEE CONSISTING OF

Dr. Jorge L. Salazar-Cerreño, Chair

Dr. Hjalti Sigmarsson

Dr. Caleb Fulton

© Copyright by ELIZABETH JOYCE 2024

All Rights Reserved.

Acknowledgments

First and foremost, I would like to thank my parents for their constant encouragement throughout this endeavor and the values they have instilled in me. Without their guidance I would not have achieved as much as I have today.

I would like to extend my deepest gratitude to my advisor, Dr. Jorge Salazar, for providing excellent mentoring and guidance to ensure my personal, academic, and professional success. Your tireless efforts do not go unnoticed. I would also like to thank my other committee members, Dr. Caleb Fulton and Dr. Hjalti Sigmarsson, for their refreshing perspectives and additional mentorship. My committee's expertise and contributions have significantly enriched my experience at the University of Oklahoma.

I would like to sincerely thank the past and present members of the PAARD team including Nafati Aboserwal, Zeeshan Qamar, Nim Ccoillo Ramos, Syed Jehangir, Khuda Burdi, Jorge Alva, Sergio Rodriquez, Mariel Avalos, Alexis Oblitas, Felipe Moncada, Marcelo Moreno, Ryan Jones, Caleb Nelson, and Brian Stade. All of these members have played a part in teaching me about electromagnetics and have proved most helpful in long discussions by providing ideas and advice concerning topics related and unrelated to my project. Outside of the team, I express my gratitude to other friends at the Advanced Radar Research Center (ARRC) who have contributed to making it a home: Rosalind Agasti, Matthew Foster, Skyler Garner, Jacob Sacco, Rabie Abo Taha, Cora DeFrancesco, William Van Houten, Dale Sexton, Jon Knowles, and Alison Sexton. A special shout-out to Matthew Foster, Caleb Nelson, and Alexis Oblitas for their generous support of my project.

Table of Contents

Acknowledgment **iv**

Table of Contents **v**

List of Tables **viii**

List of Figures **ix**

Abstract **xv**

1 Introduction **1**

1.1 Motivation 2

1.2 Literature Review 5

1.2.1 Alternatives to Reflectors in CATRs 7

1.2.2 Minimizing Edge Diffractions 10

1.3 Proposed System 14

1.4 Thesis Outline 15

2 Fundamentals **16**

2.1 IEEE Measurement Requirements 16

2.1.1 Phase 18

2.1.2 Amplitude 20

2.1.3 Quiet Zone Metrics 21

2.2 Compact Range Solution 23

2.2.1 Reflector Mathematical Theory . . . 23
2.2.2 Amplitude Taper and Illumination Trade-off . . . 26
2.2.3 f/D Ratio Trade-off . . . 29
2.2.4 Potential Feed Antennas . . . 35
2.2.5 Feed Antenna Taper . . . 42
2.3 Summary . . . 47

3 Reflector Design and Implementation 49
3.1 Reflector Curvature Design . . . 50
3.2 Reflector Rolled Edge Design . . . 57
3.2.1 2D Design Method . . . 59
3.2.1.1 Elliptical Edge Design Example . . . 63
3.2.1.2 Blended Edge Design Example . . . 66
3.2.2 3D Design Method . . . 69
3.2.2.1 Elliptical Edge Design Example . . . 76
3.2.2.2 Blended Edge Design Example . . . 77
3.3 Reflector Roughness . . . 79
3.3.1 Ruze Equation . . . 86
3.4 Reflector Fabrication . . . 89
3.5 Summary . . . 92

4 Proposed System 94
4.1 Vector Network Analyzer and Frequency Extenders . . . 96
4.2 Positioners . . . 97
4.3 Feed antenna . . . 99
4.4 Probe Antenna . . . 101
4.5 Other Components . . . 101
4.6 Summary . . . 102

5 Tests and Validation **104**

5.1 Copper Taped Reflector Measurements 104

5.2 Silver Painted Reflector Measurements 111

5.3 Summary 115

6 Conclusion **116**

6.1 Summary of Work 116

6.2 Contributions 118

6.3 Future Work 118

List of Tables

1.1 Comparing options of different compact antenna test range types 9

2.1 Horn antenna feeds comparison 40

3.1 Reflector geometry symbol definitions 54
3.2 Common blending types, their equations, order, and constants for Eq. (3.31) 62
3.3 2D surface characteristics 67
3.4 Coordinate system translations 71
3.5 3D surface characteristics 79
3.6 Ruze gain loss calculations 88

4.1 Instrumentation specifications as gathered from [65] and [66] 96

5.1 Average QZ phase and magnitude variation across the measured frequency spectrum for each reflector. The QZ is 12 cm x 10 cm. 115

List of Figures

1.1 Visualization of an emitted signal appearing more planar over distance to allow for the far field distance to be measured 3

1.2 Far field distance (FFD) over antenna under test size for 77 GHz, 100 GHz, and 200 GHz as calculated by (a) Eq. (1.1) and (b) Eq. (1.2). 3

1.3 Various reflector configurations and their respective signal paths after being emitted from the feed [14]. 6

1.4 Common design methods to reduce edge diffractions are shown. (a) Side view of a blended edge reflector and (b) front view of a serrated reflector. . 11

1.5 Field comparison of a feed antenna illuminating (a) a traditional parabolic reflector and (b) a blended edge parabolic reflector to visualize the difference in edge diffractions. 11

1.6 Example CATR reflector created by NSI-MI Technologies, an antenna metrology company [31]. Piece-wise petal-shaped serrations are used. 13

2.1 Illustration of a probe's antenna pattern projection onto the AUT's aperture. 18

2.2 Quiet zone metrics of amplitude and phase as presented in [35]. 22

2.3 Example of a parabolic reflector. The reflector successfully turns the waves emitted from the feed at the focus into plane waves because the distance from the focus to the reflector and back to the aperture plane is equivalent regardless of which section of the parabola is contacted. The line segments $\overline{\mathrm{ABC}}$, $\overline{\mathrm{ADE}}$, and $\overline{\mathrm{AFG}}$ (yellow, blue, and green) are all the same length, meaning a plane wave is present at the aperture plane. 24

2.4 Example of parabolic reflectors with various f/D ratios. The reflector successfully turns the waves emitted from the feed at the focus into plane waves because the distance from the focus to the reflector and back the aperture plane is equivalent regardless of which section of the parabola is contacted. The yellow, green, and blue arrows seen in each reflector example are all the same lengths, meaning a plane wave is present at the aperture plane. 25
2.5 Example of a feed antenna pointed at a reflector and the resulting losses from under illumination and spillover effects. 27
2.6 Spillover efficiency and amplitude taper efficiency for reflectors of various f/D ratios assuming a feed with 10 dB edge taper. 28
2.7 Phase cuts at various distances from the reflector to observe the uniformity of the phase in the quiet one for both Reflector A and Reflector B. 30
2.8 Phase cuts of the quiet zone for Reflector A (top) and Reflector B (bottom) for various distances away from the reflector as simulated by TICRA GRASP. 31
2.9 Variance of phase cuts of the quiet zone for Reflector A and Reflector B across various distances away from the reflector. 31
2.10 Sketched visualization of feed illuminating Reflector A (top) and Reflector B (bottom) to portray the effects of smaller and larger f/D ratios. 32
2.11 Variance of phase cuts of the quiet zone for Reflector A and Reflector B across various distances away from the reflector simulated at 20 GHz and 50 GHz. 34
2.12 Various horn antenna feeds designed for 77 GHz modeled in HFSS: a) pyramidal horn b) dual ridged pyramidal horn c) conical horn d) corrugated conical horn. 35
2.13 Radiation patterns of various horn antenna feeds designed for 77 GHz simulated in HFSS: a) pyramidal horn b) dual ridged pyramidal horn c) conical horn d) corrugated conical horn. 36

2.14 Front-end view of a dual-ridged horn antenna to analyze in the context of a waveguide. (a) Dimensions of dual-ridged horn antenna, including actual length a and effective length a_{eff}. (b) E-field behavior of dual-ridged horn antenna with boundary conditions compounding the energy in the center along the ridges (black arrows indicating electric current induced by boundary conditions.) 38
2.15 Simulated phase patterns of horn antennas in HFSS on cut planes 8 inches wide and 4 inches tall. (a) pyramidal (b) dual-ridged (c) conical and (d) corrugated conical. 41
2.16 (a) Gaussian radiation patterns for feeds of different taper levels. (b) Diagram of reflector showing the definition of subtended angle [42]. 42
2.17 Simulated magnitude and phase-cut patterns of a CATR system with Gaussian feed of various tapering levels. The x-axis is the distance of the vertical cut of the quiet zone in meters. The magnitude varies more with a steeper taper while the phase varies less with a steeper taper. 43
2.18 Simulated magnitude and phase grid cut patterns of a CATR system with Gaussian feed of various tapering levels. The magnitude varies more with a steeper taper (more directive feed antenna) while the phase varies less with a steeper taper. 44
2.19 Variation of phase and magnitude for Gaussian feeds of different taper levels. The variation is calculated over the distance ρ of -0.05 to 0.05 meters which can be observed in Figure 2.17. 46
2.20 Illustration of how feeds with different tapers and beamwidths can impact the compact range set-up. The scenario on the left has a large taper and the setup on the right has a small taper. 47

3.1 Parameters of an offset parabolic reflector, as defined by [42]. 51
3.2 Perspective view of offset parabolic reflector geometry [42]. 51

3.3 Step by-step demonstration of how reflector is constructed in HFSS to demonstrate the elliptical portion of the parabaloid used. 55
3.4 (a) The resulting simulated phase after the feed is placed at the focus and pointed at an angle of ψ_f. The phase becomes linear at a certain point. (b) The resulting simulated phase along the dotted line through the center of the model along the z-axis. The phase evens out and becomes acceptable for measurements after a certain point. 56
3.5 Reflected fields of rolled edge reflectors. 57
3.6 Rolled edge parameters taken from (a) [25] and (b) [51]. 58
3.7 Two-dimensional parabolic reflector with elliptic rolled edges (S2.1). 64
3.8 Illuminated region and shadow region of a scattering body. 65
3.9 Two-dimensional parabolic reflector with elliptic and blended rolled edges (S2.1) and (S2.2). 68
3.10 Coordinate system for 3D rolled edge design [25]. 70
3.11 Concave frame, target zone, and defining rectangle described as well as defining characteristics. 73
3.12 The first row depicts convex, rectangular, and concave rims (identical except for the r_e value). The second row shows the entire blended edge surface (again, identical parameters except for r_e). The third row includes the results from [46] displaying the magnitude of the diffracted fields from each reflector (10 GHz). 75
3.13 Three-dimensional parabolic reflector with elliptical edges (S3.1) 76
3.14 Three-dimensional parabolic reflector with blended rolled edges (S3.2). . . 78
3.15 Three-dimensional parabolic reflector with blended rolled edges front view. 78
3.16 Various ns values are illustrated for a common RMS roughness value. The distance between the black lines on the surface is 0.06 mm [58]. 80

3.17 Quiet zone phase variation for reflectors across surface roughness for various frequencies 100 through 500 GHz and with ns values of 250 μm, 500 μm, and 1000 μm. 82
3.18 Various 3D printed samples, treated and untreated, and their average roughness as measured by the profilometer. 84
3.19 Microscopic image from AFM of Form 3 resin printed surface (a) before and (b) after sanding by hand with a grit of up to 2000. 84
3.20 Microscopic height images (0.1 in x 0.15 in) from profilometer of PLA printed surfaces (a) untouched (b) sanded by hand with a grit of up to 2000 (c) sanded and coated with silver paint (d) sanded and copper plated and (e) sanded and covered with copper tape. 85
3.21 Distortion in the aperture plane induced by surface distortion. 87
3.22 Calculated and simulated loss in gain due to reflector roughness. 88
3.23 Fabrication process from initial 3D prints to silver coated reflector. 90
3.24 Second 3D printed reflector in the process of being coated with copper tape. 91

4.1 Similar mmWave metrology system that inspired the arrangement of the current system [64]. 95
4.2 Universal Robots 3 (UR3) positioning tool [68]. 99
4.3 ATM Ka-band standard gain horn antenna. 100
4.4 ATM standard gain horn (a) antenna pattern at 33 GHz and (b) gain and return loss over frequency. 100
4.5 MVG Standard Gain Horn Antenna. 101
4.6 Ka-band CATR system. 103

5.1 Visual of total scan size compared to expected quiet zone size overlayed on the reflector as a guide for the following figures. 105
5.2 Measured magnitude and phase grids with copper taped reflector. 106

5.3 Measured magnitude and phase grids of quiet zone (12 cm x 10 cm) with copper taped reflector. 107
5.4 Quiet zone phase cuts of copper reflector in (a) $x-$ and (b) $y-$ planes. . . . 108
5.5 Variation of phase over frequency for phase cuts viewed in Figure 5.4 for (a) $x-$ and (b) $y-$ planes. 108
5.6 Quiet zone magnitude cuts of copper reflector in (a) $x-$ and (b) $y-$ planes. 109
5.7 Variation of magnitude over frequency for magnitude cuts viewed in Figure 5.6 for (a) $x-$ and (b) $y-$ planes. 109
5.8 Measured magnitude and phase grids with silver painted reflector. 111
5.9 Measured magnitude and phase grids of quiet zone (12 cm x 10 cm) with silver painted reflector. 112
5.10 Quiet zone phase cuts of silver reflector in (a) $x-$ and (b) $y-$ planes. 113
5.11 Variation of phase over frequency for phase cuts viewed in Figure 5.10 for (a) $x-$ and (b) $y-$ planes. 113
5.12 Quiet zone magnitude cuts of silver reflector in (a) $x-$ and (b) $y-$ planes. . 114
5.13 Variation of magnitude over frequency for magnitude cuts viewed in Figure 5.10 for (a) $x-$ and (b) $y-$ planes. 114

Abstract

With finite supply and increasing demand, the RF frequency spectrum is highly saturated with signals. There is an urgent need to design and implement antennas that operate at higher frequencies for applications such as 5G and 6G. The push to the frontier of higher frequencies demands the ability to efficiently and accurately characterize mmWave antennas. Compact antenna test ranges (CATRs) offer the unique ability to minimize the often-large distance needed to measure antennas in the far field by mimicking the planar waves seen in the far field using a parabolic reflector. Previous studies have produced reflector designs for compact ranges intended to operate well below the mmWave spectrum, however, very few works have studied the design and implementation of reflectors for the mmWave spectrum. This work describes the development of a CATR consisting of an offset parabolic reflector and studies the mathematical theory behind the reflector, the design process with reflector simulations, the roughness and manufacturing of the reflector, and the implementation of the reflector with a probe, AUT, and system to measure mmWave antennas effectively. This work demonstrates the feasibility of using additive manufacturing processes to develop reflectors for CATRs as an accessible solution to easily and economically measure mmWave antennas.

Chapter 1

Introduction

There has been a significant trend across many applications to move to higher frequencies. The radio frequency (RF) spectrum, in which technologies such as 5G, Wi-Fi, GPS, and more operate, has limited supply but increasing demand. Frequencies below 6 GHz are saturated with government and private users to such an extent that it is commonly referred to as the "beachfront" spectrum [1], [2]. This physical limitation that society is fast approaching is prompting engineers and researchers to explore higher frequencies up to the mmWave spectrum (characterized by most as 26.5 GHz and above) [3], [4]. With ever-evolving technology, naturally comes the need to constantly improve the design, measurement, and implementation of the new technology. Hence, as RF technologies such as antennas and filters are being developed at higher frequencies, the ability to test them is demanded in parallel [5], [6]. Possessing a compact antenna test range (CATR) specifically designed for mmWave operation opens the door for increased development and production of mmWave antennas [7]. The convenience is unmatched and necessary to expedite the technological advancement to higher frequencies. This thesis also proposes the concept of 3D printing the CATR reflector as a low-cost and competitive performance alternative to machining a reflector.

1.1 Motivation

Compact antenna test range facilities are an attractive alternative to overcome challenges faced in traditional antenna far field measurements [7]. The main advantage of employing a CATR is the significant reduction in size, and it is often the most efficient metrology option for higher frequencies such as the mmWave spectrum, which is becoming a more alluring field of interest.

Many antenna performance measurements are completed in the far field region, in which the emitted signal has traveled far enough to appear as a planar rather than a spherical wave to the receiving device. The far field region is characterized as starting at a minimum distance of

$$\mathrm{FFD} = \frac{2\mathrm{D}^2}{\lambda} \tag{1.1}$$

where D is the largest antenna dimension and λ is the wavelength [8]. However, it is commonly recognized that to achieve waves that are increasingly acceptably planar and for more credible measurements a more accurate definition of the minimum far field distance is

$$\mathrm{FFD} = \frac{4\mathrm{D}^2}{\lambda}. \tag{1.2}$$

With the original definition outlined in Eq. (1.1), the theory highlighting how the waves appear as planar is portrayed in Figure 1.1. Figure 1.1 also illuminates that at a distance of $2\mathrm{D}^2/\lambda$ there is still a 22.5 degree offset from a perfectly planar wave. Doubling the minimum distance reduces this offset to 11.25 degrees. By employing a well designed reflector, the CATR system can achieve an even smaller offset in the quiet zone region where the antenna under test (AUT) is placed. The challenge that comes with measuring in the far field distance is that these distances are often extreme and inconvenient in size.

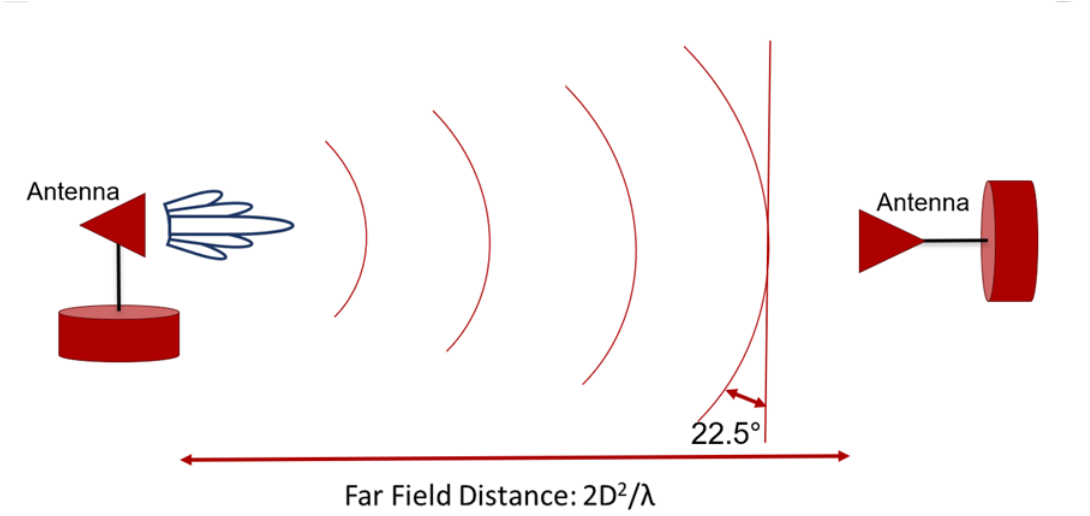

Figure 1.1: Visualization of an emitted signal appearing more planar over distance to allow for the far field distance to be measured

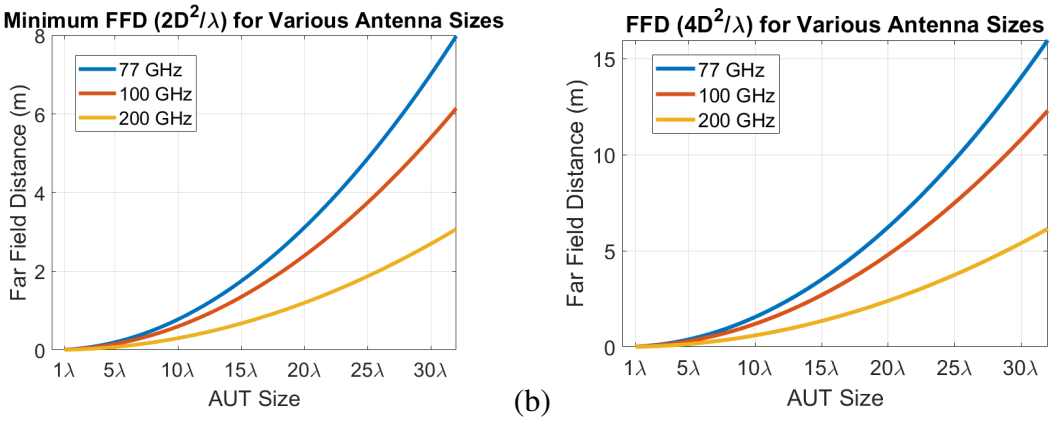

(a) (b)

Figure 1.2: Far field distance (FFD) over antenna under test size for 77 GHz, 100 GHz, and 200 GHz as calculated by (a) Eq. (1.1) and (b) Eq. (1.2).

One may argue that according to Eq. (1.1), the far field distance for mmWave antennas is not inconveniently large because the two main parameters, antenna size and wavelength, are smaller. However, the far field distance is determined by the ratio between the two, meaning the far field distance does not decrease over frequency at a steep enough rate to allow for convenience in measuring in the mmWave spectrum. Also, it is increasingly common for mmWave antenna systems to be designed as arrays. Phased arrays offer a

variety of desired flexibility and are being implemented in many applications, not the least of which is autonomous vehicles which are well known for operating in the mmWave bands [9], [10]. The far field distance for an array is much larger because the antenna dimensions are larger.

Figure 1.2 presents the far field distance of antenna arrays up to 32λ wide (roughly the size of a 64 element array) for frequencies of 77 GHz, 100 GHz, and 200 GHz. The figure includes distances for the minimum distance ($2\mathrm{D}^2/\lambda$) and also the more commonly accepted distance ($4\mathrm{D}^2/\lambda$). As shown, it is not unusual to expect the far field measurements to require more than 10 meters.

A CATR system overcomes many traditional obstacles, namely due to its compactness and ease to do on-the-fly measurements. What would originally require 10 or more meters can be completed in 1 meter. This is a substantial difference that would allow many engineering testing facilities to better accommodate demands with less real estate burden. As mentioned, CATRs also allow for precision in measurements and rival true planar waves in the quiet zone of the system, better than the 11.25 degree offset seen in traditional far field measurements.

CATRs are especially advantageous for mmWave applications in comparison to alternative antenna measurements to obtain far field results [7]. For example, one other strategy would be to measure the antenna system in the Fresnel region, or near field region, and, using Fast Fourier Transform (FFT) computations, calculate the far field measurement. This would allow for the far field measurements to be obtained without the traditionally large amount of space required since the antenna system would be measured at only the distance required for near field and not far field [8]. Although near field to far field conversions may work well for many applications, the mmWave spectrum introduces more difficulties. The extremely small wavelengths characteristic of high frequencies mean that the antennas themselves are smaller and there is a great need for exactness in the measurements. There

is a need for consistent precision as testing antenna performance requires numerous measurements across horizontal and vertical alignments. Being off by 1 cm at a 6 GHz antenna measurement would mean an offset of 10% of the wavelength, but the same small 1 cm offset for a 90 GHz system would mean an offset of 300% of the wavelength. In this case, a CATR would prove a better option as there would be no data processing and the system is more reasonably tolerant to small placement errors in the setup.

1.2 Literature Review

Marconi performed the first antenna pattern measurement in 1905 [11]. The idea for a compact range to take measurements more efficiently surfaced in the 1960s and was further developed into the 1970s with the work of Johnson of the Georgia Institute of Technology. The initial experiments completed by Johnson included using a 10-foot paraboloidal reflector to collimate the field of a horn antenna. Illuminating only the upper half of the reflector, the measurements with the rudimentary CATR system corresponded well with the measurements performed in a far field range [11]. Soon after, it was discovered that serrations helped tame the effects of edge diffractions when designed in a way that deflected the diffraction away from the AUT [12]. Many of the main developments concerning CATR reflectors deal with the progress in diluting edge diffractions by applying techniques such as blended edges and serrations.

The use of reflectors to direct and manipulate field propagation is not unique to CATRs and is even more prevalent in parabolic reflecting antennas. The earliest version of the parabolic reflector antenna was developed by German physicist Heinrich Hertz in 1888 [13]. The configuration type was that of a cylindrical-parabolic reflector. The use of these high-gain parabolic reflector antennas became more commonplace in the 1960s. Reflector, or dish, antennas have their origins in optical telescopes with scientists such as Cassegrain

and James Gregory designing refracting optical telescope instruments. These names may sound familiar because, today, reflector configurations based on the telescope designs such as the Cassegrain and Gregorian reflectors are well known and commonplace [13].

There are many variations of reflector geometries such as plane, corner, and curved. Parabolic, Gregorian, and Cassegrain fall under the curved category. Figure 1.3 displays each of these reflector configurations. The typical front-fed parabolic reflector has a feed at the focal point and the signal travels directly from the feed, to the reflector directly in front of it, and then back into space. The offset parabolic reflector behaves similarly, but with the notable difference that the feed is placed away from the center of the reflector and the dish is an asymmetrical segment of the parabola. This ensures that the the feed is still at the focal point but offset in a manner that it does not interfere or block the signal bouncing off the reflector into space.

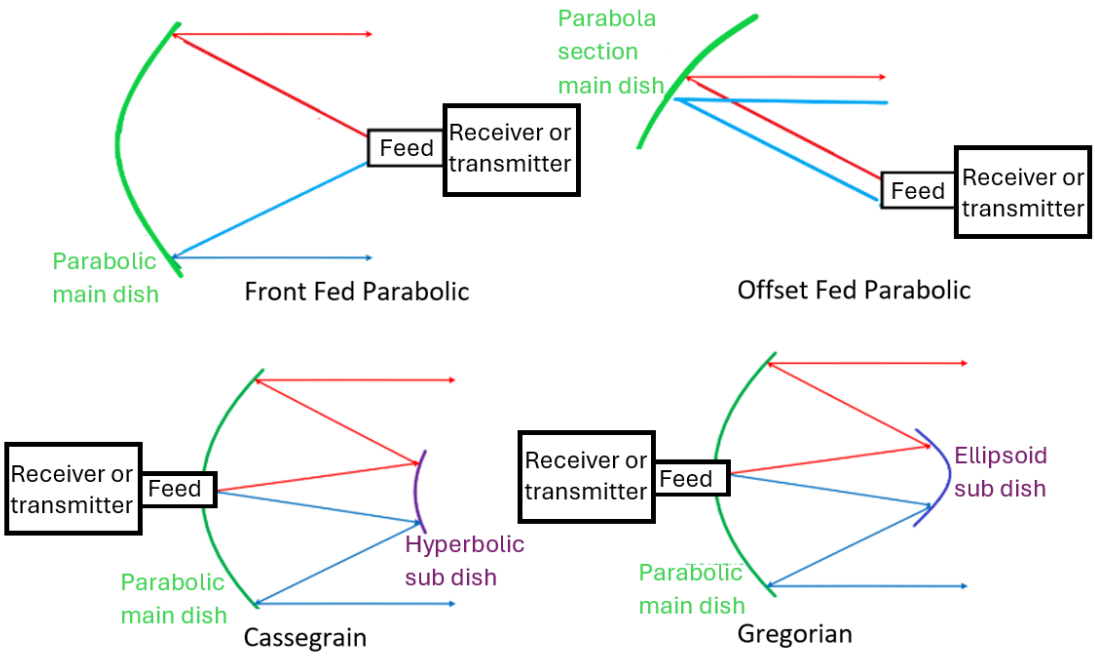

Figure 1.3: Various reflector configurations and their respective signal paths after being emitted from the feed [14].

The Cassegrain design consists of two reflectors, a parabolic main dish and a hyperbolic sub dish. The feed is placed behind the center of the parabolic reflector and the signal travels to the hyperbolic subdish. The sub-reflector shaping gives amplitude and phase control of the aperture illumination and spillover from the sub-reflector is directed out into space so the signal is not degraded [15]. The signal commences from the sub-reflector to the main reflector and then out into space. Again based on the telescope design, the Gregorian design is similar to Cassegrain, but the subreflector is a concave ellipsoid. The CATR system that this thesis proposes includes an offset parabolic reflector. As mentioned, this eliminates any blockage that would be seen in the front-fed parabola design. Design trade-offs to achieve maximal amplitude and phase taper efficiency, and balanced illumination for minimal spillover of offset parabolic reflectors are discussed in the next chapter.

There are also design variations among these reflector configurations to reduce edge diffractions. It is common to apply serrated edges or rolled edges to the rim of the reflector to target edge diffractions bouncing back into and contaminating the quiet zone. This is discussed in more detail in the following sections.

1.2.1 Alternatives to Reflectors in CATRs

Employing metallic reflectors is the most common method to create CATRs, but there are other strategies as well. Reflectarrays and plane wave generators (PWGs) are valid alternatives.

A reflectarray is a type of antenna that combines some of the advantages of phased arrays and parabolic reflectors with a planar design, high gain, ease of fabrication, and no requirement for feeding circuits [16]. Traditional reflectarray antennas use microstrip patch elements with various phase delay lines or different element sizes to control phase shifts. Each cell of the array is excited to reradiate outward of the aperture. By assigning

the reflection phase of each cell, a desired quasi-plane wave sourced from the reradiated component can be collimated [17]. Similar to the parabolic reflector approach, the reflectarray deals with edge diffraction issues. Several creative solutions have been invented such as orienting the reflectarray at a 45 degree angle or by purposefully manipulating the phase to steer the quiet zone away from the diffraction points [17]. Reflectarrays are convenient to fabricate compared to parabolic reflectors because they can be printed flat and inexpensively on a PCB, compared to the manufacturing of a parabolic reflector made out of aluminum [18]. The main issue with reflectarrays is their bandwidth as it is dependent on the bandwidth of the elements [18]. Issues arise in high-frequency limitations with the use of certain PCB materials. According to Borries [19], it is an involved process to create a necessary synthesizing algorithm and to calculate the uncertainty quantification.

PWGs are another interesting alternative to parabolic reflectors. A PWG, comprised of an antenna array with element placement and complex excitation, approximates a plane wave condition at a close distance [20]. The PWG relies on phased array technology, enabling it to concentrate the radiated energy within a quiet zone volume. This allows the PWG to be more compact compared to a CATR as it does not require a feed antenna and achieves the plane wave condition at a shorter distance. Edge diffractions do not pose a challenge to this solution type. According to Scirosi [20] the PWG performs better than the reflector-based CATR at lower frequencies and is capable of measuring lower frequencies with a smaller-sized system. However, when the frequency surpasses 10x the lower frequency limit, the CATR with parabolic reflectors performs better than the PWG. Thus, the reflector-based CATR has superior performance over a significantly wider bandwidth. Outside of bandwidth, the main issue with PWGs compared to reflectors is the need for powered elements and a more involved back-end system. Table 1.1 compares reflectarray and PWG performance to reflector-based CATR solutions. The following section outlines the reflector-based CATRs with different edge diffraction techniques.

Table 1.1: Comparing options of different compact antenna test range types

	Solution Type	Advantages	Disadvantages
Reflector Based Solutions	Reflector (no edge amends) 	• Wide bandwidth (limited by RMS) • Simple manufacturing compared to serrated and blended edges	• Limited quiet zone performance • Considerable edge diffractions
	Serrated Edge 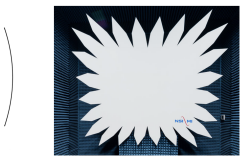	• Wide bandwidth (limited by RMS) • Simple manufacturing compared to blended edges	• More expensive than untreated reflector • Limited performance compared to blended edges
	Blended Edge 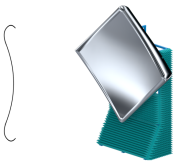	• Wide bandwidth (limited by RMS) • Best performance of reflectors	• Complex to manufacture • More expensive
Other Solutions	Reflectarray 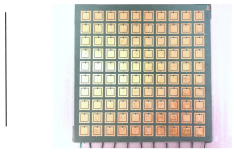	• Promising research for mmWave applications • Easy manufacturing, fabricated on PCBs • Least expensive	• Narrowest bandwidth (limited by elements) • Requires much calibration
	Plane Wave Generator 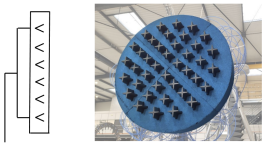	• Best performance for low-frequency • No edge diffractions • Small form factor	• Narrow bandwidth (limited by elements) • Powered elements • Limited performance above UHF/VHF compared to parabolic reflectors

1.2.2 Minimizing Edge Diffractions

Multiple ideas have been introduced throughout recent history to minimize the edge diffractions that occur when the signal bounces off the edge of the reflector. Oftentimes the presence of untreated edge diffractions will disturb the quiet zone and disrupt the planar waves. To combat this issue, the two main techniques are employing serrations and rolled edges. Overall the blended roll, when designed correctly, typically results in a superior quiet zone than serrated edges, but the added manufacturing complexity results in a much higher cost. Figure 1.4 displays design examples to highlight these two solutions.

Edge treatment has received much attention over the years since the development of the first commercial compact range. Burnside [21] recommended that an elliptical rolled edge be used, but quickly found that the abrupt change in curvature caused diffraction effects. Burnside [22] overcame this effect by introducing the blended rolled. Figure 1.5 demonstrates the impact of blended edges in deflecting unwanted edge diffractions to ensure no undesired diffractions reflect to the quiet zone. The blended rolled edge produces a better field in the quiet zone that has a smaller ripple than serrations, but it greatly complicates manufacture, hence it is more costly.

Lee and Burnside [23] compare a 20λ x 20λ optimally designed blended edge reflector and an identically sized serrated reflector. The central parabolic component for each is 10λ x 10λ, and the edge treatment extensions are added allowing the total reflector size to be 20λ x 20λ. The blended edge performed significantly better than serrations of all sizes up to the 20λ total size limit. The stray signal levels for the blended rolled edge reflector were on average more than 15 dB lower than those for the serrated design [23], [24]. The downside to the blended edge design is the increased expense incurred in the manufacturing process, to this extent serrated designs are more commonly employed in industry, but this work attempts to overcome this disadvantage by 3D printing the rolled edge reflector.

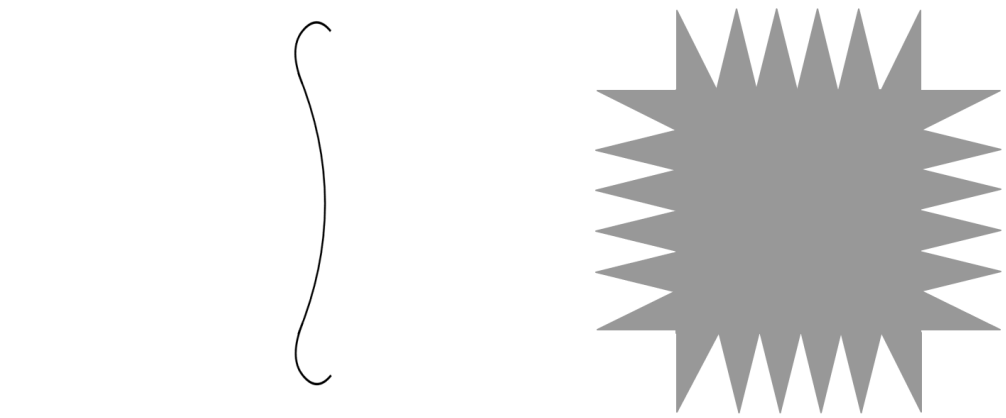

(a) (b)

Figure 1.4: Common design methods to reduce edge diffractions are shown. (a) Side view of a blended edge reflector and (b) front view of a serrated reflector.

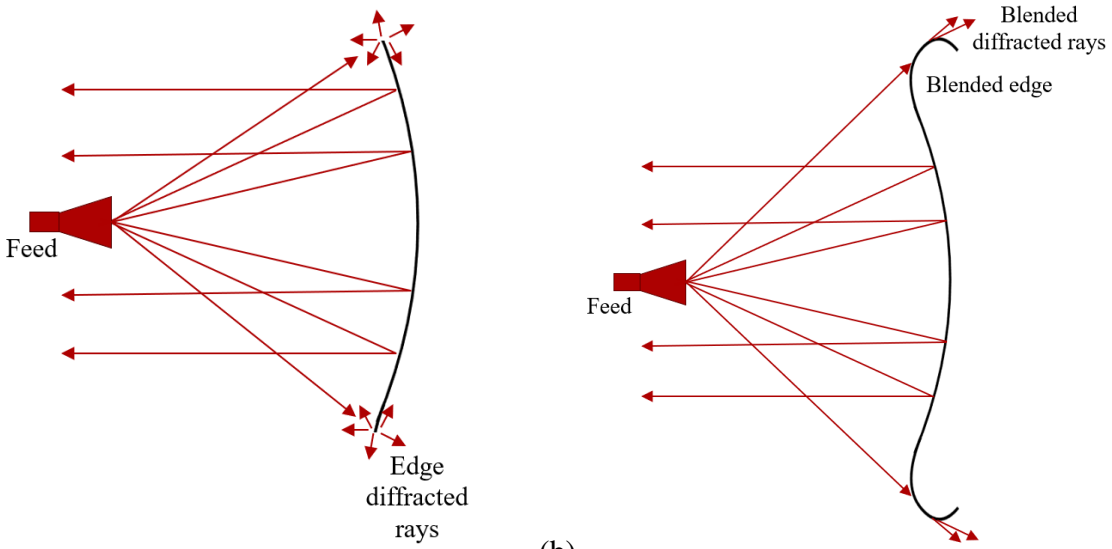

(a) (b)

Figure 1.5: Field comparison of a feed antenna illuminating (a) a traditional parabolic reflector and (b) a blended edge parabolic reflector to visualize the difference in edge diffractions.

Gupta [25], [26], [27] has been a pioneer in improving reflector design and proposed processes to design blended edges. Gupta [28] has also contributed to improving reflector design by presenting a Physical Optics (PO) analysis of serrated edge reflectors to mathematically compare rectangular rim reflectors with and without serrations. In turn, Schluper [29] developed a verification method for the serration design. This verification method consisted of RCS measurements of reflector strips each terminated in different shapes. Many researchers have studied various serration shapes to determine the optimal construction. The RCS vs. angle data could be converted to induced current distributions and then the fields in front of these reflector strips can be calculated using Physical Optics. Using this technique, Schluper discovered that cosine-shaped serrations performed better than triangular ones. Joy [30] at Georgia Tech introduced the petal-shaped serrations which have been incorporated in all of the March Microwave reflectors [21], [22]. Joy [30] presents the specific equation defining the serration shape and shows that the addition of serrations of lengths larger than ten wavelengths of a flower petal shape reduces the stray radiation in the quiet zone by as much as 10 dB. Yet another serration variation is shown in an NSI-MI reflector in Figure 1.6 which employs a piece-wise approximation to flower petal serrations, embodying more trapezoidal pieces with a triangular top. The petal shapes also offer the advantage of reducing the physical length of the serrations, which eases the manufacturing cost and process.

In terms of reflectors for mmWave applications, few resources outline successful techniques specific to this spectrum. The ideal number of serrations may depend on the operational frequency and there is a minimum number of serrations needed to provide a good performance [23]. Several studies [29], [32], [33] confirm that the cosine shape outperforms the triangular shape in most cases, and [34] confirms this is true specifically for the mmWave spectrum. Multiple serration shapes were studied in great detail for this project.

Ultimately, the proposed system of this research implements a blended edge solution

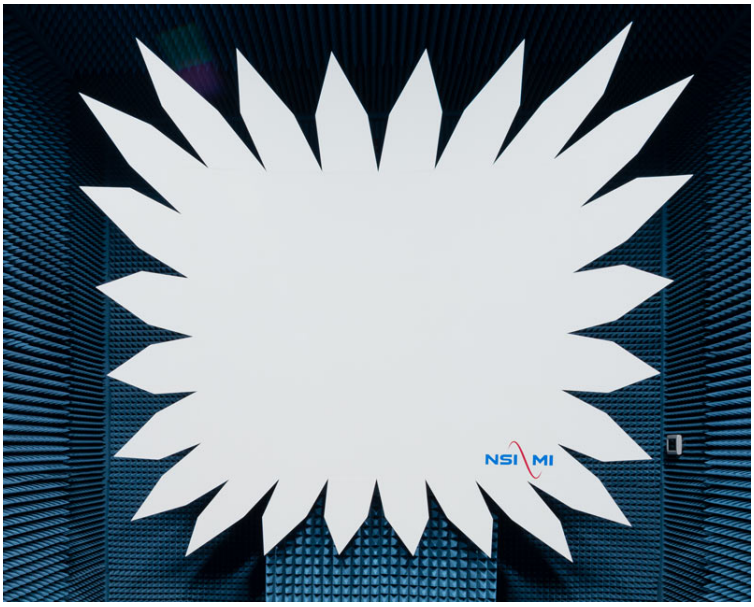

Figure 1.6: Example CATR reflector created by NSI-MI Technologies, an antenna metrology company [31]. Piece-wise petal-shaped serrations are used.

due to its superior performance. The cost of manufacturing is overcome by the novel idea of 3D printing the reflector, rather than the usual method of manufacturing by milling metal. Chartering an additive manufacturing approach is a unique solution that allows for ease of fabrication and decreases costs substantially. However, this technique has its challenges as well. Working in the mmWave spectrum requires extremely smooth surface roughness of the reflector. The limitation of the size of the 3D printer is an added consideration. Since the reflector is made from 3D printing filament, it needs to undergo treatment to be coated with a metallic lining to make it reflective. Silver paint and copper tape are the two main explored solutions. Even if the 3D print itself meets the surface roughness requirements, the final coated reflector must also be smooth. These challenges are reviewed in Chapter 3.

1.3 Proposed System

The objective of this thesis is to investigate the requirements to develop a CATR for high-frequency antennas and, based on that knowledge, to implement a mmWave compact range. The current literature is limited in the use of compact ranges at this frequency spectrum. Parameters such as the reflector design is explored and instruments are selectively chosen for this project. This thesis presents a comprehensive study on the design and implementation of a compact antenna test range throughout it's six chapters.

The reflector as the central component of the CATR system is the main focus. The design process of an offset parabolic reflector is explored and simulated in ANSYS HFSS and TICRA GRASP. Options investigated are optimal depth of the reflector, the ideal probe to illuminate the reflector, and maximizing efficiency while minimizing spillover effects. The mathematical theory behind adding rolled edges to the parabolic reflector is described extensively in Chapter 3. Based on the computations and simulations, a Ka-band reflector design is proposed. Additive manufacturing options are explored and implemented. Considerable surface roughness analysis is completed. The final reflector design satisfies surface roughness requirements and applies considerations that accompany designs employing blended rolled edges. With the completion of these studies, the reflector is fabricated and integrated into a system to obtain measurements.

The other system components include the illuminating probe, vector network analyzer (VNA), frequency extenders (FE), antenna under test (AUT), and positioners. The setup is capable of measuring parameters such as the S-parameters, power, and phase of the antenna measurements. The signal of the probe is emitted towards the offset parabolic reflector, which then reflects the signal to the AUT located in the quiet zone. After the hardware and software pieces of the system are integrated, the CATR is ready to measure antennas ranging from 26.5 - 110 GHz with full flexibility on many parameters.

1.4 Thesis Outline

Chapter 2 provides additional background information on fundamentals such as the IEEE Standards for antenna measurements and why compact ranges are a practical solution. This fundamentals chapter also dives into the mathematical theory of how reflectors manipulate the projected fields to collimate them into a planar wavefront. A simple example of the design of a reflector is presented along with simulation results from ANSYS HFSS. This chapter also analyzes design trade-offs that must be considered for compact ranges and TICRA GRASP simulations shown to support claims [19].

Chapter 3 of this thesis focuses on the main aspect of the proposed compact test range system: the reflector. The design process and various trade-offs are discussed. Aspects such as the curvature design, surface roughness, and fabrication process are outlined.

Chapter 4 describes the system implementation. A project overview and an explanation for each component within the compact range system is included. The individual instruments such as the VNA and antenna probe are discussed in detail. How the components of the system are created and integrated is demonstrated. The hardware and software are discussed. This chapter recounts the assembly process that ultimately allows the system to be usable.

Chapter 5 outlines the success of the system by presenting the resulting measurements. Chapter 6 concludes this thesis with a discussion and summary of the findings on the mmWave compact test range.

Chapter 2

Fundamentals

This chapter will discuss the requirements to perform successful antenna measurements focusing mainly on the criteria for far field measurements - mathematically explaining why certain criteria are in place and how to incorporate it into a far field measurement range. Phase, amplitude, and other quiet zone metrics will be discussed. This chapter will then specifically discuss the suggestions for compact ranges in particular and analyze certain trade-offs that must be considered in compact range design such as amplitude and illumination trade-offs.

2.1 IEEE Measurement Requirements

IEEE [35] has published guiding protocols for antenna measurements to ensure conformity and the highest quality measurements among researchers and engineers. According to these highly adhered to standards, there are three general types of ranges to measure an AUT in the far field distance of a wavefront with an approximated uniform plane wave:

- Free-space ranges. This type of range suppresses the effects of the surroundings to acceptable levels, such as anechoic chambers [35].

-Ground reflection ranges. This type of range is designed to use reflections to produce an approximated plane wave [35].

-Near-field ranges. This type of range is designed to produce a uniform plane wave through mathematical transforms such as spatial Fourier analysis [8].

Compact ranges are included in the free-space range classification. These measurements are guided by the interest in obtaining the radiation patterns of antennas. Knowledge of an antenna's radiation pattern is desired because it conveys an antenna's behavior and characteristics such as the beamwidth, side lobe levels, and the cross-polarization level. The measurements are usually focused on three main cut planes: the E-plane, where the electric field lies, the H-plane, orthogonal to the E-plane, and the D-plane, or the diagonal plane, between the E- and H-planes. The standard practice for measuring radiation patterns in antenna ranges is illuminating the AUT with the probe and rotating it in azimuth or elevations for different cut planes with the use of positioners. The radiation patterns can be obtained with far field or near field measurements. Near field measurements are completed when the probe and the AUT are only a few wavelengths apart, meaning the radiated power is mostly reactive. Far field measurements are collected when the probe and the AUT are separated by a much greater distance, which was discussed in Chapter 1, and will be elaborated on shortly. The greater distance must be large enough to meet certain criteria. The fundamental criteria for a basic far-field range include considerations of the following parameters:

- The coupling between the probe and AUT
- The amplitude taper of the illuminating wavefront
- The phase curvature of the illuminating wavefront
- Variations in the wavefront caused by reflections
- Interference from spurious sources

In this chapter, these considerations will be expounded and will be discussed to ensure the compact range will meet the requirements concerning these considerations outlined by [35].

2.1.1 Phase

According to the IEEE standards recommended practice for antenna measurements [35], there is an established relationship to determine the phase variation of the field illuminating the AUT. For a spherical wavefront, assuming minimal reflections, the phase deviation, $\Delta\phi$, is given as

$$\Delta\phi = \frac{\pi D^2}{4\lambda R} \tag{2.1}$$

for $D/R << 1$ where D is the maximum diameter of the AUT and R is the range between the probe and the AUT.

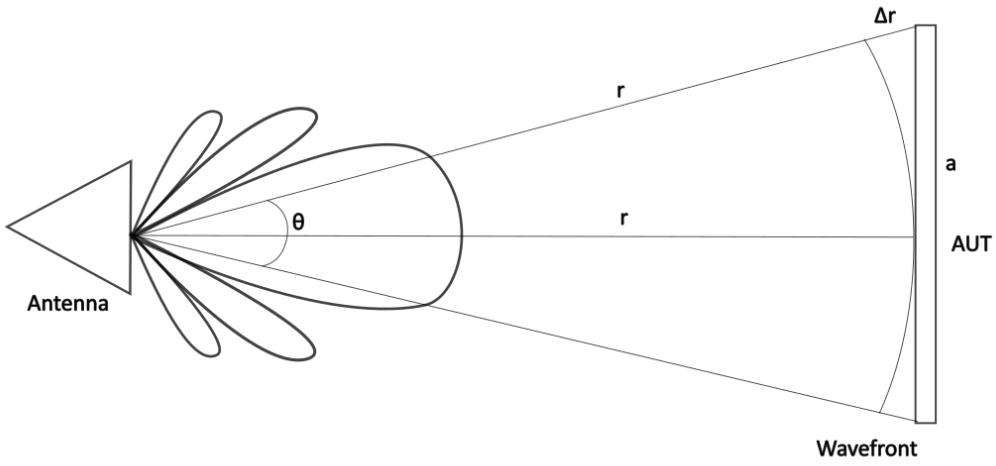

Figure 2.1: Illustration of a probe's antenna pattern projection onto the AUT's aperture.

The most commonly accepted criterion is to restrict $\Delta\phi$ to 22.5 degrees, resulting in the well-known far field equation

$$R \geq 2D^2/\lambda. \tag{2.2}$$

This relationship is derived as follows. In Figure 2.1 the distance between the probe and the center of the aperture is r. However, this distance varies from the probe to different points on the aperture. For example, the maximum distance is to the edge of the aperture

where the distance is $r + \Delta r$. The Pythagorean theorem can be applied to the right triangle as $r^2 + \frac{a^2}{4} = (r + \Delta r)^2$. It can be concluded that $\Delta r = \frac{a^2}{8r}$. This difference in the path length is what creates a phase difference across the aperture. As mentioned, it is widely accepted that this should not exceed $\pi/8$, or $\lambda/16$, to minimize measurement errors without requiring largely impractical distances. If $\Delta r \leq \lambda/16$, then

$$r \geq \frac{2a^2}{\lambda}. \tag{2.3}$$

If greater precision is required, for example when measuring very low sidelobe levels, the minimum range needed for an arbitrary phase error is expressed by

$$r \geq \frac{\pi a^2}{4\lambda\Delta\phi}. \tag{2.4}$$

In further analysis to illustrate the far field distance with respect to frequency, recall Figure 1.2. The far field distance for AUTs of 77 GHz, 100 GHz, and 200 GHz are displayed for phase requirements of 22.5 degrees and 11.25 degrees. The far field distance decreases with respect to frequency but severely increases with respect to stricter phase requirements. It is also shown that the larger the AUT size, the larger the far field distance required as well, so AUTs that are antenna arrays will require more space than a single element. It can also be shown that an AUT of smaller beamwidth also requires larger far field distances.

In summary, to consider the phase curvature of the illuminating wavefront as the IEEE standards recommend, AUTs must be placed in an area with minimal phase change over the aperture and this is usually achieved by placing the AUT in the far field distance. However, a well-designed compact range solution will achieve smaller phase changes over the aperture with the use of a reflector.

2.1.2 Amplitude

The IEEE standards [35] also require considering the amplitude taper of the illuminating wavefront, in both the transverse and longitudinal planes. Similar to the phase requirements, it is also ideal that the illuminating wavefront also has uniform amplitude to ensure the field distribution, and, by extension, the antenna pattern, is not modified. Let's call the subtended angle across the probe that projects to the AUT aperture the projected beamwidth. It is depicted in Figure 2.1 as the angle θ. This projected angle determines what section of the probe's radiation pattern will illuminate the AUT aperture, and, by extension, the amplitude taper across the aperture. The projected beamwidth can be denoted as

$$\theta_{pr} = 2 \arctan \frac{a}{2r} \tag{2.5}$$

and, inserting the expression for r as seen in Eq. (2.3), the resulting expression is

$$\theta_{pr} = 2 \arctan \frac{\lambda}{4a}. \tag{2.6}$$

Thus, the projected beamwidth gets smaller for a smaller aperture. The projected beamwidth will also decrease as an AUTs aperture beamwidth decreases. The antenna's directivity and projected beamwidth are trade-offs that need to be considered. The antennas with broader beamwidth may result in increased errors due to reflections from the antenna range, however, a probe that is too directive will not effectively illuminate the aperture uniformly. According to the IEEE standards [35], in many test ranges, to minimize the negative effect of the transverse amplitude taper it is recommended to choose a range antenna that yields a 0.25 dB taper across the AUT aperture. Depending on the situation a broader or narrower beamwidth may be selected. For situations where it is necessary to use an antenna with a narrower beam, the alignment of the antenna and AUT becomes more

crucial. For reference, if the amplitude taper is -0.5 dB at the edge of the AUT aperture, there is a directivity reduction of ~ 0.15 dB as compared to without a taper [35].

In the context of compact ranges, the feed antenna beamwidth and directivity is still a deciding factor for uniform amplitude illumination but it is analyzed in reference to the illumination of the reflector. It is undesired to have a feed that has too broad of a beamwidth such that the excess signal over illuminates the reflector and causes spillover.

2.1.3 Quiet Zone Metrics

An antenna test range requires that the range present a planar wave front that is aligned to the measurement coordinate system [18], [36], [37]. According to the IEEE standards for antenna measurements [35], the quality of this quiet zone (QZ) is defined by the amplitude taper, amplitude ripple, phase variation, and quiet zone reflectivity.

- Amplitude taper is measured as the variation of a second-degree polynomial fit through the amplitude data over the quiet zone. As mentioned in Section 2.1.2, it is often ideal to opt for a design that yields a 0.25 dB amplitude taper across the AUT aperture but this is not always the case, especially for CATRs where the requirement is $<$ 1 dB [35]. Much of this work adheres to the IEEE standards for antenna measurement, but the standards for systems built for radar cross section (RCS) measurements are similar. The typical amplitude taper standard for RCS measurements is less than 1 dB of variation [38]–[40]. Many CATR products on the market advertise their best capability as at or around 1 dB of amplitude taper [41].

- Amplitude ripple is measured by determining the variation of amplitude about the second-degree polynomial fit. The requirement is $\pm$ 0.5 dB [35].

- Phase variation is derived from a field probe trace by measuring entirety of the phase over the aperture of the QZ. There are other parameters, such as phase ripple and phase

taper, that can be reported to show the purity of the plane wave across the QZ, but these are less commonly used. As mentioned in Section 2.1.1, it is recommended to limit the phase variation to 11.25 degrees. This cut-off becomes even lower ($\sim$ 10 degrees) when the test range is used for RCS measurements rather than antenna measurements [38].

- Quiet zone reflectivity is the difference in dB between the direct path between the range antenna and the QZ and the highest level of reflected energy entering the QZ.

Figure 2.2 provides a visual of the described metrics. These parameters describe the quality of the plane wave and are alluded to in the rest of this work. This is the basis for a CATR to ensure a quality system is constructed. In line with the requirements, the goal for the proposed system is $<$ 11.25 degree phase variation and $<$ 1 dB amplitude taper.

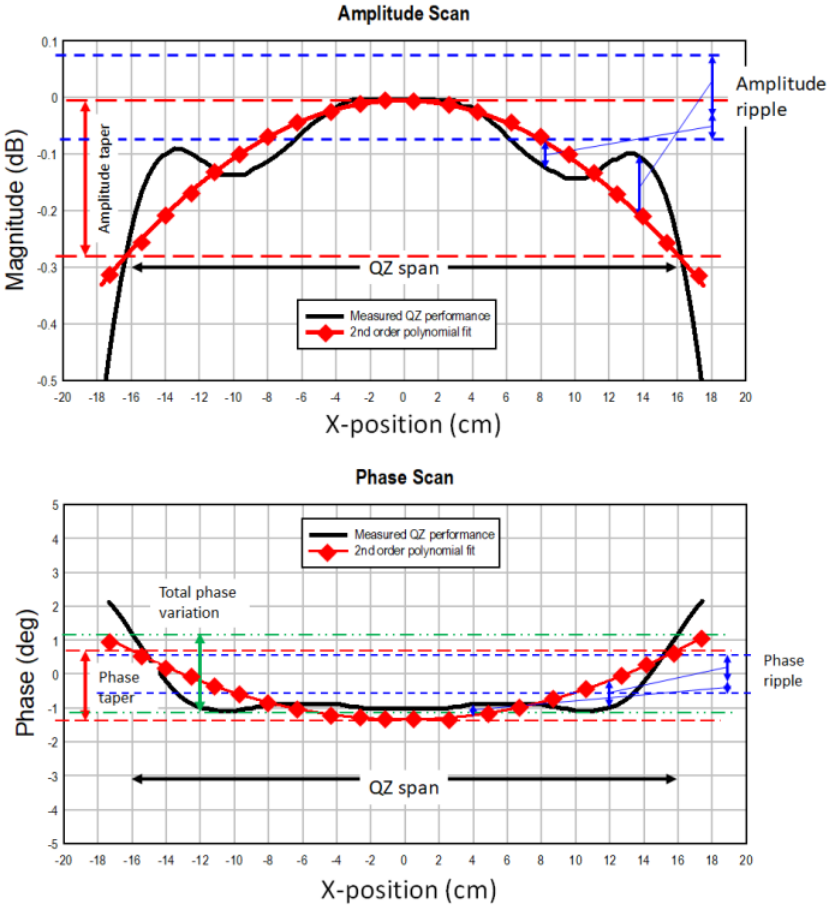

Figure 2.2: Quiet zone metrics of amplitude and phase as presented in [35].

The following section begins to explain the compact antenna test range: how it is a feasible solution to obtain the highlighted requirements, how it is an improved solution to traditional test ranges, and trade-offs that must be considered.

2.2 Compact Range Solution

Now that the previous section outlined measurement requirements as guiding parameters for this project, it is time to explain at a fundamental level, how this project works and can meet these requirements. This section covers the fundamentals of a compact antenna range and how utilizing a reflector for antenna measurements works at a physical and mathematical level. After the basic foundation is set describing the mathematical theory that substantiates the compact antenna test range system, various trade-offs can be explored. Certain aspects of the design can be altered to obtain different results and multiple case studies are simulated to analyze these examples. First, the amplitude taper versus illumination trade-off will be discussed to explain the compromise between balancing optimal efficiency while reducing spillover. Second, the focal length to diameter (f/D) ratio is discussed with a case study of reflectors with different f/D ratios compared. Next, a study is done to determine the optimal characteristics of the antenna to illuminate the reflector. Lastly, a series of simulations are compared with various probe tapers to observe the effect on the (ideally) planar wave entering the quiet zone.

2.2.1 Reflector Mathematical Theory

The purpose of the reflector is to collimate spherical waves into planar waves. As shown in Figure 2.3, this phenomenon is achieved by utilizing the mathematical characteristics of a parabola. Every parabola has a focal point and an aperture plane. Many line segments can be drawn from the focal point to a point on the parabola, and then directly to the aperture

plane. Figure 2.3 depicts several of these line segments. Three of the line segments are labeled as follows: $\overline{\text{ABC}}$, $\overline{\text{ADE}}$, and $\overline{\text{AFG}}$. Each of these line segments starting from the focal point and ending at the aperture plane are the same total length. In terms of length, $\overline{\text{ABC}} = \overline{\text{ADE}} = \overline{\text{AFG}}$. Because the distance traveled from the focal point to the aperture plane for each angle of the radiating signal is the same, a planar wave is formed at the aperture plane. If the reflector could be infinitely huge, then the wave would be perfectly planar, but as this is unrealistic, the quiet zone is characterized as quasi-planar waves that are acceptable for our purposes.

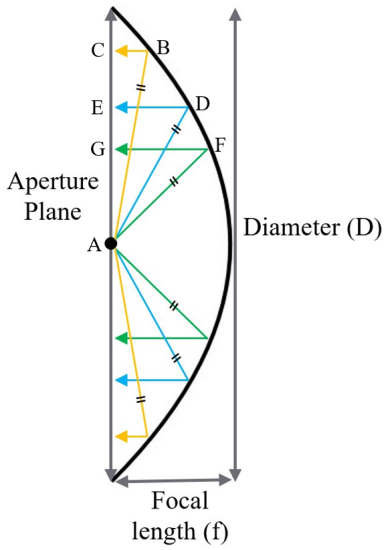

Figure 2.3: Example of a parabolic reflector. The reflector successfully turns the waves emitted from the feed at the focus into plane waves because the distance from the focus to the reflector and back to the aperture plane is equivalent regardless of which section of the parabola is contacted. The line segments $\overline{\text{ABC}}$, $\overline{\text{ADE}}$, and $\overline{\text{AFG}}$ (yellow, blue, and green) are all the same length, meaning a plane wave is present at the aperture plane.

A defining characteristic of a given reflector is its focal length to diameter (f/D) ratio. This relationship determines how shallow or how deep is the parabolic reflector. A larger f/D ratio results in a shallower reflector dish. The reflector's f/D ratio also determines how close is the aperture plane. For reflectors with an f/D ratio of 0.25, the focus lies in the

aperture plane. The focus lies inside the aperture plane for f/D < 0.25, and the focus lies outside the aperture plane for f/D > 0.25. An example of each scenario is shown in Figure 2.4 to display the focal point position compared to the aperture plane.

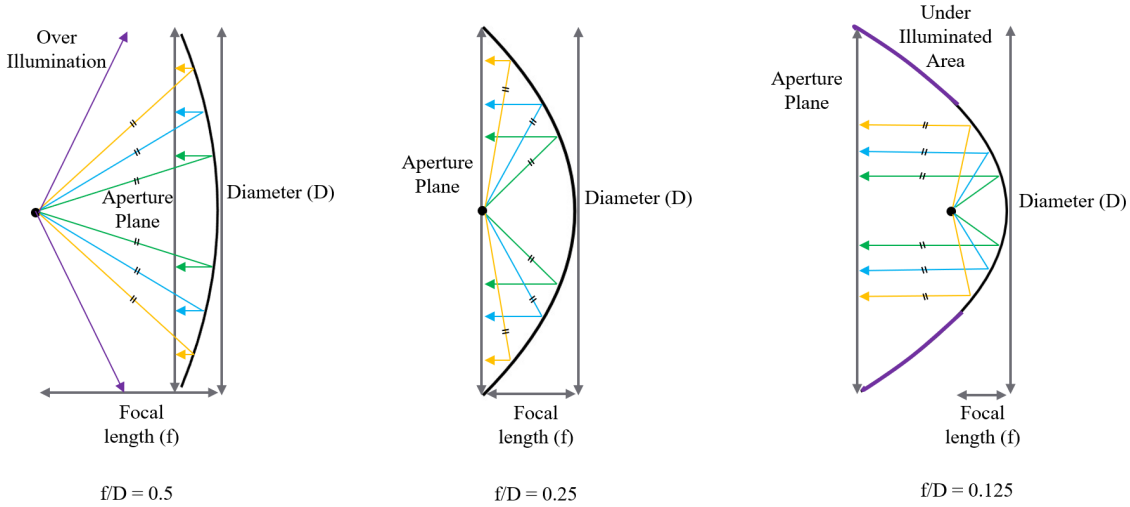

Figure 2.4: Example of parabolic reflectors with various f/D ratios. The reflector successfully turns the waves emitted from the feed at the focus into plane waves because the distance from the focus to the reflector and back the aperture plane is equivalent regardless of which section of the parabola is contacted. The yellow, green, and blue arrows seen in each reflector example are all the same lengths, meaning a plane wave is present at the aperture plane.

Different effects occur for reflectors of different f/D ratios. When the focal point is outside the aperture plane (f/D > 0.25), the feed over-illuminates the reflector and spills over the reflector rim. This spillover is an inefficient use of energy and can result in harmful edge diffractions as too much radiation striking the rim can cause rays to bounce back and tamper with the quiet zone. Let's compare this to a case where the focal point lies within the aperture plane (f/D < 0.25). Figure 2.4 shows that instead of over-illumination occurring, the reflector is under-illuminated. This is an inefficient use of the reflector, leaving large swathes of it unused and resulting in a smaller quiet zone. The following section explores more of these trade-offs.

Figure 2.3 and Figure 2.4 display parabolic reflectors, but notice that placing a feed in

the focal point would block the waves bouncing from the reflector to the quiet zone. To ensure that the feed does not impede the quiet zone, an offset-fed parabolic reflector is employed rather than a front-fed. For an offset-fed reflector, only a piece of the original parabola is used. The reflector is formed out of a piece of a larger paraboloid, specifically a piece above the plane including the focal line. Thus, the feed can remain in the focal point, which is critical to the system's success, without impeding the signal.

The rest of Chapter 2 delineates several trade-offs and how different decisions can impact the compact antenna test range system. The following section highlights the amplitude taper and illumination trade-off. The reflector should be adequately illuminated by the feed, but over-illumination to a certain extent is inefficient and can cause unwanted edge diffractions, while under-illuminating is also inefficient to a point as the quiet zone will suffer from extreme amplitude taper. Recall that amplitude and phase variation should be kept to a minimum for an optimal quiet zone.

2.2.2 Amplitude Taper and Illumination Trade-off

The f/D ratio of the reflector as well as the beamwidth and power of the feed antenna determine the illumination [42]. Narrow beamwidths ensure minimal power spills over the edge of the reflector (spillover) but also cause the reflector to be under-illuminated, which limits efficiency. A wider beamwidth ensures better reflector illumination, but at the cost of increasing spillover and introducing harmful edge diffractions. Increased reflector illumination translates to a larger quiet zone. Section 2.2.5 (specifically Figure 2.20) elaborates on this further. This is a trade-off that must be optimized for best efficiency. Figure 2.5 illustrates illumination and spillover losses from a radiation pattern pointed at a reflector.

This report approximates the spillover and amplitude taper trade-offs by assuming a general feed pattern of $cos^{2N}(\psi/2)$ [42]. The variable N is defined by the beamwidth of

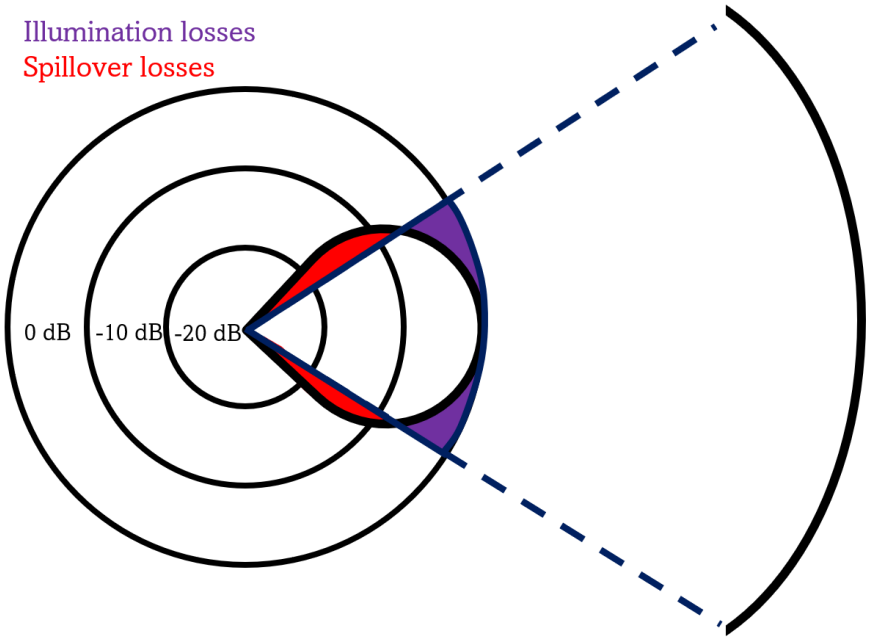

Figure 2.5: Example of a feed antenna pointed at a reflector and the resulting losses from under illumination and spillover effects.

the feed and the dB level related to that beamwidth (Level) as defined by Milligan [42].

$$N = \frac{\text{Level(dB)}}{20 \log \left(\cos \left(\text{beamwidth}_{\text{Level(dB)}}\right)/4\right)} \tag{2.7}$$

With this approximation, the spillover efficiency and amplitude taper efficiency are found as

$$\text{spillover efficiency} = 1 - u^{2(N+1)} \tag{2.8}$$

and

$$\text{amplitude taper efficiency} = \frac{4(N+1)(1-u^N)^2}{N^2(1-u^{2(N+1)})} \cot^2 \frac{\psi_0}{2} \tag{2.9}$$

where $u = \cos(\psi_0/2)$ and ψ_0 is the half subtended angle of the reflector. Figure 2.6 displays the spillover and amplitude taper efficiency for reflectors of various f/D ratios when paired with a feed of 10 dB edge taper.

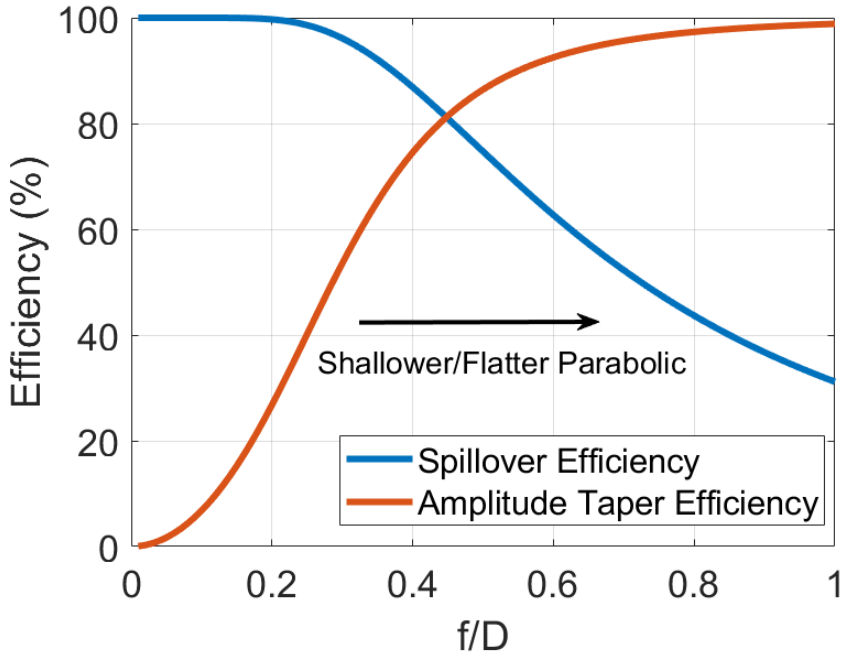

Figure 2.6: Spillover efficiency and amplitude taper efficiency for reflectors of various f/D ratios assuming a feed with 10 dB edge taper.

As the parabolic reflector becomes shallower, the spillover increases but the feed antenna illuminates more of the reflector which greatly improves efficiency after a certain point. On the contrary, a much deeper dish (small f/D) means that much more of the signal is contained and spillover is eliminated. The drawback is that the plane wave with an acceptable amplitude taper is too small to be of good use in most cases. A middle ground must be met where spillover is mitigated, but an efficient amount of the reflector is still being used to allow for acceptable amplitude taper. In this case, with an antenna feed pattern of $\cos^{2N}(\psi/2)$, if a reflector has an f/D equaling 0.4, then the spillover efficiency would be 85% and the amplitude taper efficiency 77%. This would equate to spillover losses of -0.61 dB and amplitude losses of -1.2 dB.

The following section continues a similar discussion concerning the effects the f/D ratio has on the system. A reflector with an f/D ratio of 2.3 is compared to a reflector with an

f/D ratio of 0.6 and the resulting quiet zones are explored. The simulation results will also illuminate the impact of edge diffractions caused by spillover.

2.2.3 f/D Ratio Trade-off

Simulations were performed to compare reflector designs with identical diameters, but varied focal lengths. Modifying the focal length while maintaining the reflector diameter will vary the f/D ratio. The variation in f/D ratio is studied to analyze whether a greater f/D ratio (larger focal length and shallower reflector dish) or a smaller f/D ratio (smaller focal length and deeper reflector dish) results in less phase variation in the quiet zone.

For this experiment, two reflectors, Reflector A and Reflector B, are compared. Reflector A is based on a compact antenna reflector designed by NSI-MI Technologies. Reflector A, based on the NSI-MI reflector model CRR-CRC-1, has a focal length of 2.3 m, a diameter of 1 m, and operates starting at 20 GHz. The corresponding f/D ratio is 2.3. Reflector B has a focal length of 0.6 m and has a much deeper reflector. Reflector B has an f/D ratio of 0.6. Since these designs are both offset reflectors such that the feed does not block the system, the offset of Reflector A from the xy plane it is levitating over is 0.2 m and Reflector B is offset by 0.12 m. The feed angle at which the antenna is tilted from the xy-plane is 17 degrees and 54 degrees for Reflectors A and B, respectively. Figure 2.8 displays the illustration of these designs, but first, Figure 2.7 observes the phase cuts at various distances.

Figure 2.7 compares the phase cuts of Reflector A and Reflector B. The simulation extracted the phase from -1 meter to +1 meter extending vertically across the reflector at different distances away from the reflector. However, this data was trimmed to include the phase in the quiet zone which occurs from -0.45 meters to 0.45 meters across, roughly the same size as the reflector itself. The phase was captured at every half meter (every 33.3λ).

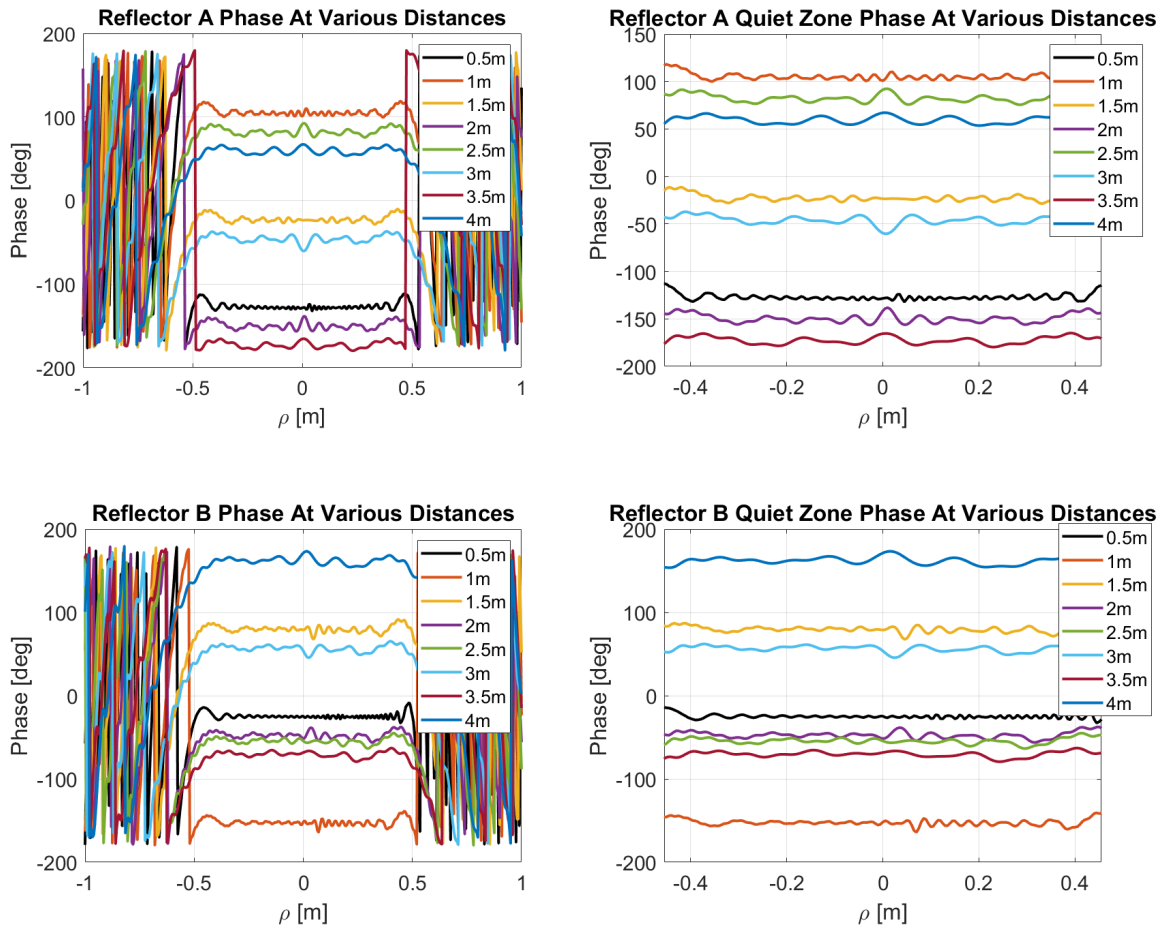

Figure 2.7: Phase cuts at various distances from the reflector to observe the uniformity of the phase in the quiet one for both Reflector A and Reflector B.

Figure 2.8 presents a more intuitive visualization to understand the experiment setup. Reflector A is pictured on top with the resulting phase cuts extending outwards, and Reflector B is pictured on the bottom with the corresponding results at the same distances. The variance of each of these phase cuts is calculated to quantify the difference between each reflector and over distance. Figure 2.9 features the resulting phase variance over distance.

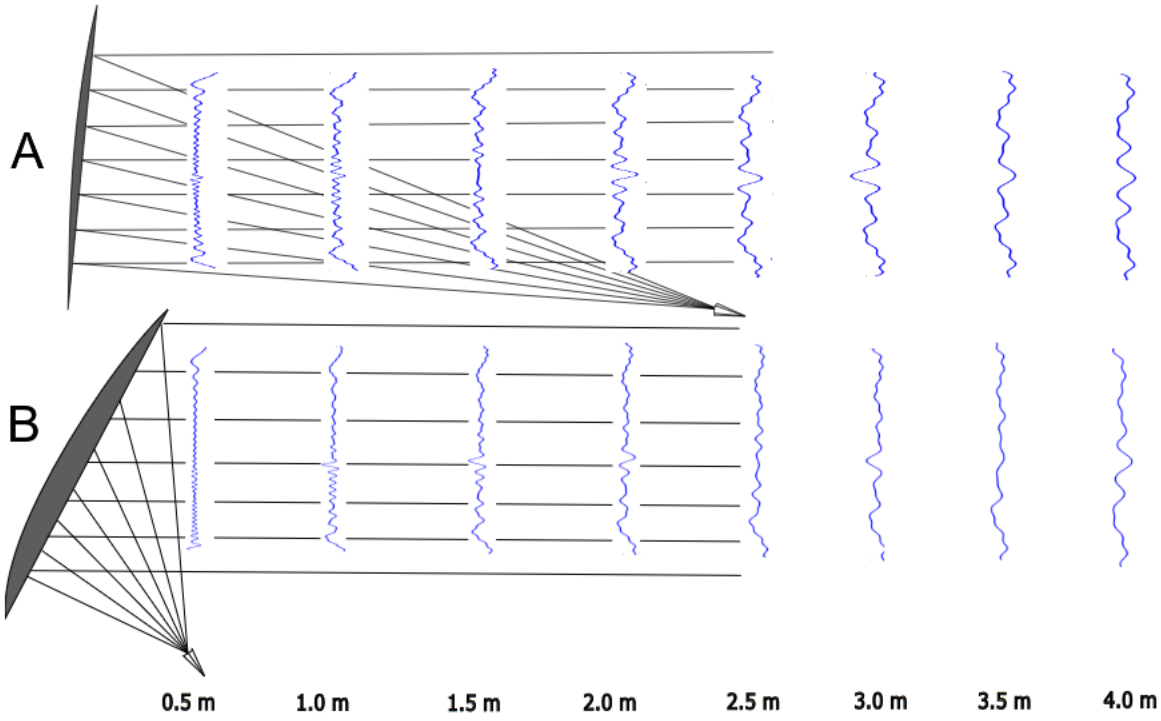

Figure 2.8: Phase cuts of the quiet zone for Reflector A (top) and Reflector B (bottom) for various distances away from the reflector as simulated by TICRA GRASP.

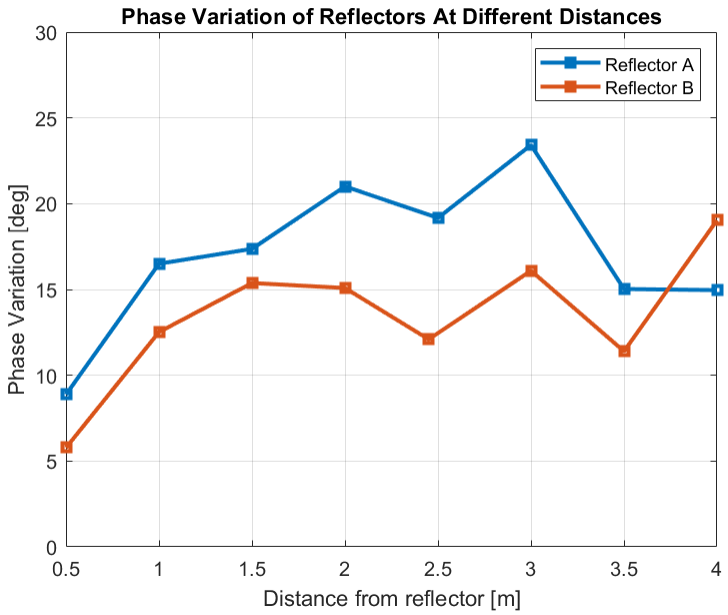

Figure 2.9: Variance of phase cuts of the quiet zone for Reflector A and Reflector B across various distances away from the reflector.

From the plot in Figure 2.9 it is apparent that Reflector B has less variation throughout the entire distance than Reflector A, which is based on the NSI range. This is surprising because at first glance is seems that the professionally designed reflector seems to be underperforming in comparison. While it is true that Reflector A has increased phase variance, and therefore a less perfect quiet zone, looking back on Figure 2.7 let's reassess the phase cuts. The Reflector A NSI-based design on average appears to have more symmetric phase patterns than Reflector B. For example, compare the phase cuts of each at a distance of 1 meter away and Reflector B has a more erratic design on one side (ρ: 0 to 0.45 m) than the other (ρ: -0.45 to 0 m). The 1-meter phase cut for Reflector A has a much more symmetric pattern across the center of the reflector (across the center point of the plot's x-axis). Other good comparison points are the patterns at 0.5 m, 1.5 m, and 3.5 m. Each of these shows the obvious distinction between Reflector A's fairly symmetric results and Reflector B's less symmetric results.

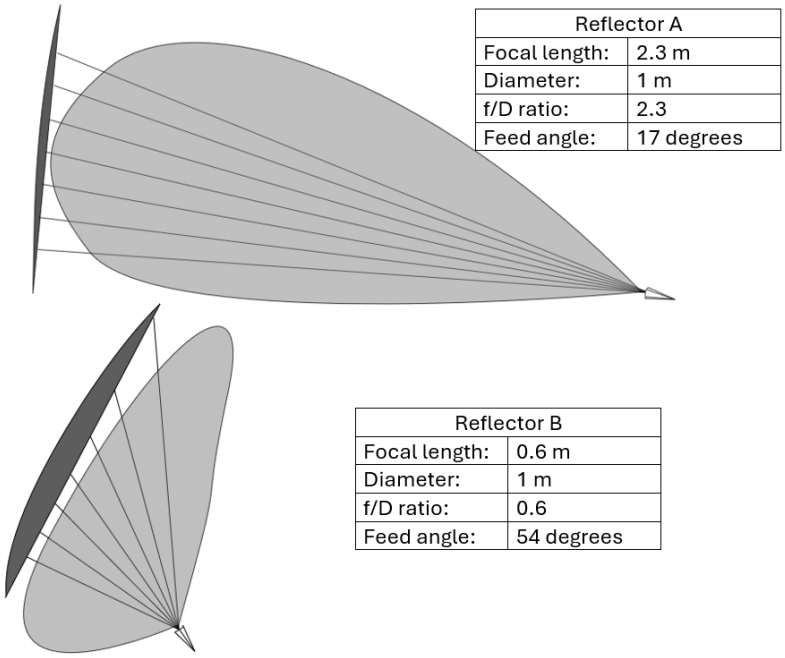

Figure 2.10: Sketched visualization of feed illuminating Reflector A (top) and Reflector B (bottom) to portray the effects of smaller and larger f/D ratios.

Why is there a notable difference in symmetry between the two designs? Figure 2.10 portrays a sketch to explain. Reflector A is further from the feed so it is illuminated more evenly than Reflector B. The larger f/D ratio also means that Reflector A is shallower, which also aids in the even illumination efforts. The focal length is smaller and, by extension, the feed for Reflector B is much closer, meaning the distance from the feed to the bottom of the reflector is much closer than the feed to the top of the reflector. The difference in feed distance across different points of the reflector causes the feed to illuminate the different points of the reflector at slightly different times, producing offsets in amplitude and phase. This causes an imbalance in illumination and lack of symmetry in the final phase patterns in the quiet zone for Reflector B. The effects are also exacerbated because the feed for Reflector B is close enough to the reflector that the emitted fields may still be reactive in nature as found in the near field distance. The feed placed further away allows for the signal to be less reactive in nature and less erratic upon contact with the reflector.

Despite the variance being lower overall for Reflector B, NSI most likely purposefully designed their system with a longer focal length to achieve increased symmetry. For the purposes of this work, a reflector with a larger f/D ratio in closer likelihood with Reflector A is examined and researched. A larger f/D ratio is chosen due to the trade-offs discussed in Section 2.2.2 in which amplitude taper and spillover efficiency are analyzed. As stated, the maximal gain is of less importance in the ambitions of this project and is sacrificed for other parameters. This trade-off dictates a larger f/D ratio be implemented.

Another interesting experiment is to simulate in TICRA the reflectors at a higher frequency to compare to with lower end frequency range of 20 GHz. For this purpose, the experiment was repeated utilizing the same reflector dimensions and simulated at 50 GHz instead of 20 GHz. Figure 2.11 presents the phase variance across the quiet zone distance for both frequencies in terms of electrical size.

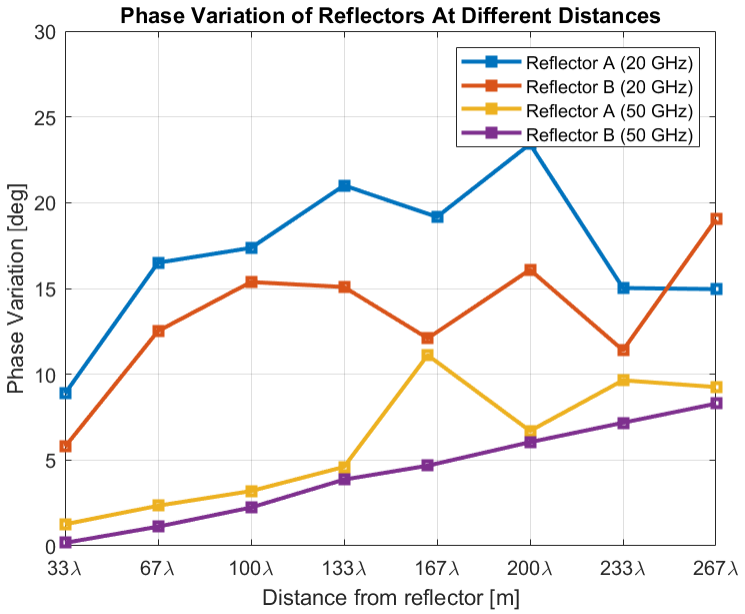

Figure 2.11: Variance of phase cuts of the quiet zone for Reflector A and Reflector B across various distances away from the reflector simulated at 20 GHz and 50 GHz.

The trend remains the same, with Reflector B providing less variation overall but the individual patterns consisting of less symmetry. Note that the variance across the quiet zone is significantly less for the 50 GHz simulations than for the 20 GHz simulations. This relates back to geometrical optics math which is the fundamental basis for all CATR reflectors. If the reflector could be infinitely large, it could collimate a spherical wavefront into a planar wavefront perfectly. However, realistically a practical reflector cannot be infinitely large, and the wavefront is only approximately planar. In this case, the reflector electrically appears larger to the 50 GHz wavefront compared to the 20 GHz wavefront. The 'larger' reflector performs better at creating more planar waves in the quiet zone.

2.2.4 Potential Feed Antennas

An important component of the CATR system is the feed antenna. It is essential to select the correct feed that best suits the system. Gain, beamwidth, taper level, and symmetry (as discussed in Section 2.2.3) are all characteristics to consider.

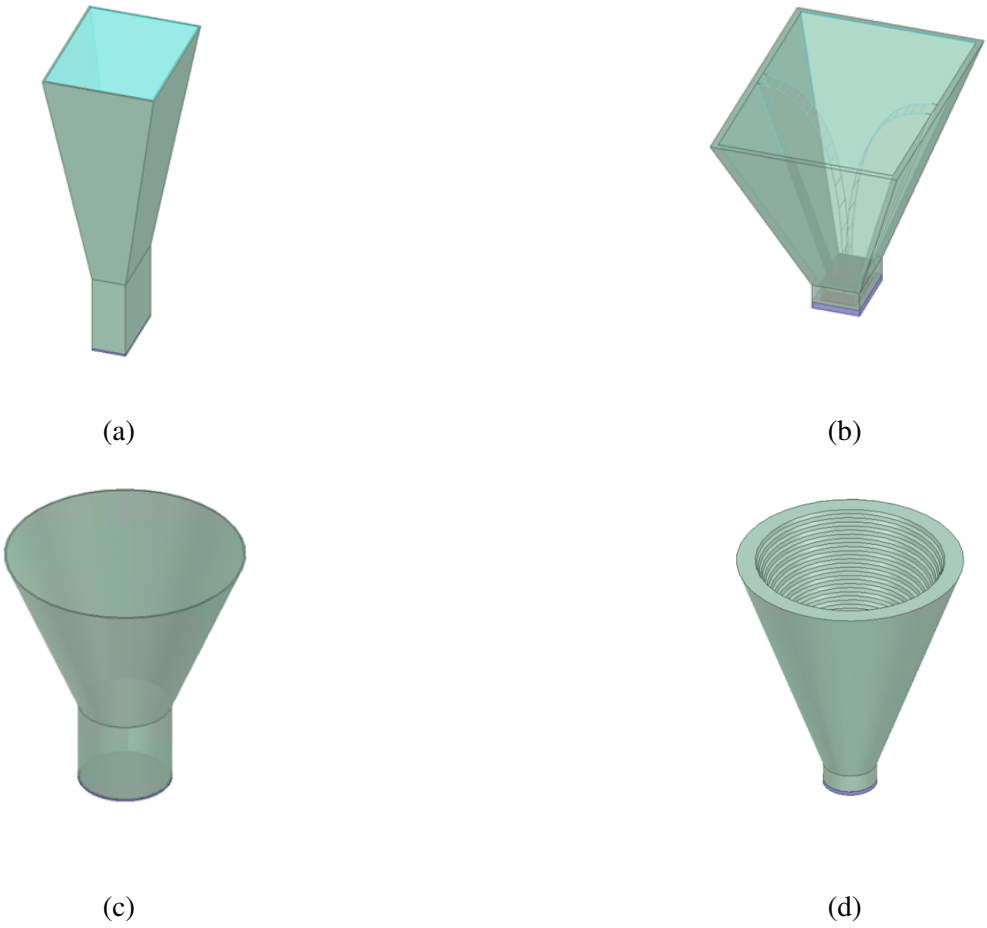

(a) (b)

(c) (d)

Figure 2.12: Various horn antenna feeds designed for 77 GHz modeled in HFSS: a) pyramidal horn b) dual ridged pyramidal horn c) conical horn d) corrugated conical horn.

It is not the reflector design alone that will determine the spillover levels, amplitude taper, and overall efficiency, but also the feeding mechanism. This section discusses various feeding options and analyzes the trade-offs.

To start this analysis, let's begin by observing four horn antenna types: pyramidal horn,

dual ridged pyramidal horn, conical horn, and corrugated horn antenna. Figure 2.12 displays the HFSS models for each of these horns. Horns are very common due to their simplicity in construction, ease of excitation, versatility, large gain, and preferred overall performance.

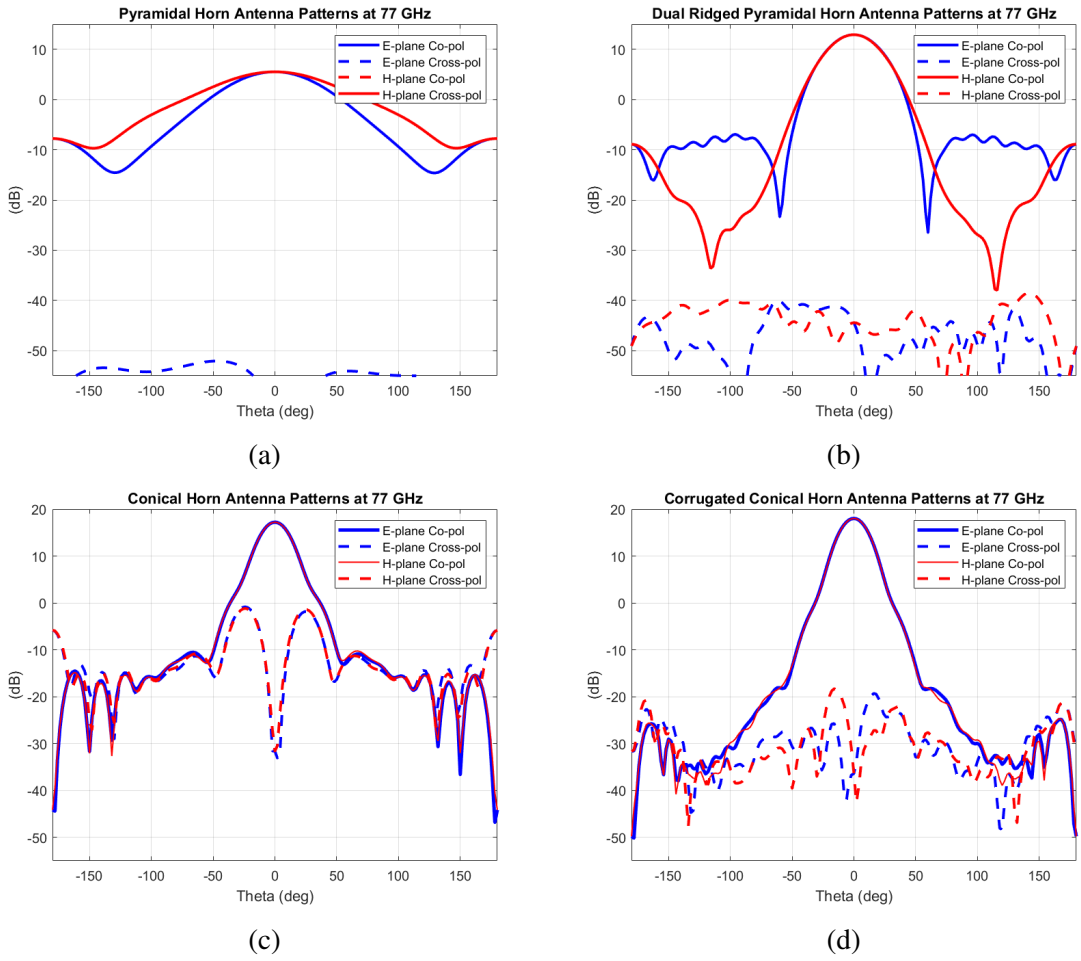

Figure 2.13: Radiation patterns of various horn antenna feeds designed for 77 GHz simulated in HFSS: a) pyramidal horn b) dual ridged pyramidal horn c) conical horn d) corrugated conical horn.

A horn antenna is an antenna that extends from a waveguide into a flared shape. The flared shape allows for better impedance matching to the surrounding free space ($\sim 377\Omega$) than a standard waveguide which has an abrupt discontinuity between the aperture and air.

This impedance mismatch causes increased reflection and limited propagation compared to the abilities of a horn antenna. The flare angle plays a considerable role in determining the gain and efficiency of the antenna. The conical horn gain, for a given length, increases by increasing the flare angle until it reaches a maximum, beyond which it starts to decrease because of the large phase variations over the aperture [43]. The most widely used horn is the pyramidal horn, which is flared in along all sides in both the E- and H-planes. Figure 2.13 displays the radiation patterns of the four antennas highlighted in Figure 2.12.

The pyramidal horn shows relatively wide beamwidth compared to the other options, but does have significantly lower cross-pol. Compared to the pyramidal horn, the dual-ridged horn is designed to be smaller. This is achieved because the ridges create capacitance effects that decrease the cut-off frequency of the dominant propagating mode (TE10) and increase the single-mode bandwidth. Viewing the ridges as a portion of the waveguide in Figure 2.14(a), it can be viewed that the actual length of a waveguide a is not the acting geometry and, rather, it is the effective length of the waveguide a_{eff} that controls the horn and its modes. This larger effective length allows for a lower TE10 mode while not sacrificing by increasing the physical size of the structure. This is displayed in Figure 2.14(a). Boundary conditions explain that the E-field approaching the ridges orthogonally induces an electric current in the ridges, as seen in Figure 2.14(b). In summary, the dual-ridged horn has the design advantage of achieving lower cut-off frequencies, wider bandwidth, and smaller form factor. However, the size of the feed is not a limitation in our CATR system.

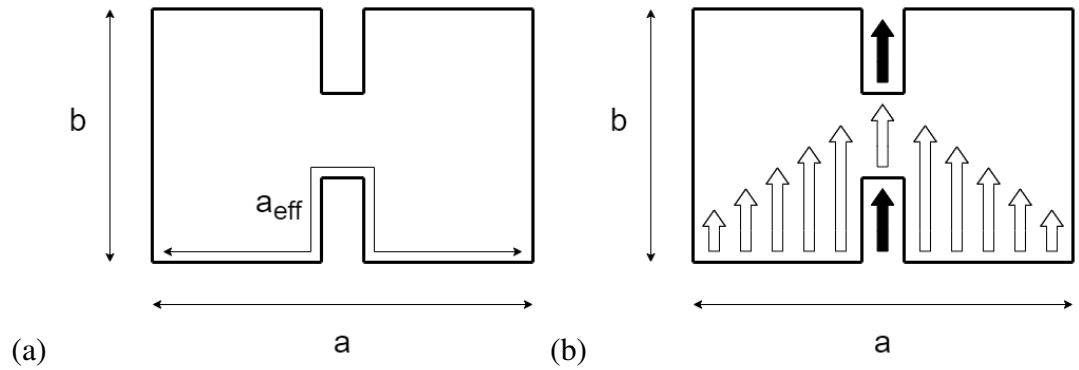

Figure 2.14: Front-end view of a dual-ridged horn antenna to analyze in the context of a waveguide. (a) Dimensions of dual-ridged horn antenna, including actual length a and effective length a_{eff}. (b) E-field behavior of dual-ridged horn antenna with boundary conditions compounding the energy in the center along the ridges (black arrows indicating electric current induced by boundary conditions.)

The pyramidal and dual-ridged do not have good alignment between their E- and H-plane patterns compared to the conical and corrugated conical horns. The pyramidal horn has different sizes in the E- and H-cuts which exacerbates the difference, but even a square aperture would not produce near-identical patterns. The dual-ridged horn also experiences differences between the patterns especially due to the fact that the ridges are only in the E-plane. The conical horns have much better alignment between the E- and H- patterns because the dimensions themselves are more symmetrical, but also because the circular nature means fewer modes are excited. With fewer modes excited over a given frequency range, there is less variation in the fields. As discussed in Section 2.2.3, symmetrical feed patterns are desirable to obtain symmetrical patterns in the quiet zone. Therefore, based on the simulation patterns in Figure 2.13, the conical or corrugated conical horn appear to be better options than the pyramidal or dual-ridged horns due to their elevated symmetry. The conical horns also have higher gains and are more directive.

The downside to the conical horn is the much higher cross-pol than the pyramidal or dual-ridge options. The conical design is plagued with a higher cross-pol because the circular shape allows for a higher induced current along the rim of the aperture. The higher

current contaminates the purity of the emitted signal and unwanted levels of cross-pol occur. In the face of this problem, the solution lies in the design of the corrugated horn antenna which has grooves along the inside surface of the horn. These grooves, which are electrically small compared to the wavelength of operation, enable very low cross-pol over the bandwidth and also low side lobes. Due to boundary conditions, the electric field along the sides of the conical horn is zero. There is low resistance along the edge. The corrugated horn's grooves have a large impedance compared to the conical counterpart. With high impedance along the rim, very little current magnitude is induced in the same direction and the current level no longer poses a threat to increase the cross-pol. The grooves cause many edge diffractions that bounce in many directions and, when summed, average to very little. This means that the back lobes - which are heavily dependent on diffractions - are reduced [44]. Kay [45] reasons that the grooves present the same boundary conditions to all polarizations, tapering the field distribution at the aperture in all planes and eliminating spurious diffractions at the edges of the aperture

Another parameter to consider for CATRs is the taper level of the feed. The taper level is defined as the difference in power from the peak of the main lobe to the first shoulder of the main lobe [42]. The shoulder is different than a side lobe. For example, Figure 2.13c has a shoulder that occurs at -30 degrees and +30 degrees where a slight bulge occurs in the main lobe. In this case, the shoulder occurs at 15 dB down from the peak, so the subsequent taper is -15 dB. The next section continues the discussion on tapers, but in general, to a certain point, a larger absolute value taper is desired. In this case, these simulation results show that the corrugated structure has a better taper than the plain conical, although it is likely that this varies across different specific designs.

Analysis of these antennas concludes that the corrugated conical horn antenna is the ideal option for CATR application. Horn antennas are desirable due to their high directivity and prominence in production as widespread options. The conical designs are composed

of symmetrical patterns across the electric and magnetic fields, and the corrugated design specifically reduces the cross-polarization levels to an acceptable level. Table 2.1 summarizes the advantages and disadvantages of each.

Table 2.1: Horn antenna feeds comparison

Horn antennas				
	Pyramidal	Dual Ridged	Conical	Corrugated Conical
Gain (dB)	5.5	12.9	17.2	18.0
HPBW (deg)	76	44	24	24
Taper (dB)	-	-	-15	-17
Symmetry	Low	Medium	High	High

Further HFSS simulations were performed on the four horns to visualize the phase. The simulation setup included obtaining the near field radiation at many points of a rectangular plane 8 inches long and 4 inches tall with the feed placed at the edge of the plane. Figure 2.15 outlines the resulting phase of the near field patterns. It can be observed that all of the feeds do look relatively planar after a certain point. This is probably due to the fact that each of the apertures is relatively small and there is not a significant phase difference across the aperture. According to Balanis [8], the gain of a horn increases as the flare angle increases until a certain point when the aperture becomes too wide and the phase variations across the aperture become too much. In this case, all of the feeds are appropriately designed to eliminate this complication.

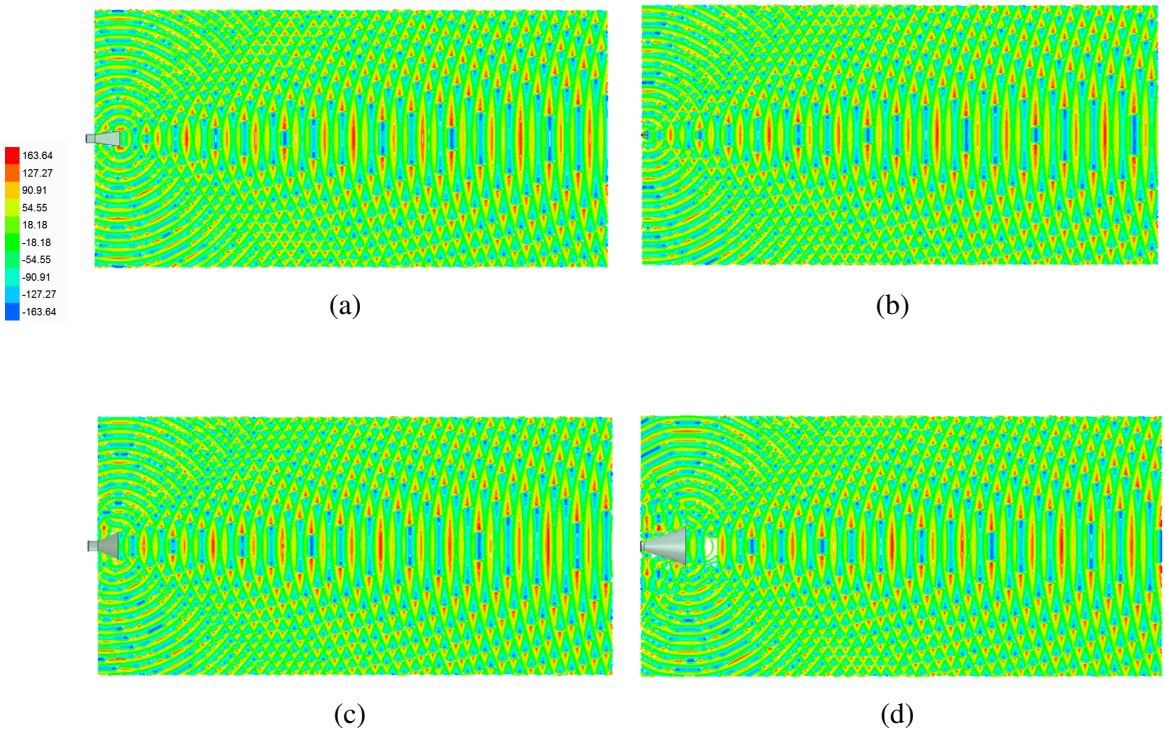

Figure 2.15: Simulated phase patterns of horn antennas in HFSS on cut planes 8 inches wide and 4 inches tall. (a) pyramidal (b) dual-ridged (c) conical and (d) corrugated conical.

While this discussion has verified through simulation results that the corrugated conical horn is the preferred feed for CATR, it is important to note that corrugations for high-frequency antennas are extremely difficult to fabricate and tend to be very lossy upon physical realization. With the accepted requirement being 10 or more corrugations per wavelength, the grooves at mmWave frequencies and above are incredibly small, and the cost of manufacturing is high [43]. Chapter 4, which highlights each component of the CATR system, discusses the available feed that was utilized.

2.2.5 Feed Antenna Taper

Another case study regarding the feeding probe is completed in this section. Simulated feeds of different tapers are compared. In this case, the taper of a feed describes the beamwidth in terms of the power reduction of the radiation pattern from the peak (at 0 degrees) to the subtended angle. Figure 2.16 presents the simulated Gaussian radiation patterns. The feed with a 20 dB taper, decreases from the peak value by 20 dB at the subtended angle. In other words, if the reflector has a subtended angle of 70 degrees, then the radiation pattern will drop 20 dB from the peak power to -35 degrees to 35 degrees in both the azimuth and elevation angles.

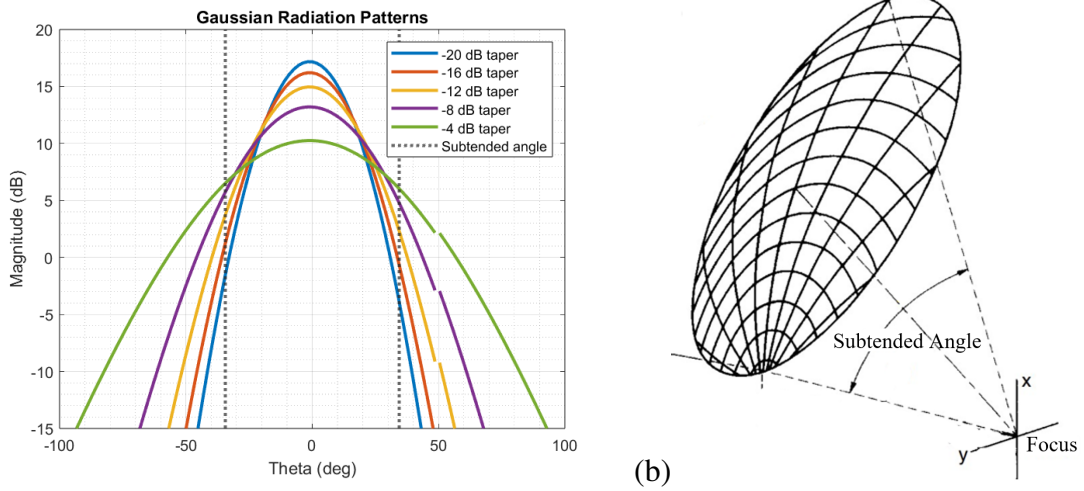

(a) (b)

Figure 2.16: (a) Gaussian radiation patterns for feeds of different taper levels. (b) Diagram of reflector showing the definition of subtended angle [42].

The magnitude and phase results in the quiet zone for feeds of different tapers are shown. The results are found by TICRA GRASP's physical optics simulations. Figure 2.17 displays the 2D vertical cuts in the quiet zone for scenarios with feeds ranging from tapers of -20 dB to -4 dB. A vertical cut is extracted to observe both the magnitude and phase.

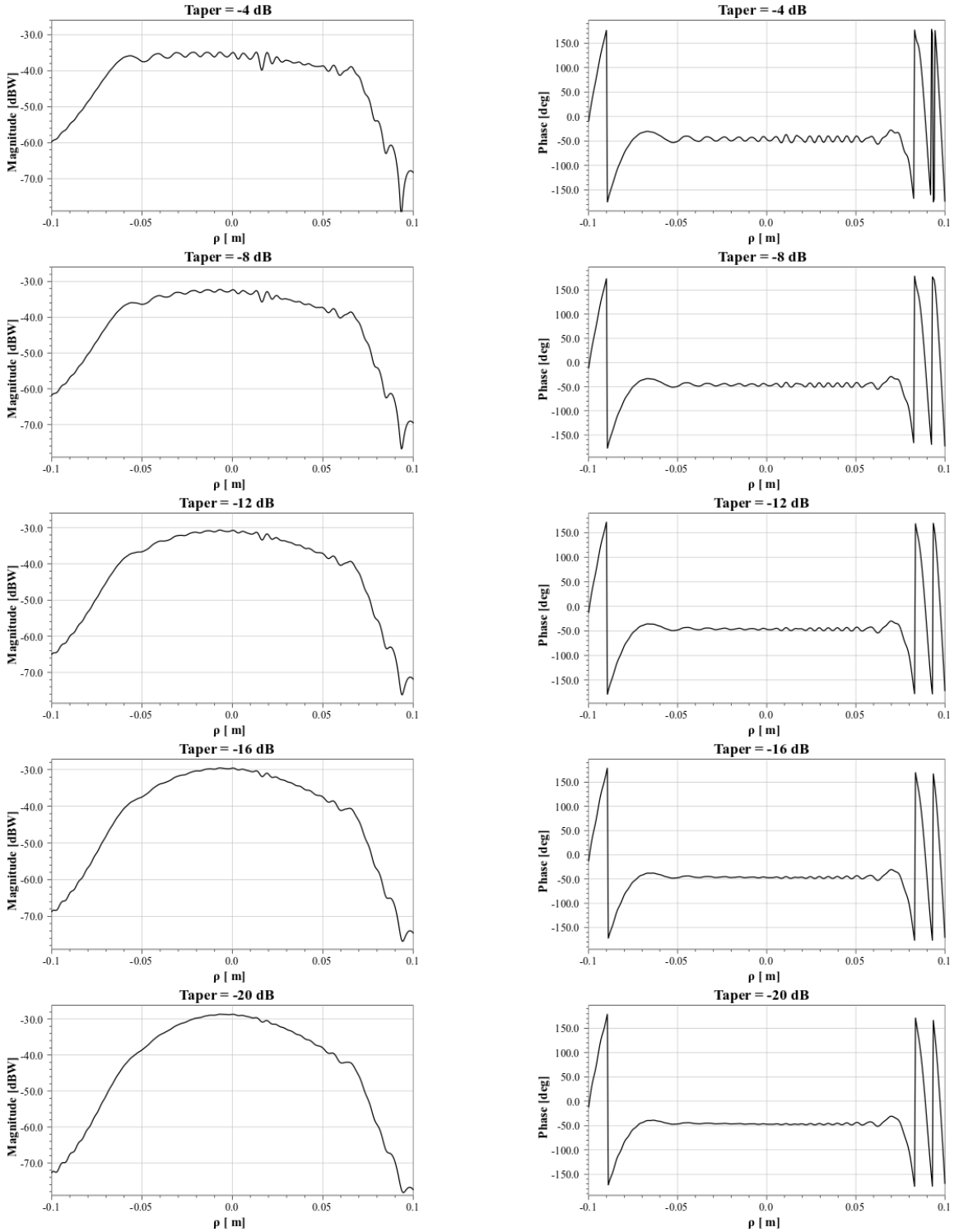

Figure 2.17: Simulated magnitude and phase-cut patterns of a CATR system with Gaussian feed of various tapering levels. The x-axis is the distance of the vertical cut of the quiet zone in meters. The magnitude varies more with a steeper taper while the phase varies less with a steeper taper.

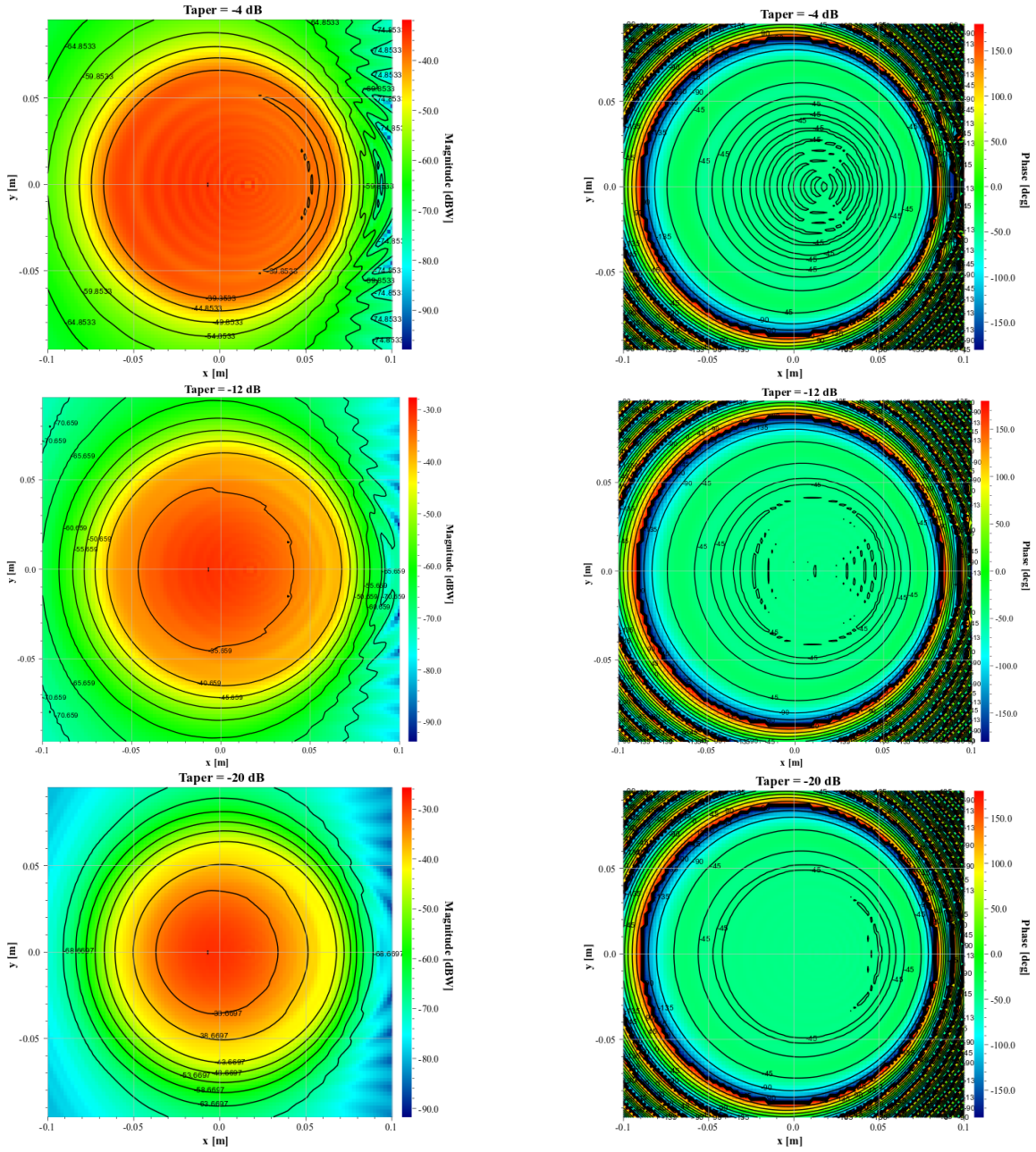

Figure 2.18: Simulated magnitude and phase grid cut patterns of a CATR system with Gaussian feed of various tapering levels. The magnitude varies more with a steeper taper (more directive feed antenna) while the phase varies less with a steeper taper.

Recall from Section 2.1.3 that the variation of the magnitude in the quiet zone is measured by looking at the variation of the second-degree polynomial of the data [35]. From

Figure 2.17 it is apparent that the increased directivity of the feed (larger taper) results in a steeper drop-off of the magnitude.

Comparing the plots of the magnitude yielded by the 4 dB and 20 dB tapered feeds, the magnitude brought about by the lower taper is relatively flat from -0.05 to 0.05 meters. The magnitude of the scenario including the 20 dB tapered feed has dropped off nearly 10 dB at -0.05 and 0.05 meters. This is even more apparent in Figure 2.18, which shows a 3D image of the quiet zone rather than one vertical cut. The magnitude in the quiet zone tapers off significantly quicker with more directive feeds.

Next, consider the phase in Figures 2.17 and 2.18. As the feed antenna taper increases, the phase stabilizes. The phase variation across the quiet zone of the scenario with the 4 dB tapered feed is 17 degrees, compared to the identical scenario with a 20 dB taper which has less than 2 degrees.

This introduces an interesting dilemma, as the magnitude variation in the quiet zone can be improved by employing a less directive antenna at the sacrifice of dramatically worsening the phase variation. Figure 2.19 presents the trade-offs by plotting the variation of the phase and magnitude over the feed antenna taper.

It is difficult to find a suitable medium with both the amplitude and phase meeting both of the optimal guidelines of less than -0.25 dB amplitude variation and less than 11.25 degree phase variation (as outlined in Section 2.1.3). However, recall that the IEEE standards highlighted that the amplitude requirements may vary based on application. Given the findings of Figure 2.19 for a reflector with a subtended angle of 70 degrees, ideally a taper between 6 and 9 dB may be optimal. The quiet zone may be slightly smaller, but the phase will have better variation levels.

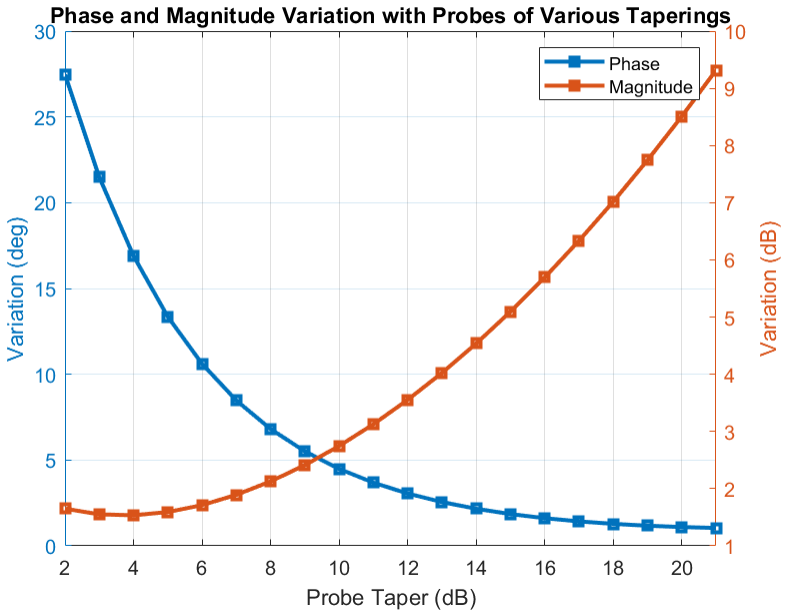

Figure 2.19: Variation of phase and magnitude for Gaussian feeds of different taper levels. The variation is calculated over the distance ρ of -0.05 to 0.05 meters which can be observed in Figure 2.17.

The optimal quiet zone technically varies with the different feed antennas. For example, the 20 dB tapered feed, causes such extreme variation of the magnitude that realistically -0.05 to 0.05 meters would not be an adequate quiet zone size. The quiet zone would need to be defined as smaller, so the magnitude variation is not so extreme within the quiet zone. For the purposes of this experiment, the quiet zone is consistently defined as bounded by -0.05 and 0.05 meters (10 cm total). Thus, another way to look at the impact of the different feed taperings is the change in the quiet zone size rather than the direct worsening of the quiet zone. This can be related to the similar trade-off discussed in Section 2.2.3, in which the efficiency of the system is evaluated by the quiet zone size given the size of the reflector. A large reflector is inefficient if the quiet zone yielded is unreasonably small.

The reason the magnitude and phase variation are inversely impacted by the feed antennas of different beamwidths is mainly due to edge effects. Figure 2.20 displays the set-up with two feeds of different tapers.

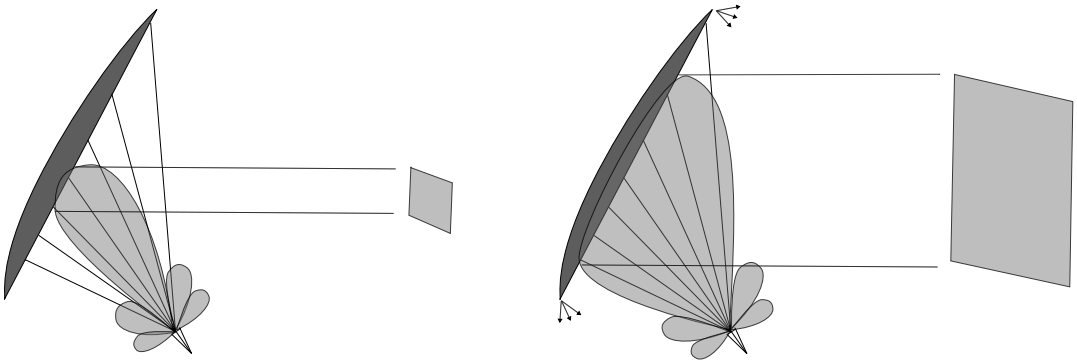

Figure 2.20: Illustration of how feeds with different tapers and beamwidths can impact the compact range set-up. The scenario on the left has a large taper and the setup on the right has a small taper.

It is illustrated that the narrow beamwidth only has consistent contact with the reflector for a smaller area, and thus the quiet zone is smaller. Otherwise, the feed's radiation pattern's contact with the reflector varies too much which causes the variation of the magnitude in the quiet zone. The smaller taper, and wider beamwidth, covers a larger area of the reflector with even contact and results in a larger quiet zone with stable magnitude. However, the radiation pattern is nearer to the rim and introduces more edge diffractions which causes increased variation in the phase.

This trade-off as well as the others discussed in this chapter are considered in the final design of this project which is covered in the next chapter. There are many aspects to balance and oftentimes compromises are made in the best interest of overall success.

2.3 Summary

To summarize, Chapter 2 has outlined the theory behind compact antenna test range reflectors and expounded upon many potential trade-offs involving the reflector design and feed to progress toward a successful compact antenna test range. Aspects of the reflector such as the optimal depth of the reflector and the preferred f/D ratio are explored to maxi-

mize efficiency while minimizing spillover, and observing the impact in the quiet zone of different designs. The feed is also discussed at length as various horn antennas are analyzed as potential options before concluding that a feed with a symmetrical pattern of sufficient directivity is ideal. However, there is not a perfect answer for the beamwidth of the feed as too narrow will increase the magnitude variation in the quiet zone, diminishing the quiet zone size and, thus, efficiency. On the other hand, too broad of beamwidth will invite adverse edge diffractions, which also detracts from the system performance. A moderate f/D ratio is selected for the reflector design and the Eravant W-band horn antenna is satisfactory considering the simulation conclusions.

Chapter 3 dives further into the mathematical theory of the reflector and describes the design process. The edge treatments, serrations and blended edges, are elaborated on mathematically. Much roughness analysis was performed considering the reflector will be operating at W-band frequencies and above. This is discussed at length, as well as the fabrication process that allows the roughness criteria to be met. Chapter 4 delineates the aspects of the compact antenna test range system, ranging from the vector network analyzers to the AUT. Once the components of the system are explained, Chapter 5 will outline the results of the setup.

Chapter 3

Reflector Design and Implementation

The reflector design in analyzed in-depth in this chapter. Whereas the previous chapter illuminated high-level reflector design trade-offs, this chapter dives into the mathematical design process. First, the curvature for an offset reflector and corresponding parameters are defined. Next, the project ultimately employs rolled edges, so this topic is talked about at length. Various questions on rolled edges are answered. What is the difference between elliptical and blended edges? Why is one better? How is this best designed? After designing for 2D, how does one expand to 3D? Examples are included.

Once the reflector design is finalized, it is important to discuss the fabrication process and possible limitations. The main challenge for high frequencies is the surface roughness. Obviously, as the surface roughness increases the upper frequency bound of the system diminishes. This chapter provides TICRA GRASP simulation results to quantify the upper frequency bound for different surface roughness levels. This project aims to prove that 3D printing reflectors are a viable option, thus it must first be proven that the 3D print and reflective metallic coating can meet the surface roughness requirements. 3D printing filaments such as PLA, ABS, and resin are compared as well as the treatment procedures such as sanding and copper plating. The final fabrication process is included.

3.1 Reflector Curvature Design

This section outlines the design process for the curvature of an offset-fed parabolic reflector. As previously explained, an offset geometry is selected to ensure that the feed does not obstruct the quiet zone, as seen in a front-fed parabolic reflector. Cassegrain and Gregorian designs were deemed needlessly complex for the proposed goal of mmWave measurements. According to Olver [12], a single offset compact range can achieve a quiet zone with exceptionally low amplitude and phase ripples. The weakest parameter is the cross-polar level which is typically about -30 dB. This is due to the fundamental cross-polarisation introduced by the offset geometry.

Figure 3.1 displays the offset-fed parabolic reflector geometry. The reflector is a piece of a larger parent parabaloid. The parent parabolic is asymmetrical, but the portion of the parabaloid that the reflector consists of is deliberately chosen to be offset from the axis. In this way, the focus, f, with the feed remains in the same position but since the reflections will only be occurring above the feed instead of all around the feed, there is no blockage from the feed. The feed is tilted to be pointed at the center of the reflector. ψ_0 describes the angle from the axis of the parabola to the center of the reflector. The offset of the lower rim, D', is given as

$$D' = H - D/2 \tag{3.1}$$

where H is the offset of the reflector center and D is the diameter of the projected aperture, as seen in Figure 3.1. From there it is possible to represent ψ_0, the angle from the z-axis the focal point lies on to the center of the rim, as

$$\psi_0 = \tan^{-1} \frac{16fH}{16f^2 + D^2 - 4H^2} = \tan^{-1} \frac{2f(D + 2D')}{4f^2 + D'(D + D')}. \tag{3.2}$$

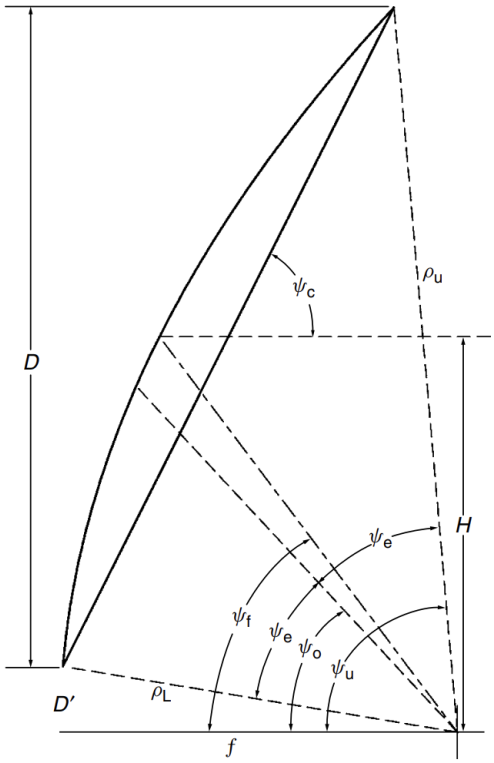

Figure 3.1: Parameters of an offset parabolic reflector, as defined by [42].

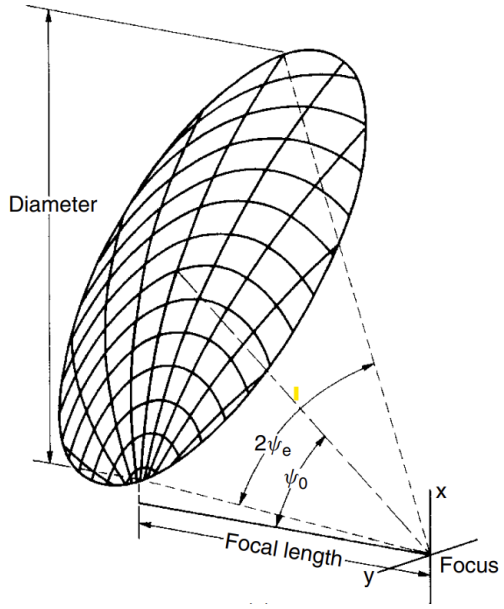

Figure 3.2: Perspective view of offset parabolic reflector geometry [42].

If ψ_0 is defined as the center point, then ψ_e can be described as the angle from the center of the rim to the edge of the rim. The reflector subtends an angle of $2\psi_e$ from the center of the rim, ψ_0. The half cone angle is

$$\psi_e = \tan^{-1} \frac{8fH}{16f^2 + 4H^2 - D^2} = \tan^{-1} \frac{2fD}{4f^2 + D'(D + D')}. \tag{3.3}$$

Using these equations to compose the initial design, it is also important to recall that adding the offset angle, D', alters the critical f/D ratio as

$$\frac{f}{D} = \frac{\cos\psi_e + \cos\psi_0}{4\sin\psi_e}. \tag{3.4}$$

Although the feed remains at the focus point, it must be rotated at an angle of ψ_f, calculated as

$$\psi_f = 2\tan^{-1}\frac{H}{2f} = \tan^{-1}\frac{2D' + D}{4f}. \tag{3.5}$$

It is also important to note that the rim lies in a plane at angle ψ_c from the z-axis.

$$\psi_c = 2\tan^{-1}\frac{2f}{H} = \tan^{-1}\frac{4f}{2D' + D} \tag{3.6}$$

The reflector rim is shaped as an ellipse with major axis a_e and minor axis b_e defined as

$$a_e = \frac{D}{2\sin\psi_c} \tag{3.7}$$

and

$$b_e = \frac{D}{2}. \tag{3.8}$$

From this point forward note that $L = 2a_e$. For the purposes of this report, the major

axis is aligned along the x-axis and the minor along the y-axis with the reflector rim laid on the $x - y$ plane. The corresponding reflector depth $d(x, y)$ is found as

$$d(x,y) = A\sqrt{1 + \frac{xD^2\sqrt{L^2 - D^2}}{1} + \frac{D^2(L^2 - D^2)}{4f^2L^4}(\frac{D^2}{4} - y^2) - 1 - \frac{xD^2\sqrt{L^2 - D^2}}{2fL^3}} \tag{3.9}$$

where

$$A = \frac{2fL^3}{D(L^2 - D^2)} \tag{3.10}$$

The deepest point d_{max} is determined by

$$d_{max} = \frac{D^3}{16fL} \tag{3.11}$$

and occurs at the point

$$x_b = -\frac{D^2\sqrt{L^2 - D^2}}{16fL} \tag{3.12}$$

along the x-axis. The radial distance from the focus to the upper and lower bounds of the rim are denoted as

$$\begin{bmatrix} \rho_U \\ \rho_L \end{bmatrix} = \frac{fL^2}{D^2} + \frac{D^2}{16f} \pm D(\frac{L^2}{D^2} - 1). \tag{3.13}$$

Table 3.1 outlines the variables used in these equations.

Table 3.1: Reflector geometry symbol definitions

Symbol definitions	
D	Diameter of the projected circular aperture of the parabolic main, or parent, reflector
D'	Offset distance; distance from the axis of symmetry to the lower reflector edge
H	Offset of reflector center; distance from axis of symmetry to center of reflector; $\frac{D}{2} + D'$
f	Focal length
ψ_0	Angle from the axis of the parabola to the center of the cone of the reflector, reflector subtends an angle ψ_e about this centerline
ψ_e	Half cone angle
ψ_f	Angle when the feed is pointed at the reflector point corresponding with the aperture center
ψ_c	Angle from which the rim lies in a plane from the z-axis
a_e	Length of major axis of reflector rim ellipse
b_e	Length of minor axis of reflector rim ellipse

A simple initial design based on these equations was created and simulated in HFSS. The initial parameters are set as follows: the projected diameter of the reflector, D, to 15 cm, the focal length, f, to 10.125 cm, and the height offset, D', as D/8 or 1.875 cm. The diameter of the parent parabaloid is $2D + 2D'$ or 33.75 cm. Calculating Equations 3.2 and 3.3, and plugging the results into Eq. (3.4) yields the f/D ratio as 0.6.

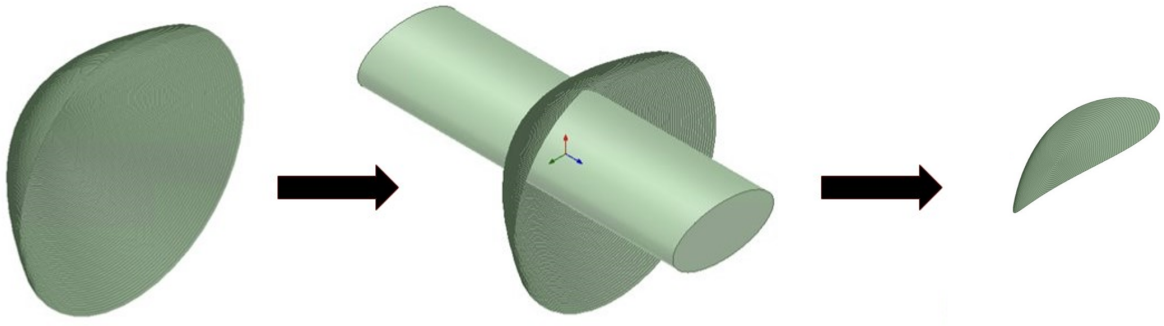

Figure 3.3: Step by-step demonstration of how reflector is constructed in HFSS to demonstrate the elliptical portion of the parabaloid used.

The HFSS construction of the reflector is demonstrated in Figure 3.3. Once the parent paraboloid is constructed in HFSS, an elliptical prism is built to intersect it. The bottom-most point of the elliptical prism is at height D' above the xy plane, and the major and minor axes of the ellipse are 10.3 cm and 7.5 cm, as calculated from Eq. (3.7) and Eq. (3.8). In HFSS the parent paraboloid and the elliptical prism are commanded to intersect, meaning the new body is merely the elliptical piece of the parent paraboloid. This is the reflector. The original f/D ratio of the parent reflector is 0.3 (a relatively deep dish), but due to the offset, the f/D ratio of the reflector is calculated from Eq. (3.4) as 0.6.

A horn antenna is created, placed at the focal point of the parent paraboloid, and pointed to the reflector at angle ψ_f. Figure 3.4 displays the phase results along the cut plane where ψ_f intersects the reflector. This correlates to the aperture center or the center of the quiet zone. Figure 3.4 also shows the phase along a line that runs through the center of this cut plane. The phase is seen as jagged and irregular until it reaches the minimum distance away from the reflector where plane waves begin to form.

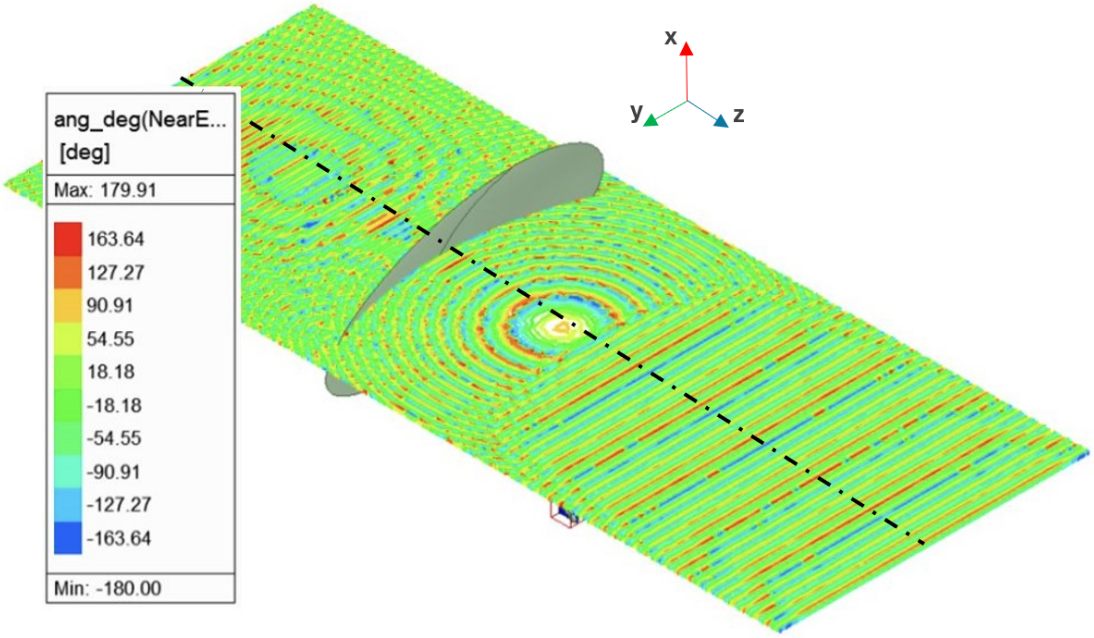

(a)

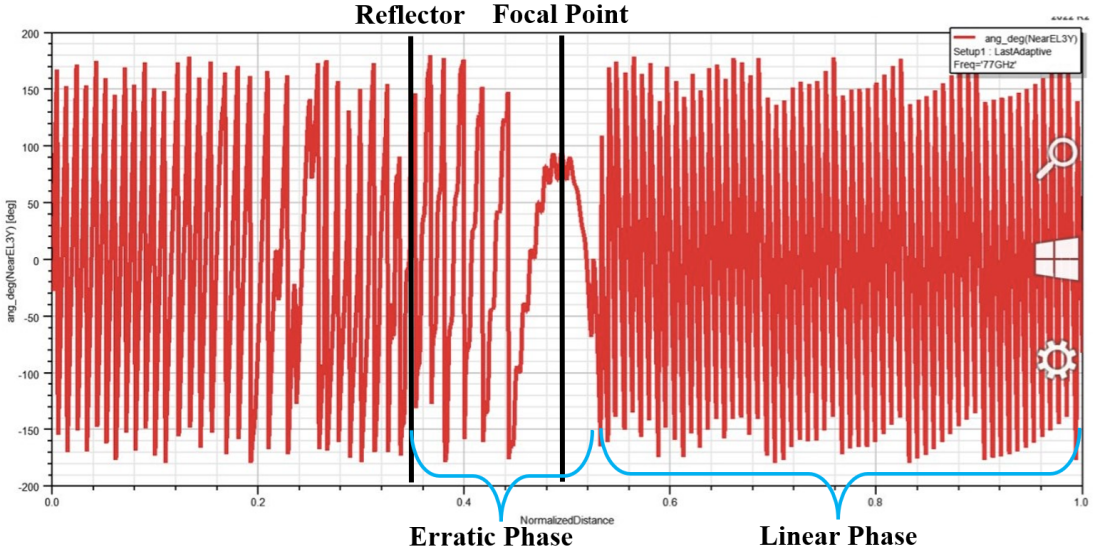

(b)

Figure 3.4: (a) The resulting simulated phase after the feed is placed at the focus and pointed at an angle of ψ_f. The phase becomes linear at a certain point. (b) The resulting simulated phase along the dotted line through the center of the model along the z-axis. The phase evens out and becomes acceptable for measurements after a certain point.

3.2 Reflector Rolled Edge Design

A method employed to minimize edge diffractions and avoid the distortion of a planar wavefront is the use of rolled edges on the reflector. With this distortion level reduced, the measurements will be more accurate and allow for lower cross-pol levels to be measured on AUTs [12]. The rolled edges on reflectors are extensions of the reflector surface to deflect undesired signals away from the quiet zone; the farther these undesired signals are forced away from the quiet zone, the less negative influence they can inflict on it. This can be done by having the surface smoothly deviate from a parabola to a more convex shape pointing away from the quiet zone. An example can be seen in Figure 3.6. However, if the transition from the parabola to the rolled edge is too quick, then new diffraction edges will appear [46]–[50].

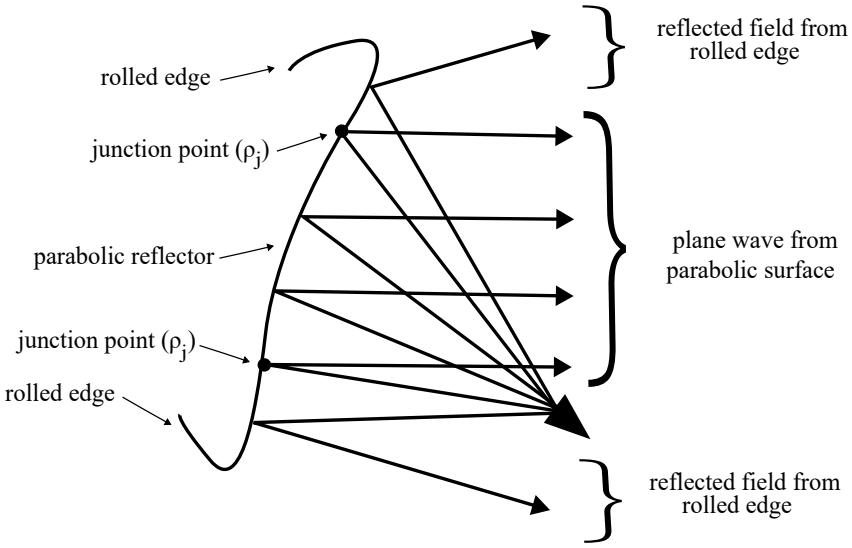

Figure 3.5: Reflected fields of rolled edge reflectors.

It is important to differentiate between a rolled edge and a blended rolled edge. A rolled edge is defined as an elliptical or similar convex surface added along the reflector rim in a

smooth and continuous manner. Rolled edge is an umbrella term. Elliptical and blended edges are both types of rolled edges. As seen in original designs in the 1980s, even if the surface is continuous there can be a discontinuity in the transition between the paraboloid and the rolled edge, due to the *difference in the radius of the curvatures*. A traditional rolled edge, such as an elliptical edge, is discontinuous at the junction, but a blended rolled edge can make the radius of curvature continuous across the junction. The parabola is a concave surface when viewed from the focus whereas the ellipse is a convex surface, so the radii of curvature on either side of the junction can be interpreted as having different signs in addition to being discontinuous in magnitude. Consequently, the reflected fields from the two surfaces are not equal and a diffracted field is created at the junction. Although not explained in this work, the expression for this diffracted field is given by Chu [50]. Figure 3.6 shows the comparison between a blended edge and an elliptical edge.

As seen in Figure 3.6, ρ_j is the junction point: the point at which the purely parabolic section ends and the rolled edge begins. The radius of curvature of a parabola at the junction point ρ_j is

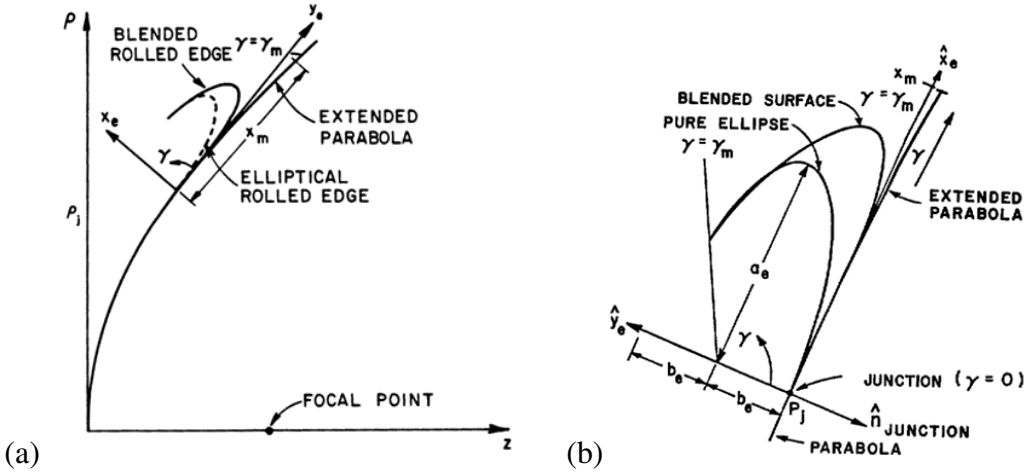

Figure 3.6: Rolled edge parameters taken from (a) [25] and (b) [51].

$$R_c^{parabola} = 2F\left[1 + \frac{x_j^2 + y_j^2}{4F^2}\right]^{3/2} \tag{3.14}$$

compared to the radius of curvature of an ellipse at point ρ_j is

$$R_c^{ellipse} = \frac{a_e^2}{b_e}. \tag{3.15}$$

Applying a blended rolled edge ensures that, although the slope of the surface appears smooth, the radius of curvature is also smooth and, thus, the reflected fields from the two surfaces are more equal.

3.2.1 2D Design Method

This section will follow Gupta's [25], [51] procedure to design blended rolled edges for minimal surface discontinuities. This procedure minimizes the diffraction fields in the transition between the paraboloid and the rolled edge surface [25]. In the search for a seamless transition between the parabola and the ellipse, four parameters are varied. The major axis of the ellipse a_e and the minor axis b_e, are promising variables to start with. One can increase a_e and decrease b_e to decrease the discontinuity in curvature radius. However, increasing a_e too much will cause the rolled edge to look too large, and decreasing b_e too much will create too sharp of an edge. A compromise is needed for optimal designs. The minimum radius of curvature of the portion of the reflector illuminated by the probe (i.e. excluding the shadow region of the reflector which is discussed in the next section) must be less than $\lambda_{max}/4$. The values a_e and b_e determine the radius of curvature, so this rule of thumb concerning $\lambda_{max}/4$ also constrains these values in the design process. The next variable, as can be seen in Figure 3.6, is the length of the portion of the parabola used in blending, x_m. Lastly, the blended rolled edge can be described in terms of the parametric angle γ, varying from 0 to γ_m. The variable γ_m defines how much of the ellipse is used

as the rolled edge. The larger the γ_m value, the further the rolled edge continues to curl behind the parabola. Gupta's [25] defines the following characterizing equations in the ρz plane with the focal point of length F placed along the z-axis.

Start simply by defining the equation of a parabola as

$$z = \rho^2/4F. \tag{3.16}$$

The junction point along the ρ-axis between the parabola and the rolled edge is referred to as ρ_j. Eq. (3.16) defines the reflector surface for $\rho \leq \rho_j$. The portion of the reflector for $\rho > \rho_j$ is defined as

$$\rho_{ellipse}(\gamma) = (a_e \sin\gamma)x_{p2} + b_e(1 - \cos\gamma)y_{p2} + p_j \tag{3.17}$$

and

$$z_{ellipse}(\gamma) = (a_e \sin\gamma)x_{p3} + b_e(1 - \cos\gamma)y_{p3} + z_j \tag{3.18}$$

in the ρ and z axes respectively, where

$$x_{p2} = 2F/(p_j^2 + 4F^2)^{1/2} \tag{3.19}$$

$$x_{p3} = p_j/(p_j^2 + 4F^2)^{1/2} \tag{3.20}$$

$$y_{p2} = p_j/(p_j^2 + 4F^2)^{1/2} \tag{3.21}$$

$$y_{p3} = -2F/(p_j^2 + 4F^2)^{1/2} \tag{3.22}$$

and

$$z_j = p_j^2/4F. \tag{3.23}$$

Recall that the ideal transition is not solely parabolic nor solely elliptic, but a blended combination between the two. Eq. (3.17) and Eq. (3.18) can be applied to define the

blended rolled edge in the ρz coordinate system as

$$\rho_{blended}(\gamma) = \rho_{parabla}(\gamma)[1 - b(\gamma)] + \rho_{ellipse}(\gamma)b_{\gamma} \tag{3.24}$$

and

$$z_{blended}(\gamma) = z_{parabla}(\gamma)[1 - b(\gamma)] + z_{ellipse}(\gamma)b_{\gamma} \tag{3.25}$$

where

$$\rho_{parabola}(\gamma) = \gamma\frac{x_m}{\gamma_m}x_{p2} + p_j \tag{3.26}$$

and

$$z_{parabola}(\gamma) = \rho^2_{parabola}(\gamma)/4F. \tag{3.27}$$

Inserting Eq. (3.17), (3.18), (3.26), and (3.27) into Eq. (3.24) and (3.25) then

$$\rho_{blended}(\gamma) = (\gamma\frac{x_m}{\gamma_m}x_{p2})[1 - b(\gamma)] + [(a_e \sin\gamma)x_{p2} + b_e(1 - \cos\gamma)y_{p2}]b(\gamma) + p_j \tag{3.28}$$

and

$$z_{blended}(\gamma) = \left[\frac{(\gamma\frac{x_m}{\gamma_m}x_{p2})^2 + 2\rho_j\gamma\frac{x_m}{\gamma_m}x_{p2}}{4F}\right][1-b(\gamma)]+[a_e \sin\gamma x_{p3}+b_e(1-\cos\gamma)y_{p3}]b(\gamma)+z_j \tag{3.29}$$

for $\rho > \rho_j$. The portion of the reflector for $\rho < \rho_j$ is still defined as the simple parabolic expression from Eq. (3.23).

It is important to note that $b(\gamma)$ is a blending function that varies from zero to one from the junction to the furthest end of the rolled surface such that $b(0) = 0$ and $b(\gamma_m) = 1$. A common design is the cosine blend which is defined as

$$b(\gamma) = \frac{1}{2}\left[1 - \cos\left(\frac{\pi\gamma}{\gamma_m}\right)\right]. \tag{3.30}$$

Table 3.2: Common blending types, their equations, order, and constants for Eq. (3.31)

Blending Type	Blending Function	Order (n)	α
Linear	$b(\gamma) = \frac{\gamma}{\gamma_m}$	1	12
Square	$b(\gamma) = (\frac{\gamma}{\gamma_m})^2$	2	48
Cosine	$b(\gamma) = \frac{1}{2}(1 - \cos\frac{\pi\gamma}{\gamma_m})$	2	$12\pi^2$
Cosine Squared	$b(\gamma) = \frac{1}{4}(1 - \cos\frac{\pi\gamma}{\gamma_m})^2$	4	$90\pi^4$

More blending functions are displayed in Table 3.2. The blending function ensures the smooth transition for which we're aiming. The blending function is designed such that the derivative of it is zero at the junction. An nth order blending function, for which the first $n-1$ derivatives are zero at the junction and the nth derivative is nonzero ($b^n \neq 0$), provides a smoother transition the higher the nth order is. However, there is a point of diminishing returns where the higher orders no longer produce less diffracted fields and the higher order blending functions require more space to obtain a smooth junction. The discontinuity in the nth order derivative of the radius of curvature is

$$\epsilon_n = \frac{\alpha F k^{n+3}}{(x_m^n)} \left[\frac{a_e}{(x_m/\gamma_m)} + \frac{F b_e k^3}{(x_m/\gamma_m)^2} - \frac{1}{2} \right] \tag{3.31}$$

where

$$k = \sqrt{1 + (\rho_j/2F)^2}. \tag{3.32}$$

and α is a constant dependent on the blending function.

Table 3.2 includes the value of this constant for certain examples. The variables a_e, b_e, γ_m, and x_m can be tuned to set ϵ_n to zero. This will lead to a smooth surface to reduce the diffracted fields towards the quiet zone. Eq. (3.31) can be derived by comparing the nth derivative of the radius of curvature of the blending function to the nth derivative of the radius of curvature of the parabola at the junction of curvature ρ_j. This means that at the junction point (where $\gamma = 0$ and $\rho = \rho_j$) an nth order blending function adheres to the rule

that

$$\left(\frac{d^n R_c}{d\rho^n}\right)^{blend} = \left(\frac{d^n R_c}{d\rho^n}\right)^{parabola} + b^{(n)}(0)\epsilon_n. \tag{3.33}$$

The following sections walk through examples to illustrate the design process for both an elliptical and blended edge surface to operate in Ka-band (27 - 40 GHz).

3.2.1.1 Elliptical Edge Design Example

Consider a parabolic reflector with f_c = 35 cm and elliptic rolled surface terminations with $a_e = 8.6$ cm, $b_e = 3.75$ cm. The rolled edge is to be added at 30 cm (ρ_j^{top}) and at 15 cm (ρ_j^{bottom}). Let us call this surface S2.1. Recall that one of the design constraints is that the minimum radius of curvature (R_c^{min}) of the illuminated surface must not be smaller than $\lambda_{max}/4$ where λ_{max} corresponds to the wavelength at the lowest frequency of operation, which in this example is 27 GHz ($\lambda_{max} = 1.11$ cm.) In the case of an ellipse,

$$R_c^{min} = \frac{b_e^2}{a_e}. \tag{3.34}$$

Thus, $\frac{be^2}{ae}$ must not be less than 0.2775 cm. The selected values are acceptable as they yield a result of 1.758 cm. Figure 3.7 displays the surface.

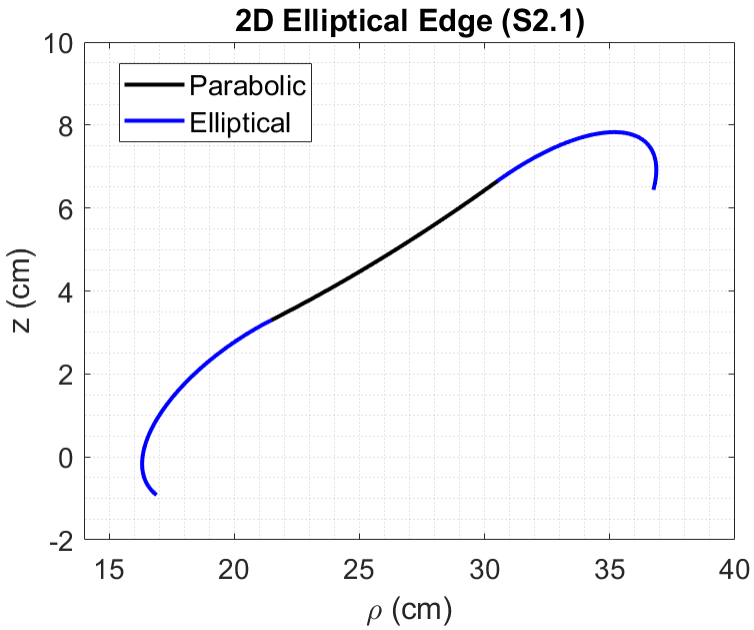

Figure 3.7: Two-dimensional parabolic reflector with elliptic rolled edges (S2.1).

Figure 3.8 presents the definition of the illuminated region of a surface when given vectors

$$\hat{\mathbf{n}} = \text{unit vector normal to the surface}$$

$$\hat{\mathbf{k}} = \text{direction of propagation of the incident electric field}$$

and

$$H^i = \text{incident magnetic field on the surface.}$$

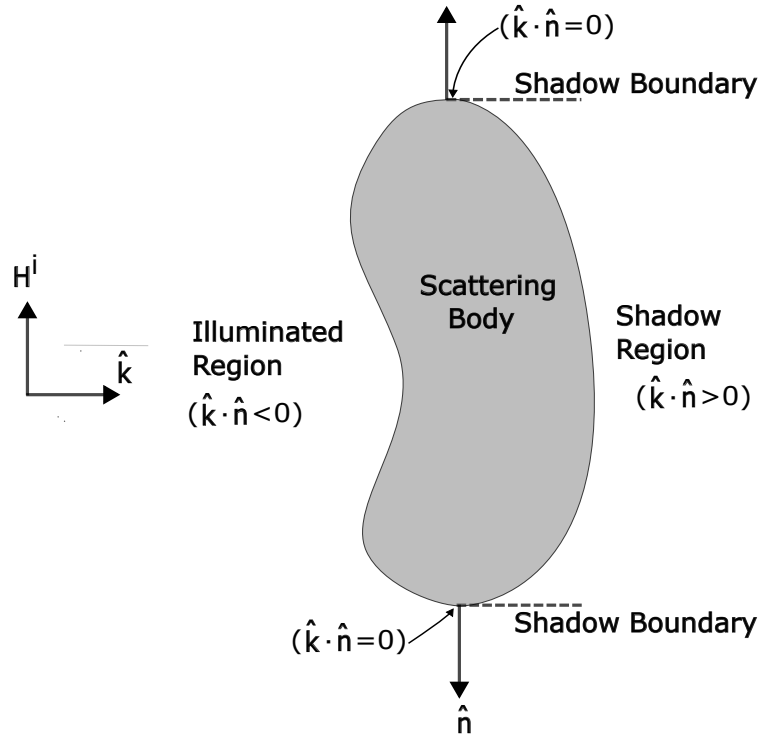

Figure 3.8: Illuminated region and shadow region of a scattering body.

The illuminated and shadow regions are determined by

$$\hat{\mathbf{k}}\cdot\hat{\mathbf{n}} = \begin{cases} < 0 & \text{in the illuminated region} \\ = 0 & \text{at the shadow boundary, and} \\ > 0 & \text{in the shadow region.} \end{cases} \tag{3.35}$$

When the dot product of $\hat{\mathbf{k}}$ and $\hat{\mathbf{n}}$ are less than zero, the surface is illuminated. The illuminated region up to and including the shadow boundary must meet the R_c^{min} requirements, which this example has done.

3.2.1.2 Blended Edge Design Example

Let us now design a cosine blended rolled edge for a 35 cm focal length reflector. Surface 2.2 also has an a_e of 8.6 and b_e of 3.75. The added variables to consider are x_m and γ_m. There are four main considerations in determining these values:

C.1) The first consideration is minimizing the nth order derivative of the radius of curvature, ϵ_n. This is done by yielding to Eq. (3.31).

C.2) Next, the maximum reflector dimensions must also be considered. In this case, the maximum allowable dimensions are 25 cm x 25 cm, which is, unfortunately, a fairly stringent size restriction for a Ka-band reflector. These size constraints are due to the limited size of the available 3D printers, which is how the 3D version of this reflector will be fabricated. The x_m value plays a large role in the size of the blended edges; a larger x_m results in a better ϵ_n value, but a larger sized reflector. To overcome this, experiments were performed to print the reflector into 4 pieces and interlock them together. This increases the maximum dimensions to 50 cm x 50 cm.

C.3) Another recommended rule is that the parabolic section of the reflector is at least 10λ. By dedicating this much space to the parabolic section of the reflector, the blended edge was originally allotted only the remaining space within the 25 cm x 25 cm restrictions, but this is also overcome with the solution of printing the reflector in quarters.

C.4) In general, γ_m is recommended to be between 105 and 180 degrees. However, a larger value typically results in a larger ϵ_n.

For the design process, γ_m was set to 105 degrees. A MATLAB code cycled through thousands of possible combinations of a_e, b_e and x_m while filtering results that met the size and ϵ_n constraints. The parabolic portion of the reflector was sized at slightly greater than 10λ to allow more room for the blended edges because otherwise, an acceptable ϵ_n value was difficult to achieve. At 27 GHz, the height of the parabolic portion is 13.5λ. Table 3.3

displays the surface parameters. The final 2D reflector size was 18 cm x 44 cm and the ϵ_n is 0.6654 at both the top and bottom junctions.

Table 3.3: 2D surface characteristics

	Surface 2.1	Surface 2.2
Blending:	None	Cosine
f_c	35 cm	35 cm
a_e	8.6 cm	8.6 cm
b_e	3.75 cm	3.75 cm
x_m	-	38 cm
γ_m	-	105°
y_{bot}	15 cm	15 cm
y_{avg}	22.5 cm	22.5 cm
y_{top}	30 cm	30 cm
ψ_f	35.64°	35.64°

The minimum radius of curvature is trivial to determine in the case of an elliptical shape, as seen in the previous example (Eq. (3.34)). For a curve defined in the ρz plane the radius of curvature can be found as,

$$R_c(\gamma) = \frac{R_u}{R_l} \tag{3.36}$$

where

$$R_u(\gamma) = \sqrt[3]{(\rho')^2 + (z')^2} \tag{3.37}$$

and

$$R_l(\gamma) = |\rho' z'' - \rho'' z'|. \tag{3.38}$$

Thus, by taking the derivative and second derivative of equations 3.28 and 3.29, which were the lengthy equations describing the curvature of $z_{blended}$ and $\rho_{blended}$, one can find the radius of curvature of the blended edge. Then, depending on $\hat{\mathbf{k}}$ (the direction of propagation of the incident electric field) and the shape of the reflector surface, it can be determined where the illuminated region is truncated by the shadow boundary. This is essential to determining that the minimum radius of curvature of the blended edge reflector's illuminated region is not less than $\lambda_{max}/4$. It is too lengthy to show here, but this example does meet this constraint as 0.2901 is more than 0.2775 cm. Figure 3.9 shows Surface 2.2 compared to Surface 2.1.

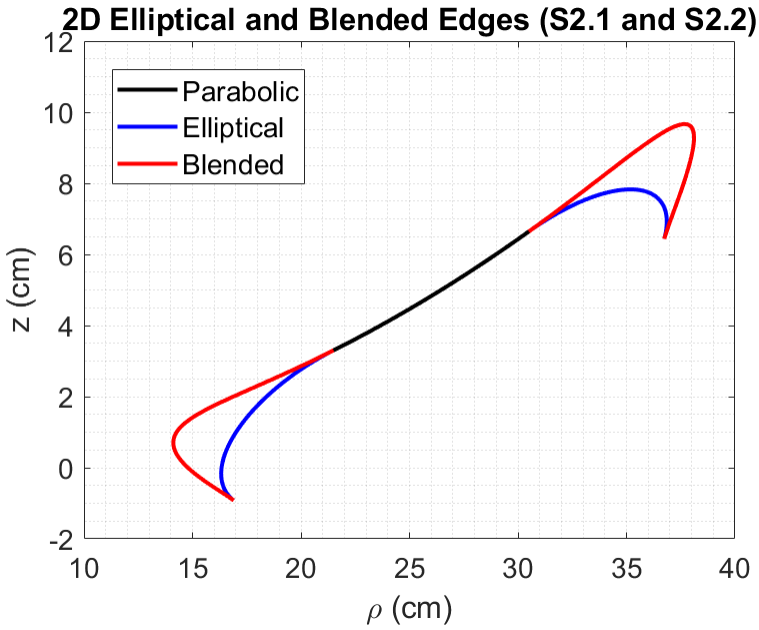

Figure 3.9: Two-dimensional parabolic reflector with elliptic and blended rolled edges (S2.1) and (S2.2).

3.2.2 3D Design Method

The discussion thus far has established the method to design an elliptical and blended edge in the 2D space and now this foundation will be expounded upon for the 3D design. The 3D design is, of course, the most practical for realizing the reflector in the real world. Again, the 3D mathematical design is also based on Gupta's [25] work for the framework of the next subsection.

The paraboloid in the xyz coordinate system is defined as

$$z = \frac{x^2 + y^2}{4F}. \tag{3.39}$$

The rim of the reflector is called the junction contour around the perimeter. Figure 3.10(a) shows the 2D parabola. Figure 3.10(b) depicts the parent paraboloid centered in the xyz coordinate system, and the section of the parent utilized for the 3D offset reflector is centered at a point $(x_{avg}, y_{avg}, z_{avg})$. Note that

$$z_{avg} = (x_{avg}^2 + y_{avg}^2)/4F. \tag{3.40}$$

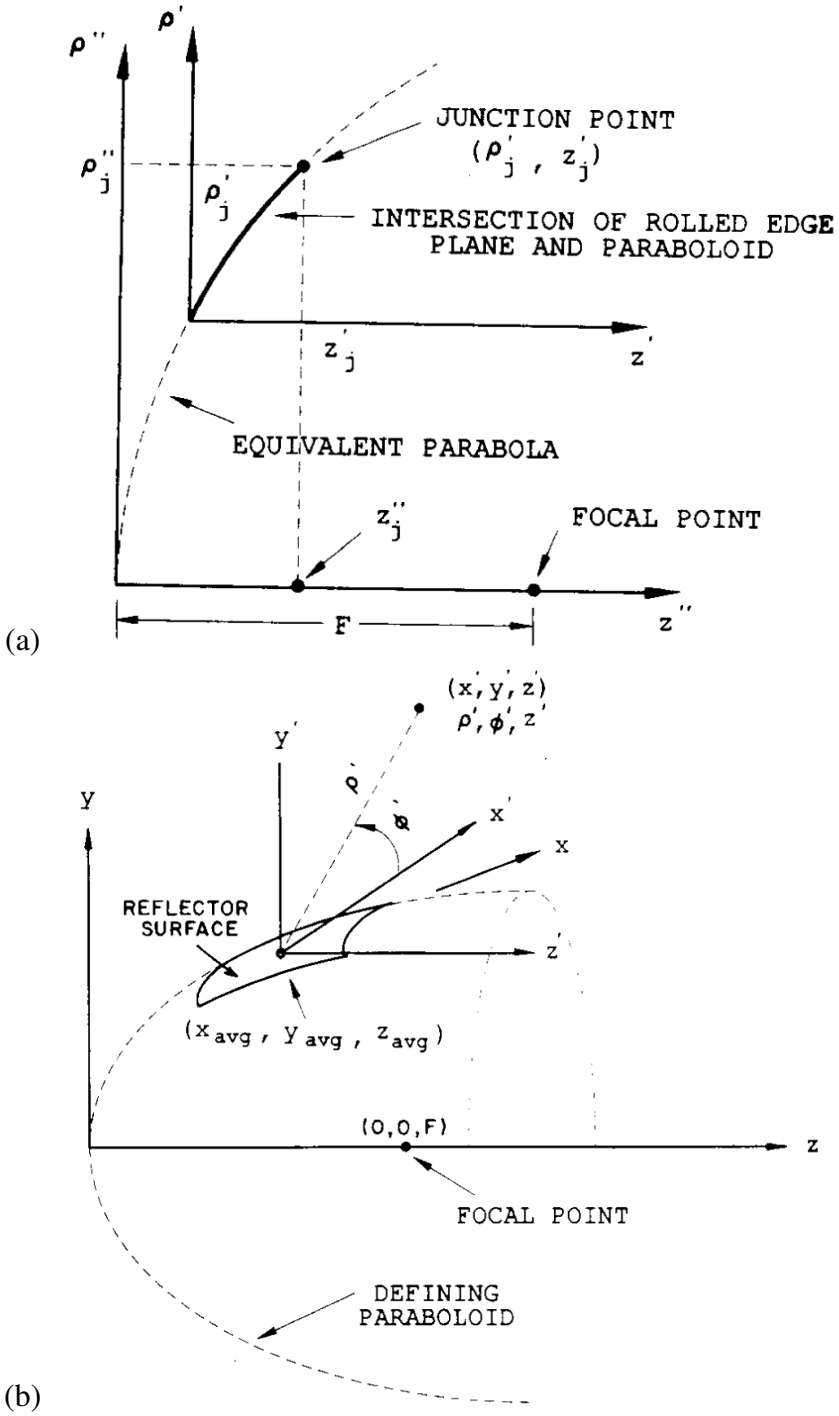

Figure 3.10: Coordinate system for 3D rolled edge design [25].

Table 3.4: Coordinate system translations

Coordinate system translations	
Translation from xyz to $x'y'z'$	Translation from $x'y'z'$ to $\rho'\phi'z'$
$x = x' + x_{avg}$	$x' = \rho' \cos\phi'$
$y = y' + y_{avg}$	$y' = \rho' \sin\phi'$
$z = z' + z_{avg}$	$z' = z'$

A new coordinate system $x'y'z'$ has an origin centered at the offset reflector. A cylindrical coordinate system sharing an origin with $x'y'z'$ is also defined and can be viewed in Figure 3.10(a). Table 3.4 gives the translation equations between the coordinate systems.

As seen in Figure 3.10(a), p'_j is a point on the junction contour of the reflector in the cylindrical coordinate system. This point p'_j is a single value for each ϕ' angle. To collect a series of p'_j values to build the 3D rim, a value must be defined for each ϕ' value. For each instance when ϕ' is fixed, looking at a certain point on the rim, the rolled edge is added in the $\rho'z'$ plane. Thus, a similar approach is taken as seen in the 2D design strategy. For each angle ϕ' a smooth rolled edge is added in the $\rho'z'$ plane. In this way, the reflector builds up a surface of unique rolled edges that vary with angle. First, it is important to understand that the parabolic section of the reflector is given by,

$$\rho'^2 + 2\rho'(x_{avg}\cos\phi' + y_{avg}\sin\phi') = 4Fz' \quad \text{for} \quad \begin{cases} 0 \leq \rho' \leq p'_j \\ 0 \leq \phi' \leq 2\pi \end{cases} \tag{3.41}$$

If the rolled edge is added at a point $\phi' = \phi'_j$, then Eq. (3.41) becomes

$$\rho'^2 + 2\rho'(x_{avg}\cos\phi' + y_{avg}\sin\phi') = 4Fz'. \tag{3.42}$$

By extension, the junction height, as shown in Figure 3.10, is

$$\rho_j'' = \rho_j'(\phi_j') + x_{avg}\cos\phi_j{}' + y_{avg}\sin\phi_j'. \tag{3.43}$$

The junction height ρ_j'' may vary with ϕ_j', so the rolled edge parameters will vary with ϕ_j'. Building from Section 3.2.1, the rolled edge in the $\rho' z'$ coordinate system is defined as

$$\rho'(\gamma) = \left[\gamma\frac{x_m(\phi_j')}{\gamma_m(\phi_j')}x_{p2}\right][1-b(\gamma)] + [(a_e(\phi_j')\sin\gamma)x_{p2} + b_e(\phi_j')(1-\cos\gamma)y_{p2}]b(\gamma) + \rho_j'(\phi_j') \tag{3.44}$$

and

$$\begin{aligned} z'(\gamma) = &\left[\left(\gamma\frac{x_m(\phi_j')}{\gamma_m(\phi_j')}x_{p2} + \rho_j''\right)^2/4F\right][1-b(\gamma)][(a_e(\phi_j')\sin\gamma)x_{p3} \\ &+b_e(\phi_j')(1-\cos\gamma)y_{p3} + z_j'']b(\gamma) - (x_{avg}\cos\phi_j' + y_{avg}\sin\phi_j')^2/4F \end{aligned} \tag{3.45}$$

where

$$z_j'' = (\rho_j'')^2/4F \tag{3.46}$$

$$x_{p2} = 2F/(\rho_j''^2 + 4F^2)^{1/2} \tag{3.47}$$

$$y_{p2} = \rho_j''/(\rho_j''^2 + 4F^2)^{1/2} \tag{3.48}$$

$$x_{p3} = \rho_j''/(\rho_j''^2 + 4F^2)^{1/2} \tag{3.49}$$

and

$$y_{p3} = -2F/(\rho_j''^2 + 4F^2)^{1/2}. \tag{3.50}$$

Therefore, the entire surface is defined in the $\rho'\phi' z'$ coordinate system. Similarly seen in the previous section, for a given ϕ', Eq. (3.41) defines the surface for $\rho' < \rho_j'(\phi')$ while Eq. (3.44) and (3.45) define the surface for $\rho' > \rho_j'(\phi')$ as a function of parametric angle γ.

As mentioned earlier in this subsection, the reflector rim can be any shape. According to Pistorius [46], the optimal reflector shape is a convex rectangle. Figure 3.11 depicts an example of a concave-shaped rim. The reflector would be parabolic within the rim and the blended edges would begin after the rim.

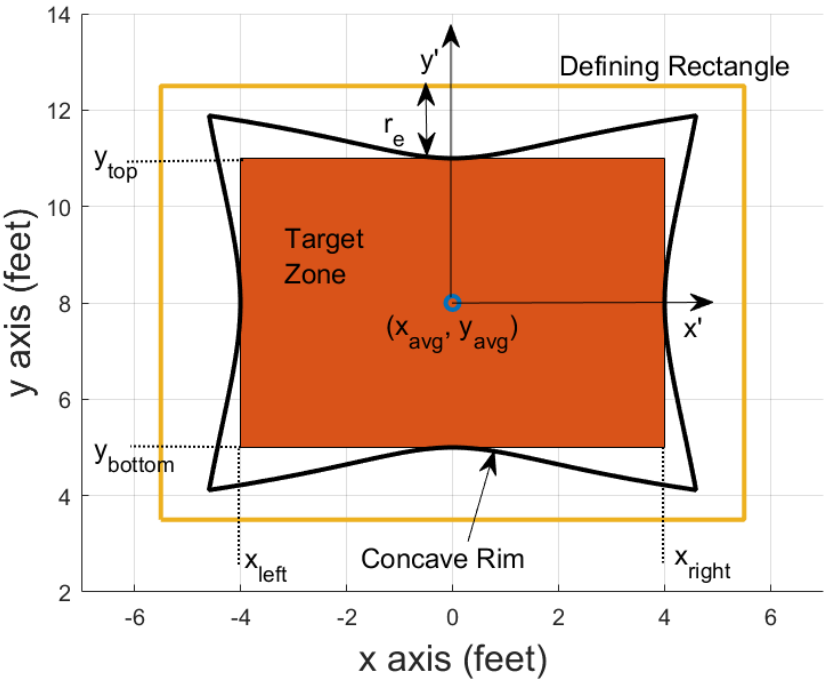

Figure 3.11: Concave frame, target zone, and defining rectangle described as well as defining characteristics.

The target zone is defined as extending from x_{left} to x_{right} and from y_{bottom} to y_{top} in the $x-$ and $y-$ directions, respectively. There is a defining rectangle that is a distance r_e away from all borders of the target zone. This can be seen in Figure 3.11. The value r_e controls the concavity. A positive r_e yields a concave rim, an r_e of zero yields a rectangular rim, and a negative r_e value, a convex rim. The concave edge is defined as

$$x_j = \begin{cases} x_{right} + r_e(1 - \cos\phi') & 0 \le \phi' \le \phi_1 \\ x_{avg} + (y_{top} + r_e - y_{avg})\cot\phi' - r_e\cos\phi' & \phi_1 \le \phi' \le \phi_2 \\ x_{left} - r_e(1 + \cos\phi') & \phi_2 \le \phi' \le \phi_3 \\ x_{avg} + (y_{bottom} - r_e - y_{avg})\cot\phi' - r_e\cos\phi' & \phi_3 \le \phi' \le \phi_4 \\ x_{right} + r_e(1 - \cos\phi') & \phi_4 \le \phi' \le 360^\circ \end{cases} \tag{3.51}$$

$$y_j = \begin{cases} y_{avg} + (x_{right} + r_e - x_{avg})\tan\phi' - r_e\sin\phi' & 0 \le \phi' \le \phi_1 \\ y_{top} + r_e(1 - \cos\phi') & \phi_1 \le \phi' \le \phi_2 \\ y_{avg} + (x_{left} - r_e - x_{avg})\tan\phi' - r_e\sin\phi' & \phi_2 \le \phi' \le \phi_3 \\ y_{bottom} - r_e(1 - \cos\phi') & \phi_3 \le \phi' \le \phi_4 \\ y_{avg} + (x_{right} + r_e - x_{avg})\tan\phi' - r_e\sin\phi' & \phi_4 \le \phi' \le 360^\circ \end{cases} \tag{3.52}$$

$$z_j = (x_j^2 + y_j^2)/4F \tag{3.53}$$

where

$$x_{avg} = (x_{left} + x_{right})/2 \tag{3.54}$$

$$y_{avg} = (y_{top} + y_{bottom})/2 \tag{3.55}$$

$$\phi_1 = \tan^{-1}\left(\frac{y_{top} + r_e - y_{avg}}{x_{right} + r_e - x_{avg}}\right) \tag{3.56}$$

$$\phi_2 = \tan^{-1}\left(\frac{y_{top} + r_e - y_{avg}}{x_{left} - r_e - x_{avg}}\right) \tag{3.57}$$

$$\phi_3 = \tan^{-1}\left(\frac{y_{bottom} + r_e - y_{avg}}{x_{left} - r_e - x_{avg}}\right) \tag{3.58}$$

and

$$\phi_4 = \tan^{-1}\left(\frac{y_{bottom} - r_e - y_{avg}}{x_{left} - r_e - x_{avg}}\right). \tag{3.59}$$

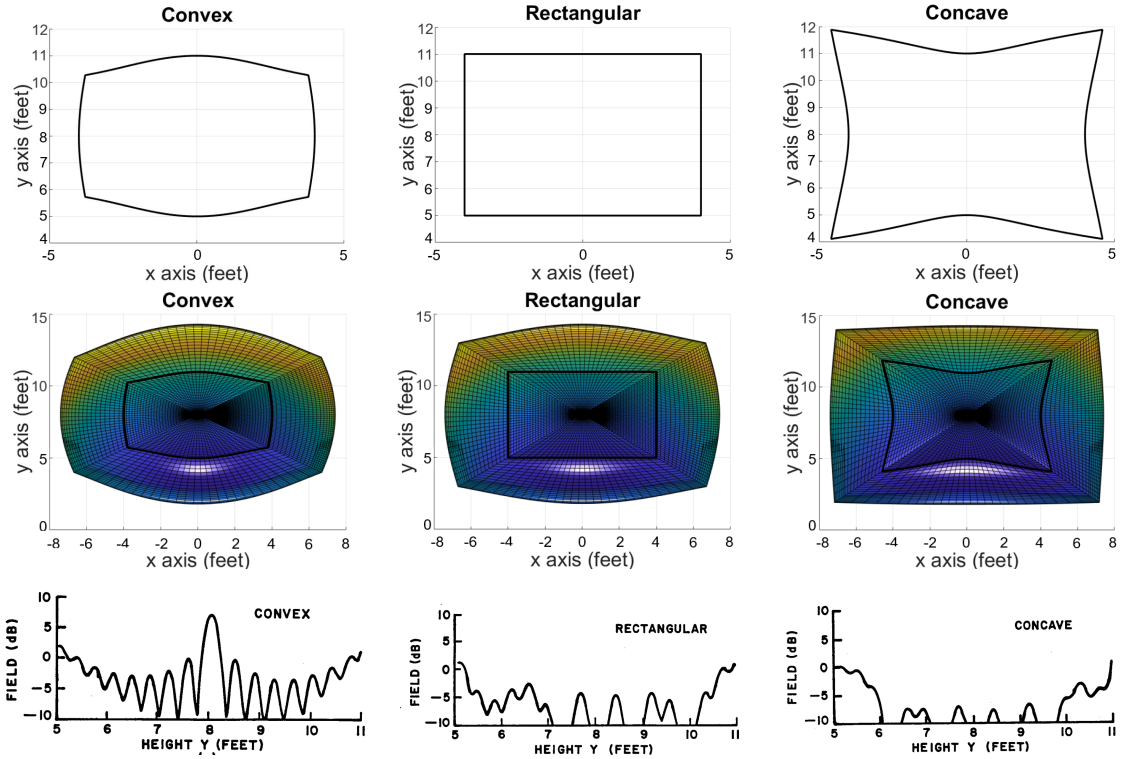

Figure 3.12: The first row depicts convex, rectangular, and concave rims (identical except for the r_e value). The second row shows the entire blended edge surface (again, identical parameters except for r_e). The third row includes the results from [46] displaying the magnitude of the diffracted fields from each reflector (10 GHz).

Figure 3.12 presents a convex, rectangular, and concave rim, the complete reflectors built around those rims, and their calculated magnitude of diffracted fields as found by [46]. Figure 3.12 demonstrates that a convex frame will result in a higher magnitude of edge-diffracted fields when the goal is to minimize edge diffractions. Thus, a concave-shaped rim is ideal for the best quiet zone [46].

3.2.2.1 Elliptical Edge Design Example

A three-dimensional reflector referred to as surface S3.1 with $f_c = 35$ cm and concave edge contours will now be analyzed. This corresponds to the two-dimensional surface S2.1 discussed earlier in Section 3.2.1.1 in that surface S2.1 is the yz-plane cut of S3.1. The reflector parameters include an a_e of 8.6 cm and b_e of 3.75 cm.

The target zone is considered to be 12 cm wide and 15 cm tall, with the center of the target zone 22.5 cm above the axis of symmetry of the paraboloid as shown in Figure 3.11. The surface is pictured in Figure 3.13 and will be compared to a blended edge counterpart in the following section.

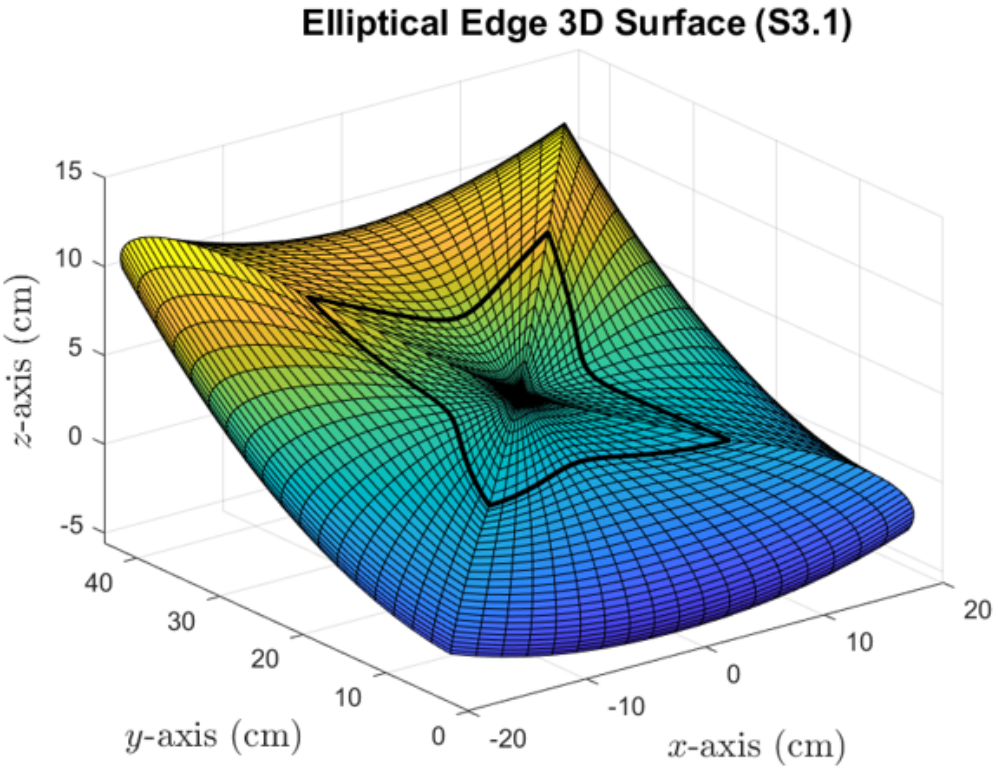

Figure 3.13: Three-dimensional parabolic reflector with elliptical edges (S3.1)

3.2.2.2 Blended Edge Design Example

Consider now the case of a parabolic reflector with a focal length of 35 cm and a cosine blended edge with parameters $a_e = 8.6$, $b_e = 3.75$, $x_m = 38$, and $\gamma_m = 105$ degrees. This surface S3.2 is the final design that is ultimately fabricated and implemented in the CATR system. Chapter 5 presents the measured results of this enacted design. Again, for the design process, a MATLAB code cycled through thousands of possible combinations of a_e, b_e and x_m (γ_m was set to 105 degrees) while filtering through and saving results that met the size and ϵ_n constraints.

The average ϵ_n value across all angles was 0.653, which is a relatively low radius of curvature discontinuity. This means the blended edge with these parameters is a promising design for the goal of minimizing edge diffractions in the CATR quiet zone. The final size of the reflector is 38.12 cm x 39.91 cm x 18.22 cm, which does fit in the size constraints of the Bambu printer being used for fabrication when it is sliced into four pieces. The MATLAB surface plot shown of this reflector in Figures 3.14 and 3.15 can be increased in resolution and exported as an .stl file with the use of a MATLAB function. This is then imported into Solidworks and modified to add the backing and to turn it into a printable solid. One quarter is printed at a time, as well as a final fixture to hold them into place. An epoxy glue is then used to secure the pieces.

The next section pivots from the discussion of the geometric design to the study of the allowable surface roughness of reflectors for Ka-band and higher. This is another important element to consider in the implementation of a mmWave reflector. Table 3.5 displays the parameters for S3.1 and S3.2.

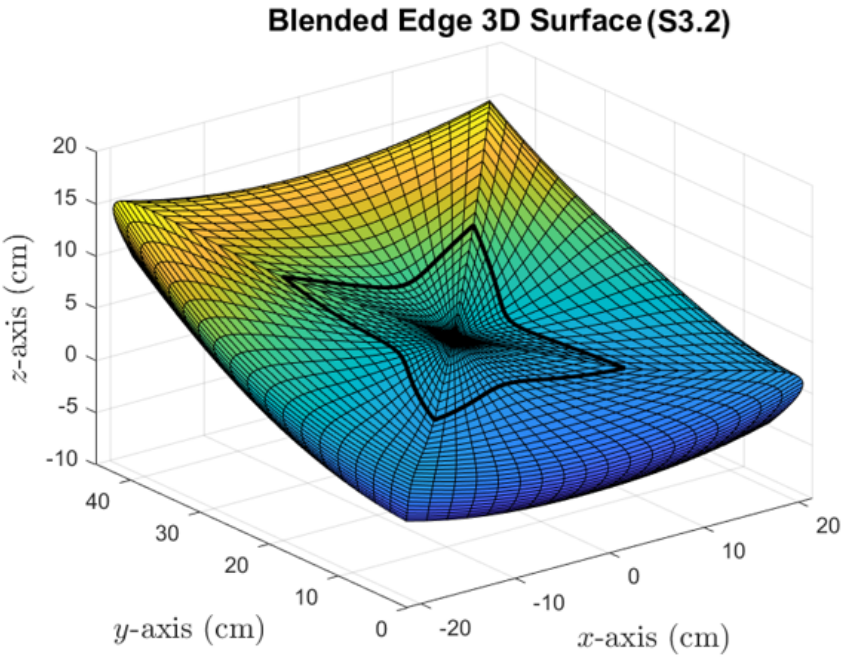

Figure 3.14: Three-dimensional parabolic reflector with blended rolled edges (S3.2).

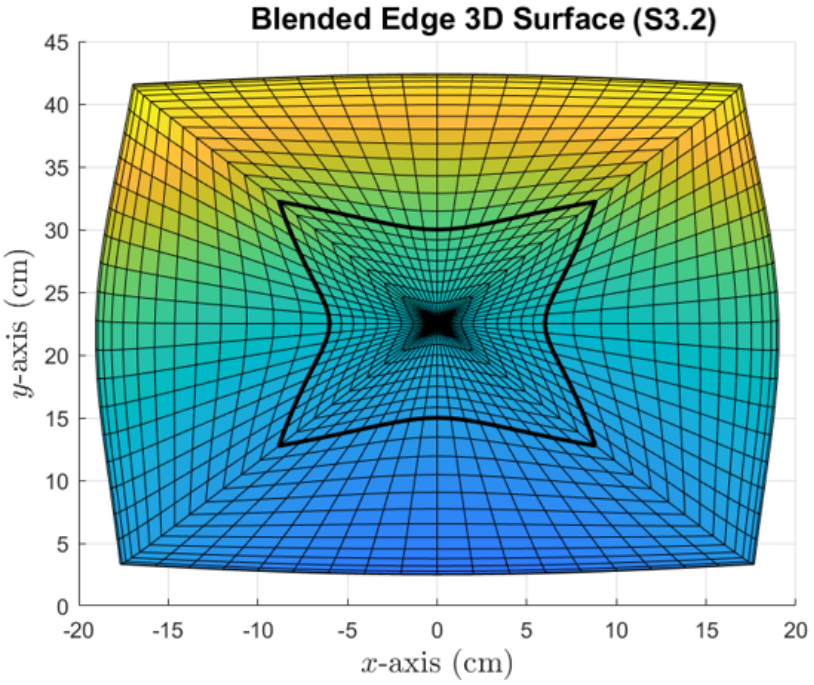

Figure 3.15: Three-dimensional parabolic reflector with blended rolled edges front view.

Table 3.5: 3D surface characteristics

	Surface 3.1	Surface 3.2
Blending:	None	Cosine
f_c	35 cm	35 cm
a_e	8.6 cm	8.6 cm
b_e	3.75 cm	3.75 cm
x_m	-	38 cm
γ_m	-	105°
r_e	8.6 cm	8.6 cm
y_{bot}	15 cm	15 cm
y_{avg}	22.5 cm	22.5 cm
y_{top}	30 cm	30 cm
x_{left}	-6 cm	-6 cm
x_{right}	6 cm	6 cm
ψ_f	35.64°	35.64°

3.3 Reflector Roughness

Previous studies have produced reflector designs for compact ranges intended to operate well below the mmWave spectrum, however, very few works have studied the design and implementation of reflectors for the mmWave spectrum. The main projected obstacle is the surface roughness as studies have shown that surface roughness on the order of a few micrometers can lead to significant losses in reflectivity, reduce the gain of the reflector, increase sidelobe level, and increases the noise in the system [52]–[56]. Two main parame-

ters are used to describe the roughness of a substrate: average roughness, Ra, and root mean square roughness, Rq. The average roughness, Ra, is the arithmetic average of the absolute values of the profile heights over the sample. The RMS roughness, Rq, is the root mean square average of the profile heights over the sample. For this project, two instruments were used to measure the surface roughness of various samples.

First, simulations were completed in TICRA GRASP to observe and quantify the effect of a reflector's surface roughness on the purity of the quiet zone. This will provide much-needed direction when creating the surface roughness requirements for the fabrication of the reflector in both 3D printing and CNC milling [57]. The simulation set-up included an identical reflector scaled for different frequencies from W-band to sub-terahertz. Various average roughness values are simulated, ranging from 0 (ideal) to 25 μm. Another important variable that was evaluated was the spacing between the roughness peaks ns. This variable describes the rate of change of the surface roughness. Different materials can possess the same average roughness, but the surfaces look drastically different because the roughness spacing differs.

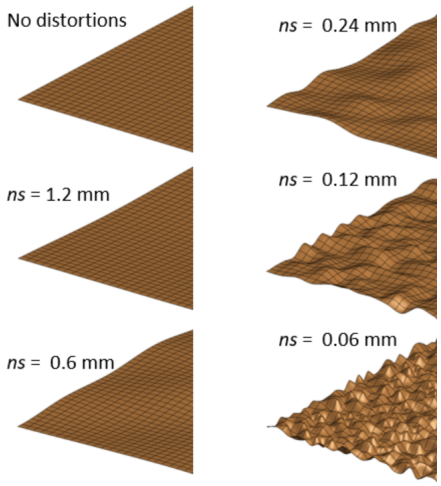

Figure 3.16: Various ns values are illustrated for a common RMS roughness value. The distance between the black lines on the surface is 0.06 mm [58].

This can be seen in Figure 3.16. One case demonstrates no distortions. Five cases of surface smoothness corresponding to ns = 1.2, 0.6, 0.24, 0.12, and 0.06 mm for the same value of ϵ_{rms} are illustrated in Figure 3.16. The example visuals in Figure 3.16 all share the same ϵ_{rms} value, but the frequency of the peaks and valleys vary. A higher ns value denotes that the surface roughness varies at a slower rate while a lower ns value means that it is a more rapidly varying surface.

The TICRA simulation included reflectors designed for 100 GHz, 200 GHz, 300 GHz, 400 GHz, and 500 GHz. The average roughness varied from 0 to 25 μm and the spacing, ns, was set to 250 μm, 500 μm, and 1000 μm. Figure 3.17 displays the resulting phase variation in the quiet zone for each combination.

Based on the results, as expected, the phase variation worsens when the average roughness increases. The increased roughness results in the incident propagating wave bouncing in a slightly offset direction than intended. As this happens across the entire surface of the reflector, the aggregate of the collimated wave has many small errors introduced that cause increased phase distortion in total. This is exacerbated by higher average roughness values. According to the plots, this problem becomes worse at a faster rate for higher frequencies. 100 GHz and 200 GHz appear to be relatively unaffected by the surface roughness reaching 25 μm, however, 500 GHz in all scenarios worsens significantly after Ra = 10 μm.

Another conclusion from the simulations is that the larger spacing between roughness peaks also increases phase variation in the quiet zone. Thus, for fabrication purposes, it is desired to minimize average roughness and also the spacing between peaks. The pertinent frequency band for this project is Ka-band, so the simulation proves surface roughness is not an extreme issue for this spectrum. These simulations also prove that the reflector should be able to operate well into the sub-terahertz band since a smooth surface is prioritized in fabrication.

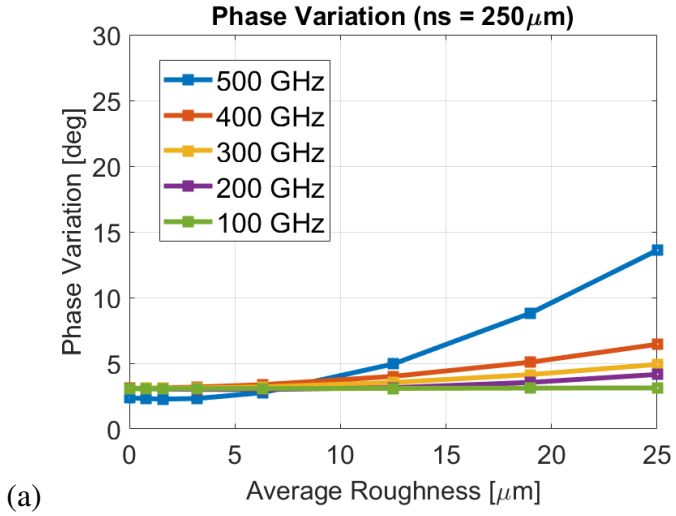

(a)

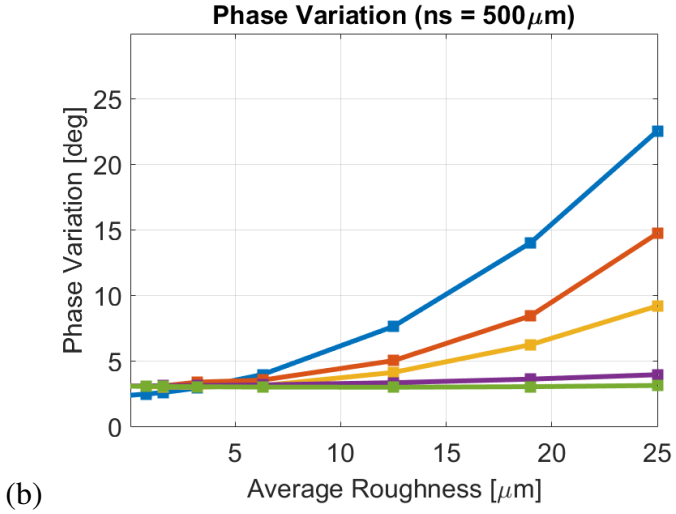

(b)

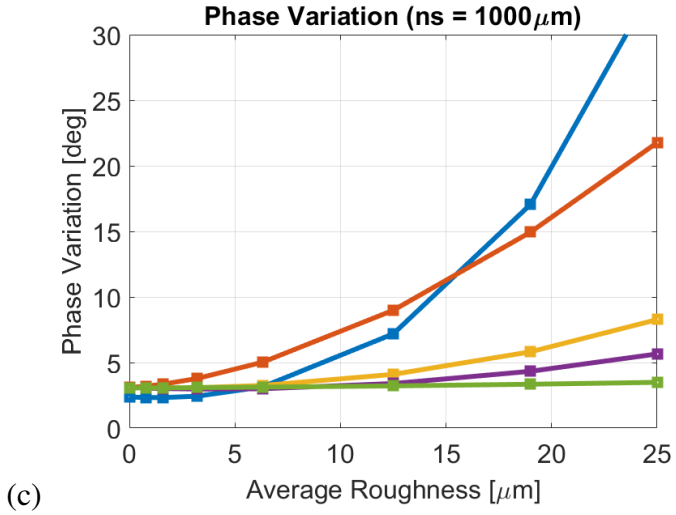

(c)

Figure 3.17: Quiet zone phase variation for reflectors across surface roughness for various frequencies 100 through 500 GHz and with ns values of 250 μm, 500 μm, and 1000 μm.

With these guiding parameters, many fabrication processes were analyzed for their resulting surface roughness. First, a sample kit with metal samples that were created with various average roughness values and different machining methods (turning, grinding, etc) was measured with both an Atomic Force Microscope and a high-accuracy profilometer, both capable of measuring surface resolution on the order of nanometers ($<$5 nm and 0.01 nm, respectively.)

Multiple 3D printed samples were created to compare to the machined samples. Samples of PLA, ABS, and resin were printed from Bambu and Form 3 printers. While the 3D printed sample may be acceptable on its own, it must also have an acceptable roughness when applying the metal (reflective) coat. Silver paint, copper plating, and copper tape are explored as potential options, and their roughness is measured. Figure 3.18 showcases the samples created from the different materials. The samples were sanded with a grit of up to 2000 before any treatments were applied. ABS can also be 'sanded' with acetone fumes to smooth the surface; this is one of the samples included to be measured.

The measurements in Figure 3.18 showcase that even the untreated samples had fairly acceptable levels of surface roughness, especially the resin printed sample. In all cases, unsurprisingly, sanding lowered the roughness. The images in Figure 3.19 as taken by the AFM machine of the resin sample before and after being sanded portray the significant difference sanding makes. The silver paint had the highest surface roughness across the board, but this could also be due to the application process of the paint on these specific samples. At the time no aerosol paint gun was available, so the samples were hand-painted with a brush, likely worsening the roughness. The acetone fumes as an alternative 'sanding' method for the ABS sample improved from the original print but did not perform better than traditional sanding. The copper-plated samples fared very well, boasting low surface roughness in all three cases. The copper tape was also shown to be a viable option with high smoothness.

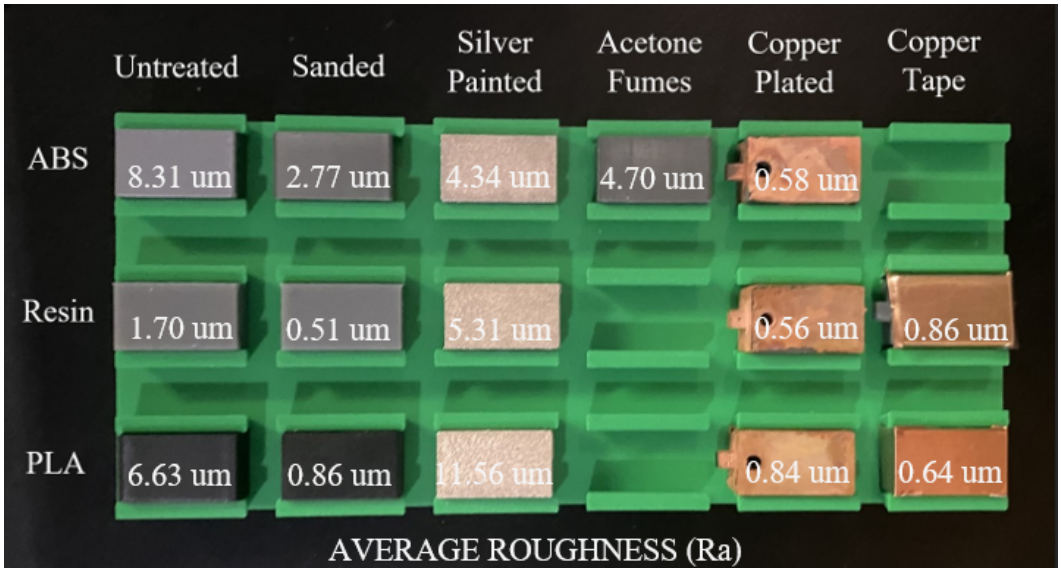

Figure 3.18: Various 3D printed samples, treated and untreated, and their average roughness as measured by the profilometer.

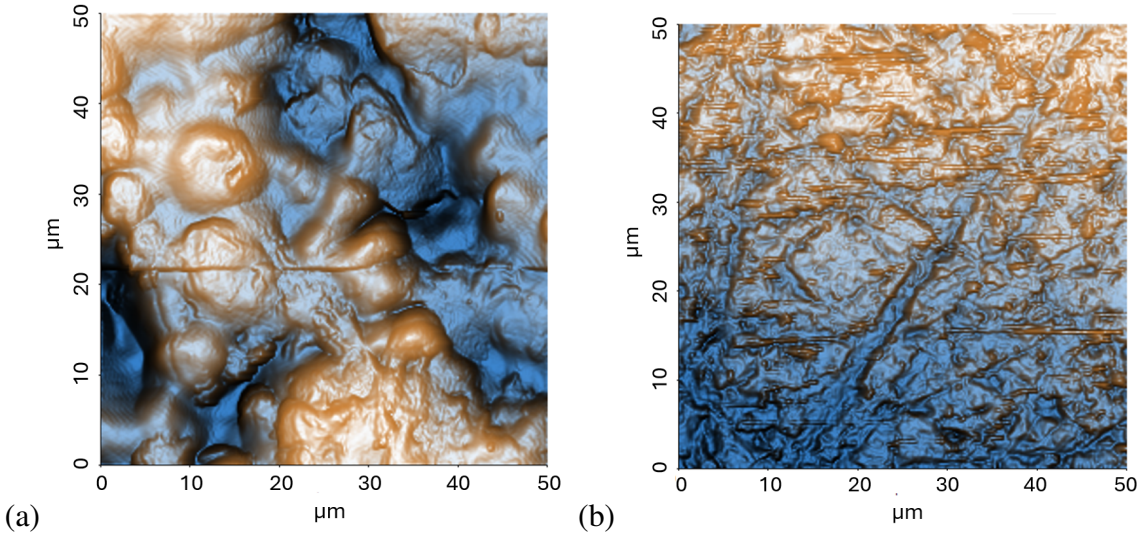

Figure 3.19: Microscopic image from AFM of Form 3 resin printed surface (a) before and (b) after sanding by hand with a grit of up to 2000.

Although the resin samples boasted the best and smoothest surfaces, due to the limited size of the resin printers available, ultimately PLA was selected to use for the reflector print. Because PLA is the material chosen for fabrication, Figure 3.20 displays the surface

roughness measurements of the PLA samples in more detail. It can be seen that the untreated sample retains the lines of the printer extruder building it row by row. The sanded sample eradicates this pattern, but small pockets remain. The silver paint does not have an even coat, with small but noticeable splotches. Again, better application of the paint could be a solution. The copper plating is relatively even across the sample and the copper tape is even more so, except for a bump that is probably an imperfection in the application.

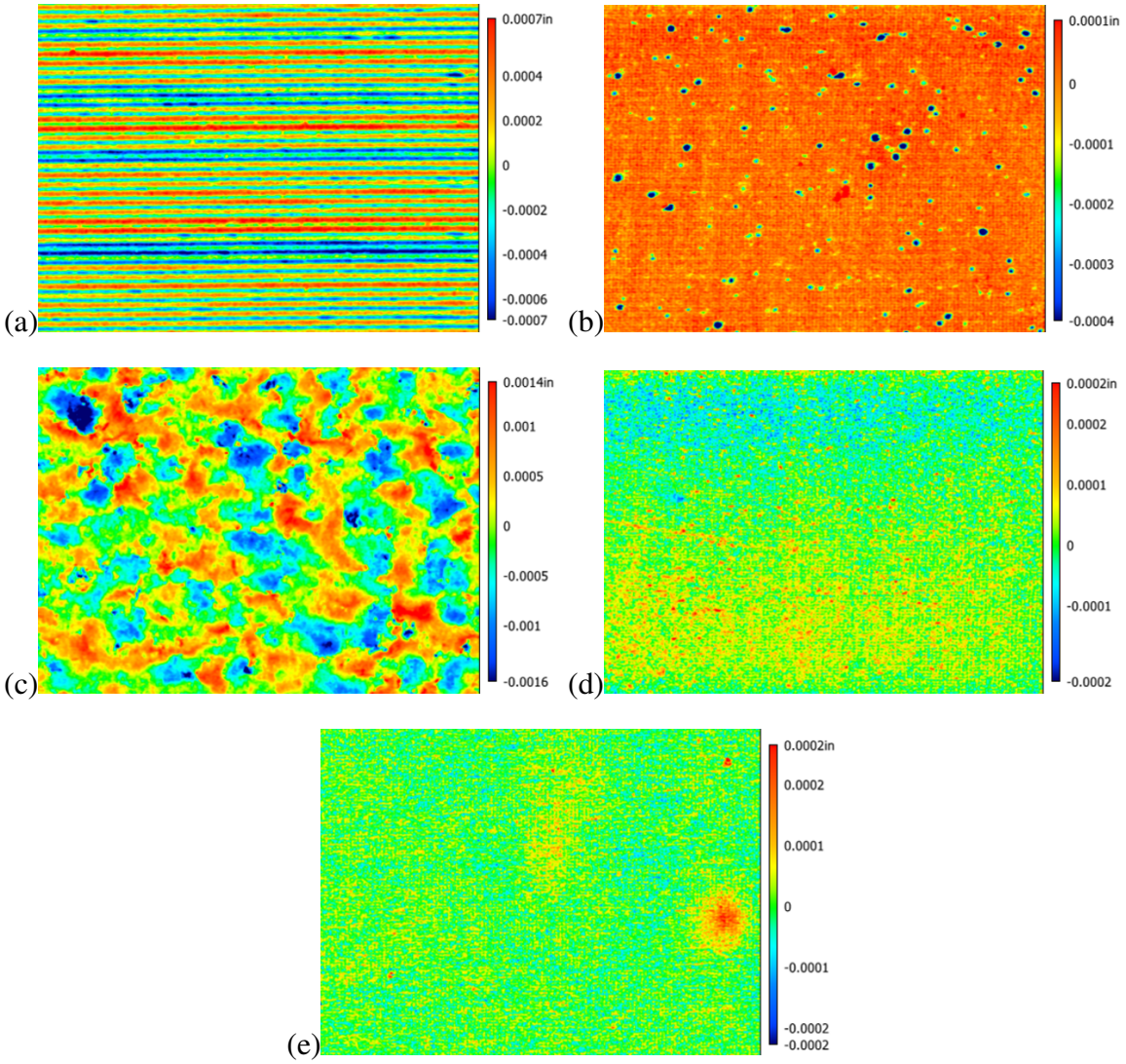

Figure 3.20: Microscopic height images (0.1 in x 0.15 in) from profilometer of PLA printed surfaces (a) untouched (b) sanded by hand with a grit of up to 2000 (c) sanded and coated with silver paint (d) sanded and copper plated and (e) sanded and covered with copper tape.

3.3.1 Ruze Equation

The effects the surface roughness has on the gain of a system can be quantified. Ruze [59] pioneered much of this work as early as the 1950's recognizing that the surface tolerance of an antenna has a crucial influence on its performance, but it is today more than ever that the surface tolerance of our systems needs to be understood as boundaries are being pushed into higher frequency spectrums with increased sensitivity to roughness [59]–[63]. This analysis is an important piece in identifying the upper limit in which our system can perform. This section will explain how the gain loss of the CATR due to the reflector roughness can be estimated and will provide mathematical examples confirmed with simulations. The main parameters, as discussed in the previous section, are the peak and average roughness values, which will now be denoted as ϵ_p and ϵ_{rms}, and the spacing between the roughness peaks ns. For our purposes, and aligning with how TICRA GRASP computes their simulations, the RMS value can be derived from the peak roughness value as

$$\epsilon_{rms} = 0.47\epsilon_p. \tag{3.60}$$

This is found via a cubic interpolation and is a satisfactory estimate for our purposes. The ns value describes the rate of change of the surface roughness. In his examinations of reflector antennas, Ruze [62] based his equations on a concept of a correlation region with diameter "2c" outside of which the correlation is zero. In summary for this analysis to be accurate, if an autocorrelation function of the surface were to be obtained, the total width of that autocorrelation function must be a certain amount before tapering to zero. The general rule of thumb is that these equations apply when the autocorrelation function of the surface roughness of an area that, when plotted, tapers to zero after a length of at least 2λ. See [58] and [62] for a more in-depth explanation of this requirement. Ruze derives a

formula to estimate the peak gain reduction for a planar wave incident on a surface with a random distortion of $2c \geq \lambda$. The derivation is beyond the scope of this work, however, the resulting formula is

$$P = e^{-(\frac{4\pi\epsilon_{rms}}{\lambda})^2}, \text{ for } 2c \geq \lambda \tag{3.61}$$

where δ_{rms} is the root mean square of the aperture error described as

$$\delta_{rms} = (1 + \cos\psi_f)\epsilon_{rms}. \tag{3.62}$$

Figure 3.21 displays the aperture distortion along the reflector's aperture plane. For a given ϵ_{rms} of a reflector and a feed pointed to it at an angle of ψ_f, the aperture distortion RMS value δ_{rms} can be calculated. All of these variables play a role in the loss of gain in the system.

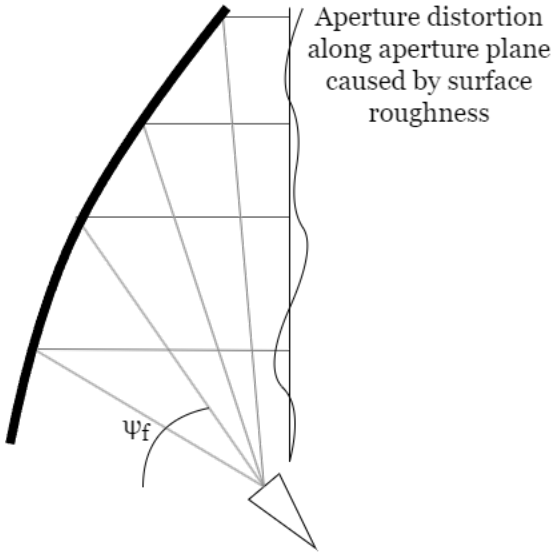

Figure 3.21: Distortion in the aperture plane induced by surface distortion.

Let's explore the loss in gain for a reflector of various surface roughnesses. Eq. (3.61), which describes the peak gain reduction for a planar wave incident on a reflector, is employed and compared to simulation results.

Table 3.6: Ruze gain loss calculations

Gain loss calculations for 500 GHz and ns of 1.2 mm				
ϵ_p (μm/mm)	ϵ_{rms} (μm/mm)	δ_{rms} (λ)	Calculated Loss (dB)	Simulated Loss (dB)
6.8 / 0.0068	3.2 / 0.0032	0.009	0.020	0
13.4 / 0.013	6.3 / 0.0063	0.017	0.076	0
26.6 / 0.027	12.5 / 0.0125	0.034	0.299	0.329
40 / 0.040	19 / 0.019	0.052	0.673	0.693
60 / 0.060	28.2 / 0.028	0.077	1.515	1.154
80 / 0.080	38 / 0.038	0.116	2.693	1.978
100 / 0.100	47 / 0.047	0.129	3.409	2.762

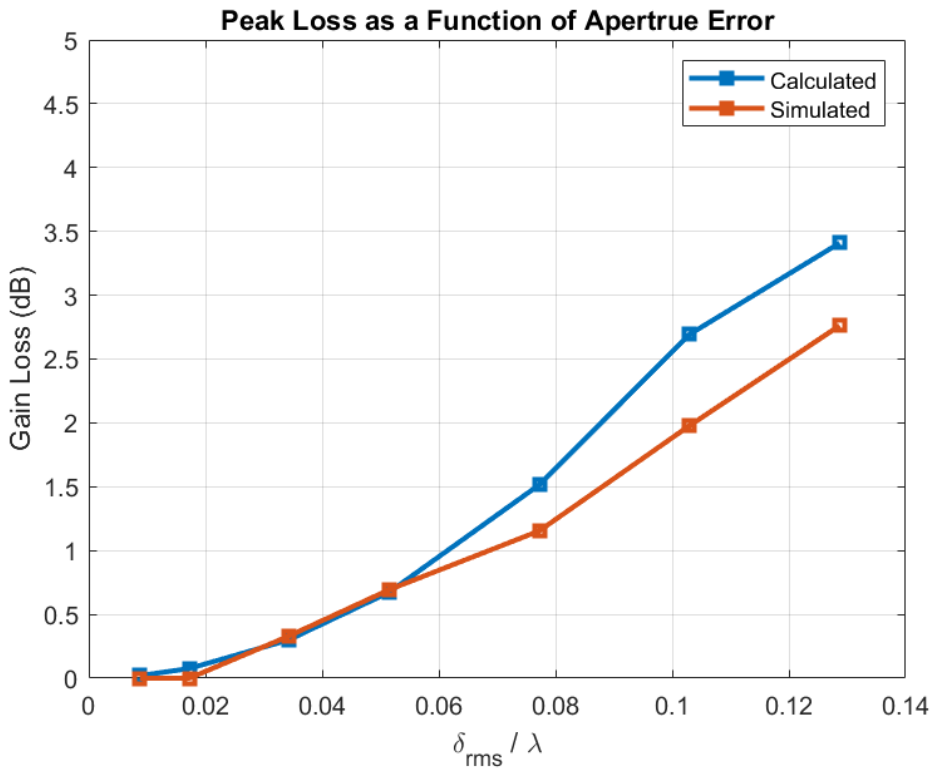

Figure 3.22: Calculated and simulated loss in gain due to reflector roughness.

The RMS roughness is varied from 3.2 to 47 μm and the aperture distortion (δ_{rms}) is calculated, along with the loss of gain on the system. For this scenario, a frequency of 500 GHz is selected and the ns spacing value is set to 1.2 mm. The feed is angled at 50 degrees. Table 3.6 relays the calculated and simulated results. Figure 3.22 portrays the comparison graphically.

As expected, as the surface roughness increases, the distortion in the aperture plane rises and the gain is reduced. The calculated and simulated values align fairly well but deviate more as the roughness increases. One explanation may be that the calculated values are the maximum loss of gain in the system expected, so the loss is greater than seen in some simulations. It is also accepted that Ruze's formulas are most accurate when the aperture error $\delta_{rms} < 0.1\lambda$ [58]. This is a healthy exercise to gain intuition on the reflector roughness impact on the system gain. It would not be unusual to observe a loss of more than 2 dB if the roughness is not considered a factor in the design process.

3.4 Reflector Fabrication

The previous sections show that 3D printed samples can meet the surface roughness requirements for fairly high frequencies. This allows for the green light to undergo the additive manufacturing process using PLA and to apply copper tape to add the reflectivity element.

Figure 3.23 illustrates the techniques employed to elevate the surface smoothness of the initial 3D printed components. Unfortunately, the ideal reflector size was too large to fit into the available working 3D printers at the time of the print. The largest reliable printer at the time was the Bambu Lab X1-Carbon printer with a maximum build size of 25.6 cm x 25.6 cm x 25.6 cm. To overcome this, the reflector was printed into four pieces. Different interlocking methods, such as the dovetail, were experimented with on a smaller scale. The

final print implemented a sliding technique, with an extra fixture printed that could slide onto the backing and hold all the pieces together.

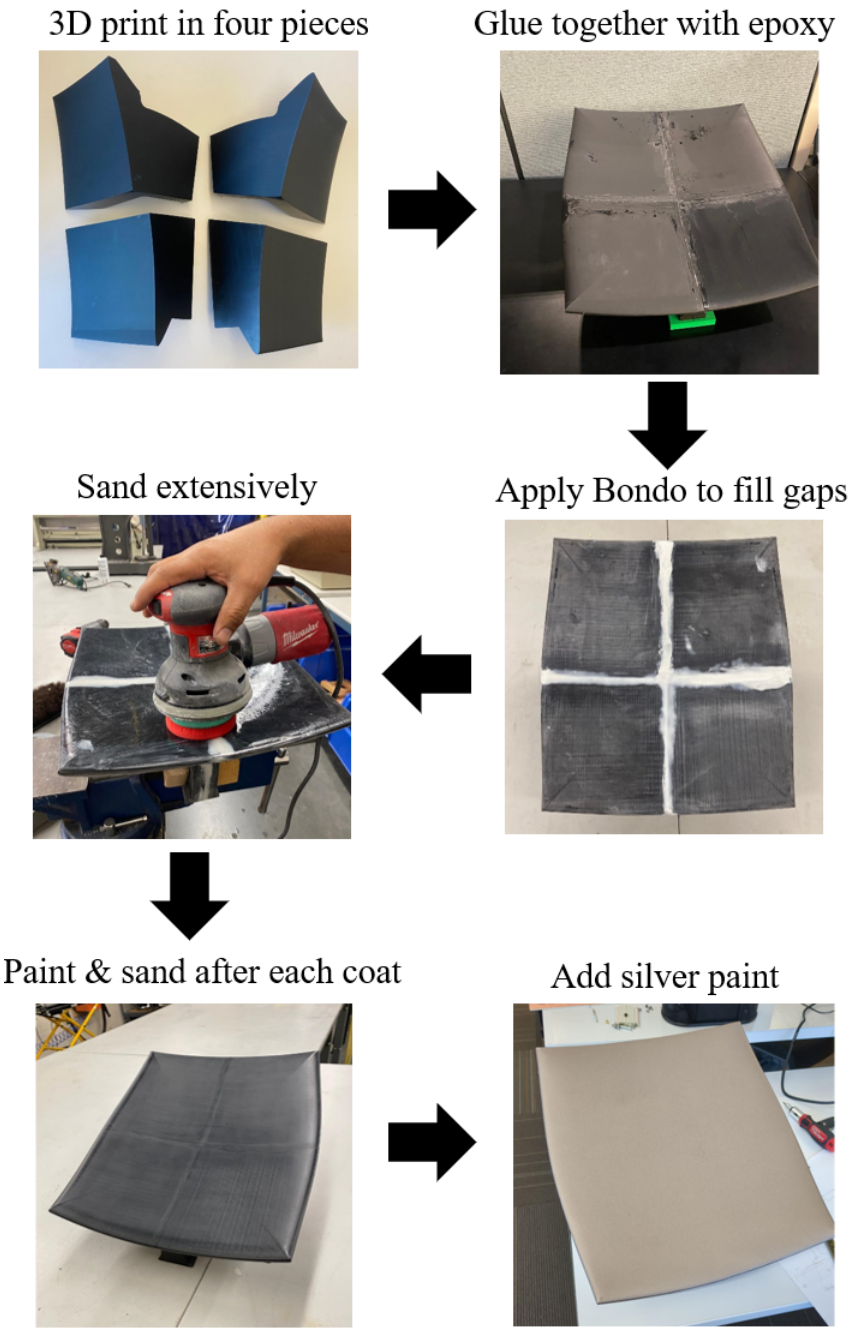

Figure 3.23: Fabrication process from initial 3D prints to silver coated reflector.

Epoxy was used to adhere the pieces together and once it had dried, the extra fixture holding the quarters in place was removed. The excess epoxy was sanded down and then Bondo was used to fill the few small gaps that remained at the intersection points where the edges didn't meet exactly. The reflector was sanded down including the excess Bondo. The reflector was sanded extensively, starting with a grit of 400 and graduating to 800, 1000, 1200, 1500, and 2000. At this point, a light coat of spray paint was added. After drying for 24 hours, the reflector was sanded again with fine sandpaper (grits of 2000, 3000, and 5000). This was repeated four times for a total of four paint coats. After the sanding and finishing, the silver paint could be added.

Similarly, a second reflector was created. The main difference is that the much larger Vivedino T-Rex 3 printer was used to print this copy, meaning it could be printed in one piece. The product employed Bondo to correct a few irregularities in the print and was sanded as extensively as the original. Finally, the copper tape was carefully added as seen in Figure 3.24.



Figure 3.24: Second 3D printed reflector in the process of being coated with copper tape.

3.5 Summary

In summary, this chapter outlined the beginning process and considerations for designing an offset parabolic reflector. Then it highlighted the process to add blended edges in both 2D and 3D. For the 3D design procedure, various considerations are discussed such as the blending options, the radius of curvature requirements, and the junction shape between the parabolic section and the blended edges. With respect to these discussions, a Ka-band blended edge reflector design is proposed. The main indicator of a well-designed blended rolled edge that sets it apart from the elliptical rolled edge is the difference in the radius of curvature when transitioning from the parabolic portion to the rolled edge portion of the reflector. This discontinuity is parameterized by the value ϵ_n. An ϵ_n value closer to zero indicates that the transition between the parabola and rolled edge is ideal. After applying a cosine-blended edge the reflector has an average ϵ_n of 0.653. The final size of the reflector is 38.12 cm x 39.91 xm x 18.22 cm.

Once the design is finalized, it is important to determine how to manufacture it and understand the potential limitations. This thesis proposes a creative and convenient solution to 3D print the reflector. However, it is understood that high frequencies face the challenge of increased sensitivity to surface roughness. Many simulations were performed to establish the frequency limitations for different surface roughnesses on the reflector. Frequencies of up to 200 GHz can tolerate an average surface roughness of 25 μm and maintain a theoretical phase variation of less than 5 degrees. It was discovered that average roughness is one parameter to consider, but another limiting factor is the space between the roughness peaks, ns. The 200 GHz upper bound applies when ns is less than 1000 μm.

Once the simulations highlighted the upper frequency bound, 3D printed samples were analyzed and their surface roughness was measured. The measurements, when compared to simulations, show that 3D printing the reflector is a valid option for fairly high frequencies.

All materials (PLA, ABS, and resin) meet the average surface roughness constraints when untreated, straight off the print build plate. Sanding is proven to have a significant impact on improving the surface smoothness further, achieving an average roughness of less than 1 μm for the resin and PLA samples. Adding silver paint, copper plating, or copper tape all satisfy the requirements with copper plating and tape as the best options ($<$ 1 μm of average roughness on all samples.)

With this confirmation, the reflector was fabricated. The fabrication process is demonstrated and the final reflector is depicted. With the realized reflector, the next step is to employ it in a measurement system to gather measurements. Chapter 4 outlines the other components of the system (VNA, positioners, etc) and Chapter 5 presents the measurements.

Chapter 4

Proposed System

This thesis mainly aims to understand, design, and implement the CATR reflector as the centerpiece of CATR systems and introduce a novel form of fabrication. Due to already-in-place Ka-band and W-band scanning systems available for use, it was unnecessary to reinvent the wheel by creating a new system. Rather, the existing in-place systems were analyzed to ensure their suitable capability, and modified to account for the reflector and new accompanying requirements. In the mmWave region, it is imperative that the system as a whole can perform accurate and repeatable measurements. For this reason, this chapter will outline the other critical pieces of the CATR system. This will allow a complete understanding of how the results, presented in Chapter 5, are yielded.

The scanning system consists of various positioners to situate the necessary components, such as the feed antenna, probe, and reflector. The scanner has a total of 4 independent controllers, 2 of them are linear positioners, 1 of them a rotary table, and, the last one, is a 6-axis arm robot. The first linear positioner moves the FE with the AUT or probe in the y-axis and the second linear positioner moves the FE with the AUT or probe in the z-axis. Combined, these two linear positioners form an inverted T-positioner, common in antenna measurement setups. The frequency extender is placed with the AUT or probe to minimize any RF cable movement that may strain the cables, and lead to degradation over time or worsened measurement results. The rotary table enables the polarization rotation

(0 - 360 degrees) of the antenna probe, allowing easy accommodation to measure co- and cross-measurements of E-, D-, and H-planes. The reflector is mounted on a robot arm that has 6 degrees of freedom. The reflector is mounted with a 3D-printed fixture that attaches to the robot hand. The feed antenna illuminating the reflector is positioned by a mount with an adjustable angle bracket.

The appropriate RF cables and frequency extenders are attached to the antennas and to the VNA for measurements. With the exception of the robot arm, these components are all controlled via a MATLAB interface to dictate the appropriate positions as well as the FE and VNA settings (frequency, number of points, etc).

The assembly of these components, similar to as shown in Figure 4.1, allows for high-accuracy and repeatability of measurements. The following sections will outline the features of each component.

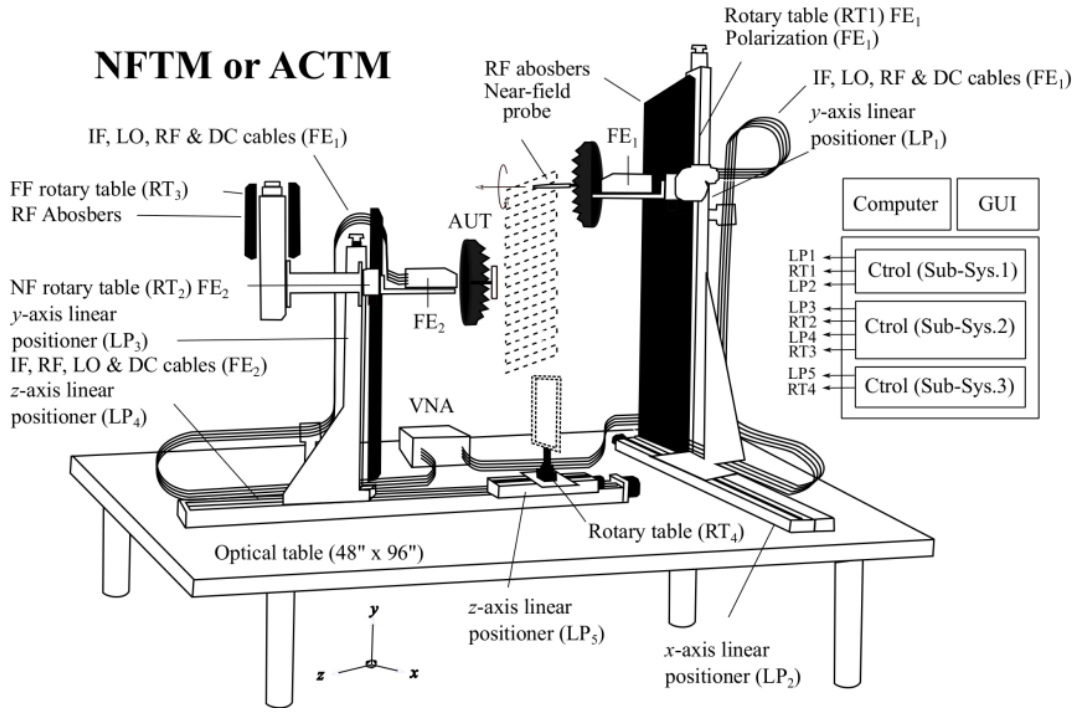

Figure 4.1: Similar mmWave metrology system that inspired the arrangement of the current system [64].

4.1 Vector Network Analyzer and Frequency Extenders

For Ka-band measurements, the Copper Mountain S5243 2-Port network analyzer was selected that can operate from 10 MHz to 44 GHz. The additional CobaltFx frequency extenders provide operation from 75 GHz to 110 GHz. The use of both these components ensures the system can adequately measure s-parameters (from which phase and amplitude can be extracted) in Ka-band and W-band frequency spectrums.

The accuracy of the CMT S5243 VNA, as well as the flexibility in frequency and time domain measurements, and overall high-performing specifications, makes it a recommendable tool. The S5243 VNA is in Copper Mountain's line of compact VNAs, meaning it is of much smaller size and weight than many VNAs but with minimal impact to performance. VNAs can be costly machines due to the required precision. VNAs that cover larger and higher frequency ranges can be especially costly and sensitive. For this reason, frequency extenders are employed to expand the measurable frequency range from Ka-band up to W-band. The CobaltFx FE system has been proven to be a versatile and cost-effective tool for precise metrology measurements with repeatable results. Fast sweep speeds down to 10 µsec per point and a dynamic range of up to 110 dB, combined with a compact USB form factor, make it an ideal RF instrument for this system. Table 4.1 characterizes a few of the

Table 4.1: Instrumentation specifications as gathered from [65] and [66]

Parameters	VNA (CMT S5243)	FE (CobaltFx FEV-10)
Freq. operation	10 MHz - 44 GHz	75 GHz - 110 GHz
Test Pout	-50 dBm to 0 dBm	0 dBm to 5 dBm
Dynamic range	>135 dB	110 dB
AC/DC power	110-240 V (60 Hz)	6 V at 2.2 A
Weight	5 kg	3-5 kg
Temp. operation	5-40° C	0-30° C

specifications for each hardware component. The accuracy of a CATR system's measurements is largely limited by the equipment responsible for collecting those measurements, so it is crucial to start with strong and reliable VNAs and FEs as the basis.

4.2 Positioners

The VNA and FEs are important for determining the accuracy of the s-parameter measurements that can be taken, but it is equally important that the positioners present the same level of precision. If the positioners are off by a few millimeters, especially in the mmWave frequency spectrum, the VNA is measuring what one can consider to be near-useless data. As has been reiterated many times, higher frequency levels require increased accuracy and precision. For this system, the main positioners include the VELMEX bisliders, VELMEX rotary table, and the Universal Robot 3 (UR3).

The motorized bisliders have a repeatability of 0.005 mm and a straight line accuracy of 0.076 mm across the entire travel distance of 560 cm, making it a promising option for the applicable frequency spectrum. The VELMEX bisliders are also convenient due to their modular design, making them highly configurable for different setups. This easy configurability allows for the inverted T-positioning setup rigged for this system. The bisliders are capable of carrying up to 300 lbs. horizontally and 100 lbs. vertically, which is more than sufficient for the relevant load of the frequency extender, AUT/probe, and any applicable fixtures [67].

The VELMEX rotary table offers performance of a similar caliber, featuring ultra-precision and durability. The rotary tables have a load capacity of up to 200 lbs. horizontally and 25 lbs. vertically. They are also easy to integrate with the bisliders in an array of configurations for utmost flexibility [67].

Both the VELMEX bisliders and rotary tables can be controlled with the VXM step-

per motor controller. These motor controllers govern the performance of the positioners and allow for simple and precise positioning of the slides and tables. The VXM is given commands by MATLAB via a serial communication protocol, which is a reliable and steadfast method. Rather than introducing uncertainty by manually moving the rotary table, the VXM allows for the rotary table to be moved in as small as 0.0125 degree motorized steps [67].

The UR3, 6-axis robot arm, is another helpful component. While the VELMEX system is responsible for positioning the probe, the UR3 aligns the reflector. The six degrees of freedom include the base, the shoulder, the elbow, and the three wrist joints. This allows utmost flexibility when positioning the reflector and the feed antenna. The UR3 boasts a repeatability of 0.1 mm and a reach of 50 cm. Like the VELMEX positioners it can also be controlled via MATLAB, although through a TCP/IP communication protocol. While the rest of the scanning system has centralized control with a master MATLAB interface, the UR3 was an added feature for the purposes of the CATR system. Recall that the majority of this system was already in place and is slightly modified to account for the CATR needs. Though the UR3 is not integrated into the main system software, it is still possible to program the robot's position and movement, or to simply use the touchscreen interface provided to control the robot. The maximum payload is 3 kg (6.6 lbs) which is not exceeded with the 3D-printed reflector and additional fixtures. The typical power consumption is 125 W [68]. Figure 4.2 highlights the robot and provides a visual for the numerous axes of freedom.



Figure 4.2: Universal Robots 3 (UR3) positioning tool [68].

One of the reasons the UR3 is a useful tool is due to the calibration needs of the system. Calibrating the reflector position and ensuring everything is aligned is a time-consuming and difficult process. The UR3 conveniently allows for control over aligning the reflector along each axis and in tilting different directions.

4.3 Feed antenna

The trade-offs and advantages of different feeding probes have already been discussed in Section 2.2.4, concluding that a corrugated conical horn antenna would be best for many scenarios. However, due to the Ka-band scanning system already being in place, the CATR system utilizes an already-available antenna. The feed antenna available is the Narda-ATM Ka-band standard gain horn antenna. This antenna was simulated in HFSS and the resulting antenna pattern, gain, and return loss are highlighted in Figure 4.4.

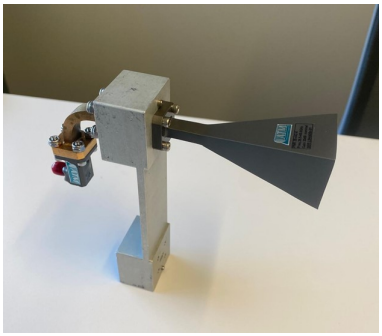

Figure 4.3: ATM Ka-band standard gain horn antenna.

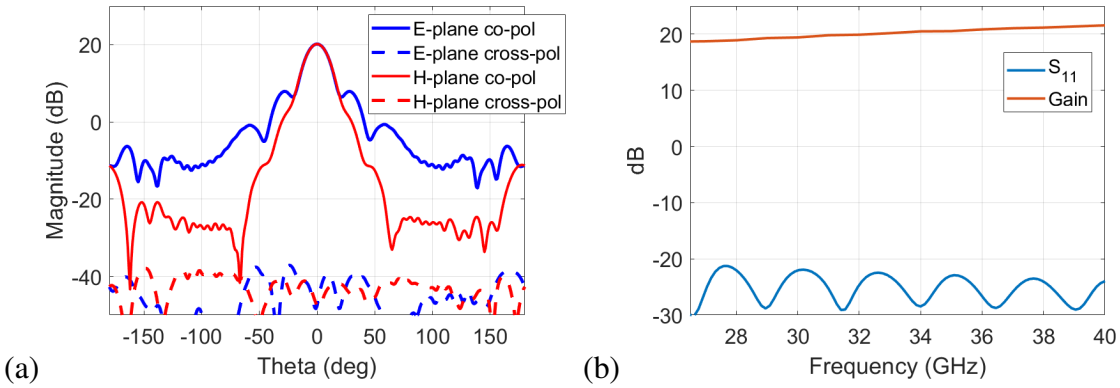

Figure 4.4: ATM standard gain horn (a) antenna pattern at 33 GHz and (b) gain and return loss over frequency.

The HPBW is 18.2 degrees. The subtended angle of the parabolic portion of the final reflector design is 26.5 degrees. The beamwidth taper extended from the azimuth angle of -13.25 degrees to +13.25 degrees is 6.6 dB. For this system, it would be best to have a constant amplitude taper pattern across the parabolic section of the reflector because the blended edges on the reflector ensures it is not as susceptible to edge diffractions from spillover. So, while this antenna is slightly more directive than ideal, it is still more than acceptable to use as the feed antenna.

4.4 Probe Antenna

The Ka-band antenna placed in the quiet zone of the system is Microwave Vision Group's (MVG's) pyramidal horn antenna model number SGH2650. This singularly polarized horn antenna operates from 26.5 to 40 GHz with a gain of 24.7 dB at the center frequency. According to the datasheet, the VSWR is quite low at less than 1.4 (-15 dB) and the cross-polarization discrimination is excellent at $>$ 40 dB [69]. This antenna is selected as the probe instead of an open-ended waveguide because the waveguide was hypothesized to have too broad of a beamwidth that might capture spurious signals outside of that which is coming from the reflector.

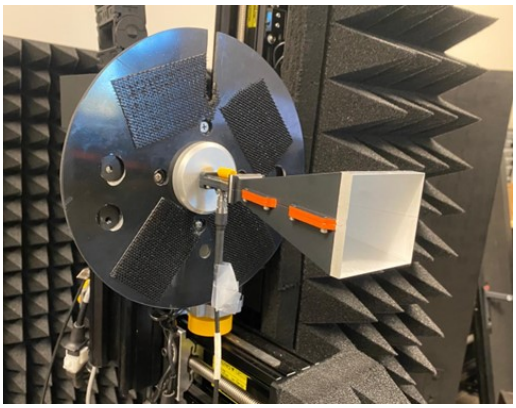

Figure 4.5: MVG Standard Gain Horn Antenna.

4.5 Other Components

The remaining components include the rotary joint, RF cables, cable tracks, and absorbers.

The rotary joint is important to allow for seamless movement and revolutions of the necessary equipment, such as the antennas, without twisting the RF cables. A single channel rotary joint (of I-style connection) with a frequency range of DC to 50 GHz is utilized.

Like most things, the rotary joint offers better performance at the lower end of it's frequency span. At the far end, up to 50 GHz, the rated power is 3W, the maximum VSWR is 1.7 (0.2 deviation during rotation), and the loss is 0.9 dB. Thus, it still maintains relatively good parameters through and past Ka-band. Also note that the maximum phase deviation during maximum rotation is 2 degrees. Overall, this is by far the best option found on the market for this frequency range and at a reasonable price.

Another common point of loss in the link budget is the RF cables. 2.92 mm RF cables from Mini Circuits are utilized with a typical loss of 2.2 dB throughout, which is relatively common and acceptable. A high gain, although important, is not the main objective of this CATR system which is focused on generating a ripple-free QZ. The RF cables employed work comfortably up to 34 GHz, meaning they are currently the limiting factor in measuring the entirety of Ka-band.

Concerning the absorbers, ideally the wall behind a serrated edge reflector may be treated with a shorter absorber, usually $\lambda/2$ in thickness, and it only needs to cover the regions of the wall that are not obscured by the reflector body. For rolled edge reflectors, the entire wall should be fully treated with an absorber [35]. For a compact range, this is the most critical wall and therefore should have the lowest reflectivity [35]. Unfortunately, the current setup of the system is in a large room and the back of the reflector is not oriented against a wall so it is difficult to arrange absorbers there. However, there are walls of absorbers on the opposite side, behind the AUT. There are also absorbers placed on the sides of the system.

4.6 Summary

Previous chapters focused solely on the reflector but more pieces are needed to obtain measurements. This chapter highlights the other components of the CATR system, with-

out which the reflector would be useless. The other instruments operate comfortably in the mmWave spectrum, starting at Ka-band, except the RF cables which operate up to 34 GHz. The VNA and FE's are selected to ensure precise and adequate measurements can be gathered. The available antennas are acceptable choices for this system. The positioners such as the UR3 allow for generous flexibility in aligning the components which is helpful in calibration. Other components meet the system specs as needed. Figure 4.6 displays the components all assembled. Now that the system specifications have been outlined, the following chapter presents the results yielded by this system.

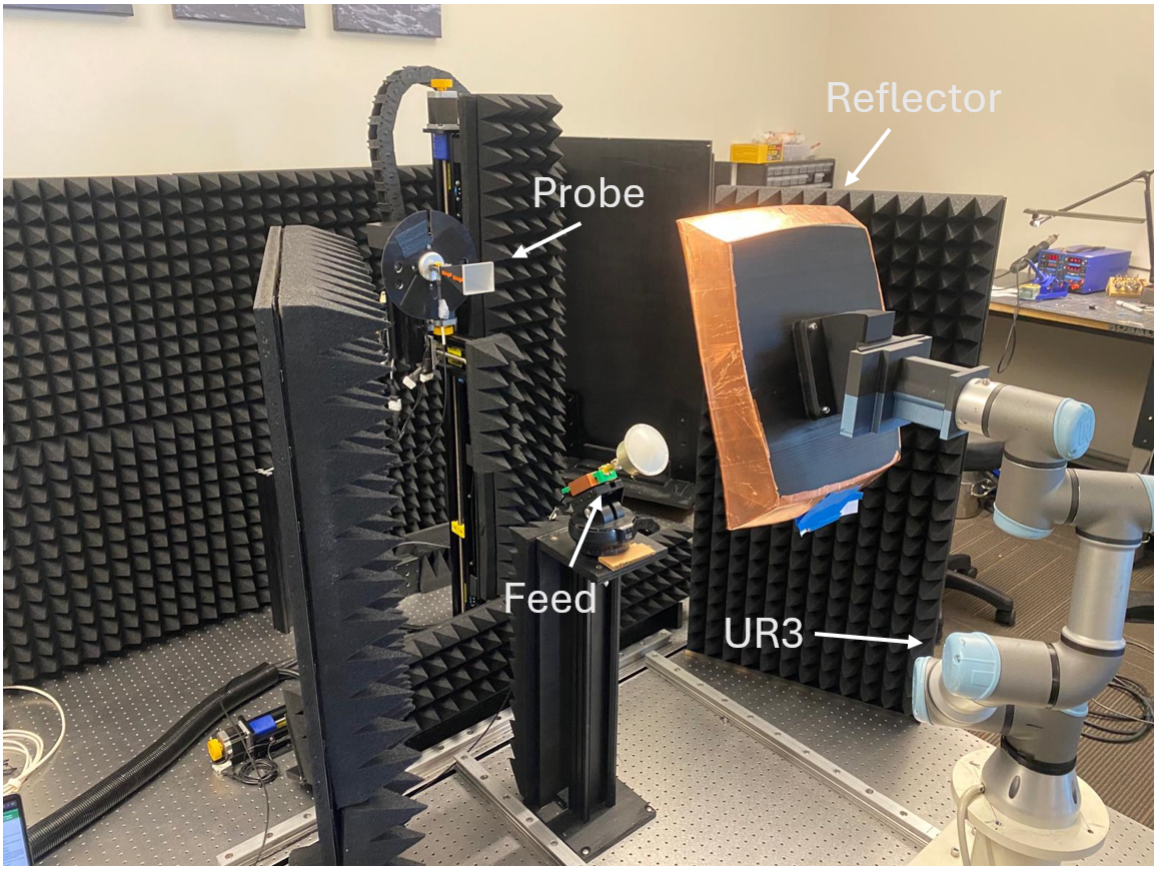

Figure 4.6: Ka-band CATR system.

Chapter 5

Tests and Validation

With the reflector designed and fabricated and the CATR system in place, measurements can be obtained. The CATR components can operate in Ka-band from 26.5 GHz to 34 GHz. Based on the surface roughness analysis completed in Chapter 3, in theory, the reflector can operate in Ka-band and up to W-band well. This chapter includes measured results in the Ka-band spectrum to prove the validity of the reflector. Two versions of the reflector were produced, one carefully covered in copper tape and the other coated with silver paint by a professional automotive finisher. Both are presented and compared.

5.1 Copper Taped Reflector Measurements

The copper taped reflector was measured to have a resistance of 0.2 ohms, meaning it is highly conductive and reflective. The probe scanned a grid covering the entirety of the reflector (20 cm x 20 cm) at 80 cm away from the reflector. Figure 5.1 displays the scanning area of the following measurements and the size of the QZ (12 cm x 10 cm) within the scanned area. The QZ size aligns with the size of the parabolic portion outlined in the design process in Section 3.2.2.

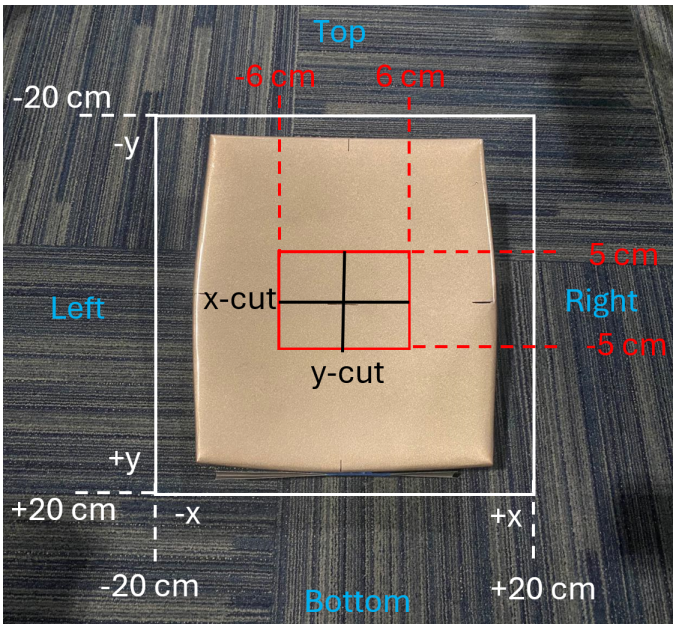

Figure 5.1: Visual of total scan size compared to expected quiet zone size overlayed on the reflector as a guide for the following figures.

Figure 5.2 displays the magnitude and phase of the entire reflector as seen 80 cm away for various frequencies. Figure 5.3 depicts the 'zoomed in' data, featuring the results from the QZ alone. Although the reflector and feed were aligned well, the probe scanned at a slight offset, so the QZ is not directly in the center of the data plots. The plots in Figure 5.3 reflect the actual location of the QZ and confirm that it maintains the 12 cm x 10 cm size. These figures reveal ample consistency of the magnitude and phase in the QZ.

Recall from Section 2.1.3 which outlined the IEEE QZ specifications that the ideal magnitude variation along a cut plane is < 0.25 dB and the phase variation is < 11.25 degrees. Although it is often common practice to lessen the magnitude requirements to less than 1 dB variation and, technically, standard far-field requirements achieve 22.5 degrees. The proposed goal was < 11.25 degree phase variation and < 1 dB magnitude variation.

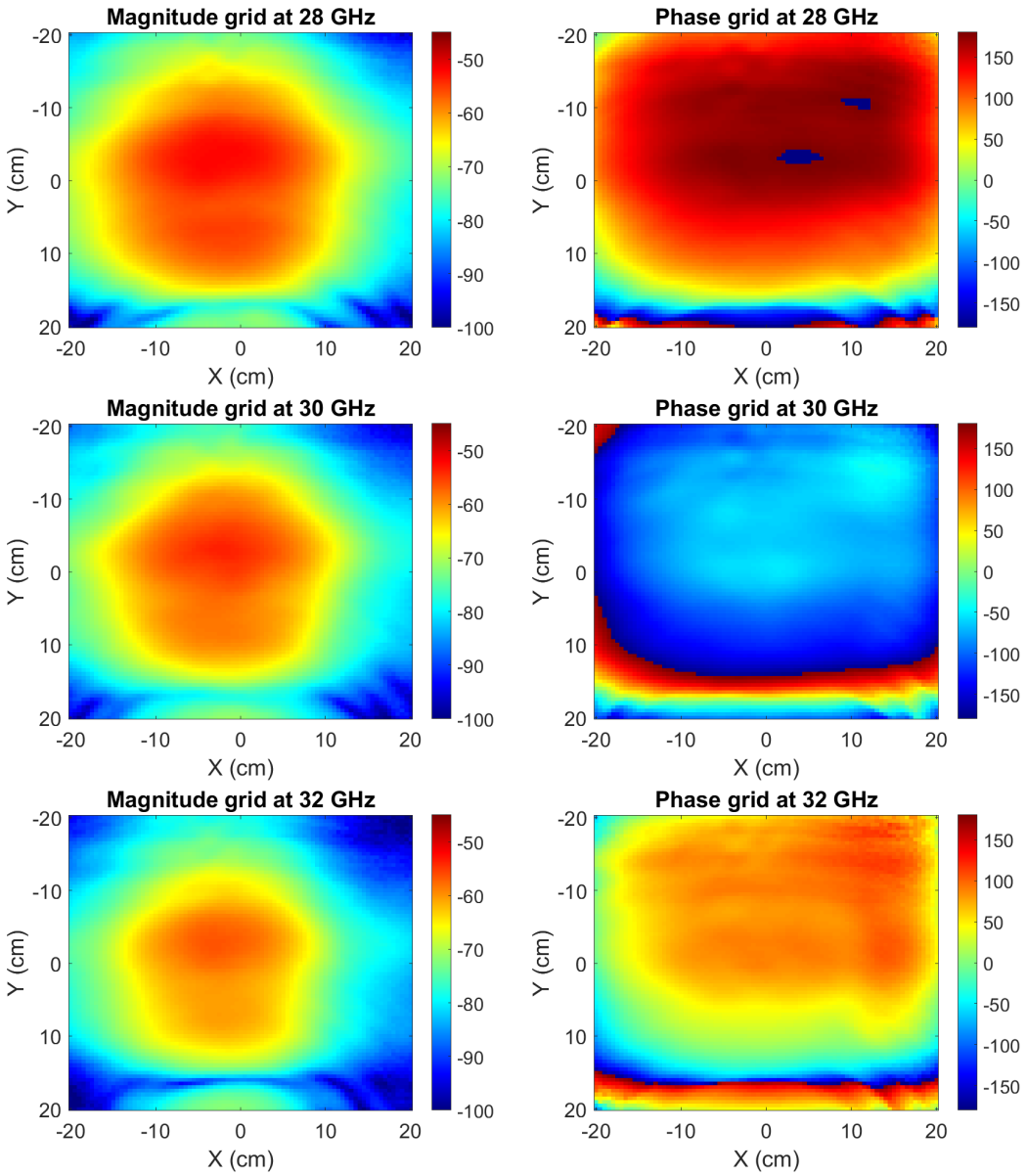

Figure 5.2: Measured magnitude and phase grids with copper taped reflector.

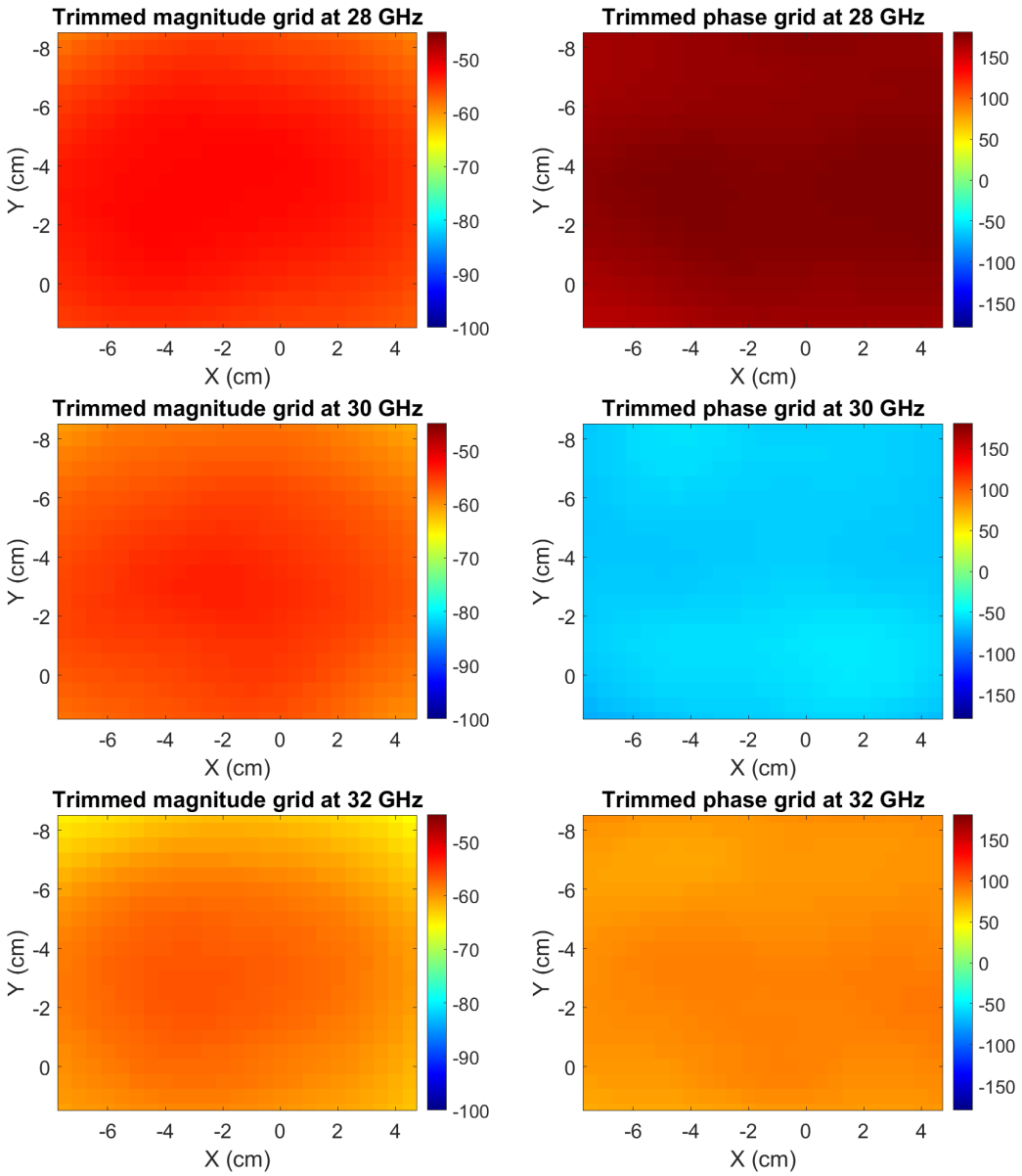

Figure 5.3: Measured magnitude and phase grids of quiet zone (12 cm x 10 cm) with copper taped reflector.

Since antennas are often measured in cuts, it is important the $x-$ and $y-$ cut planes demonstrate consistent phase. Figure 5.4 expresses the phase of the cut planes in the center of the QZ for the measured frequency range. It is confirmed that the phase is successfully stable. Figure 5.5 depicts the calculated variation of the cuts seen in Figure 5.4 across the

frequency spectrum. The ideal variation requirements are plotted for comparison. It can be seen that both the $x-$ and $y-$ cuts exceed the ideal goal of phase variation under 11.25 degrees. The average phase variation across all the plotted data points is an exceptional 2.28 degrees in the $x-$axis and 7.58 degrees in the $y-$axis.

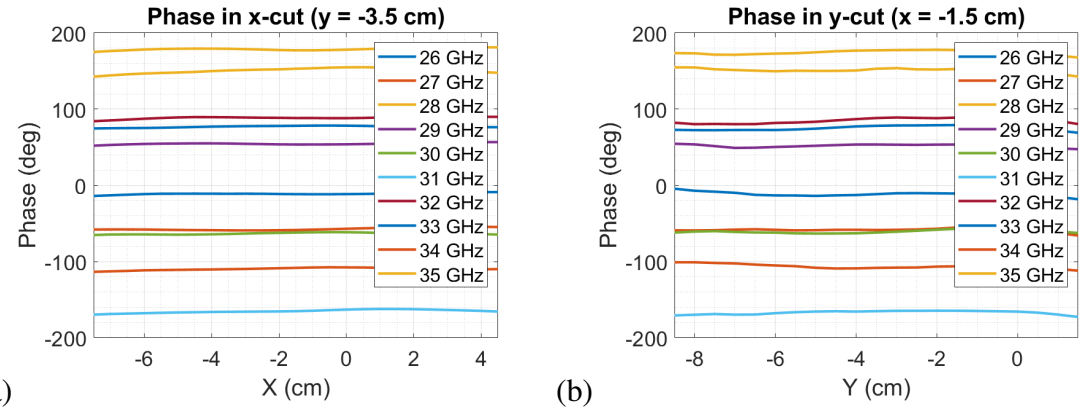

(a) (b)

Figure 5.4: Quiet zone phase cuts of copper reflector in (a) $x-$ and (b) $y-$ planes.

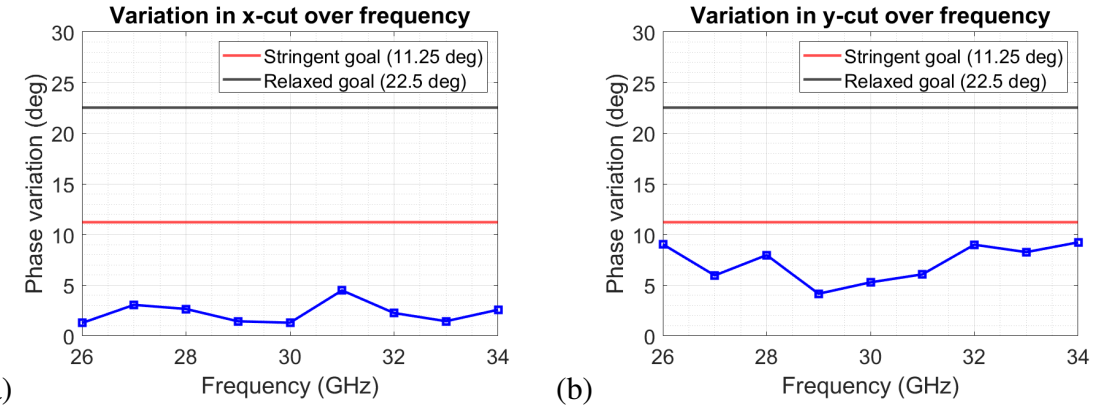

(a) (b)

Figure 5.5: Variation of phase over frequency for phase cuts viewed in Figure 5.4 for (a) $x-$ and (b) $y-$ planes.

A similar analysis is performed for the cut planes of the magnitude. Figure 5.6 exhibits the magnitude of $x-$ and $y-$cuts for each frequency point. Following this visual, Figure 5.7 presents the variation of the second-degree polynomial fit, as is the recommended technique by IEEE standards for antenna measurements [35].

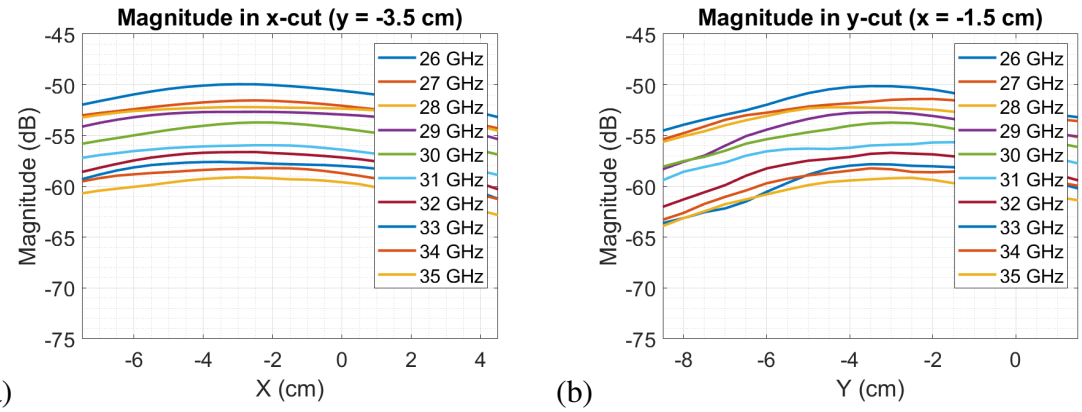

(a) (b)

Figure 5.6: Quiet zone magnitude cuts of copper reflector in (a) $x-$ and (b) $y-$ planes.

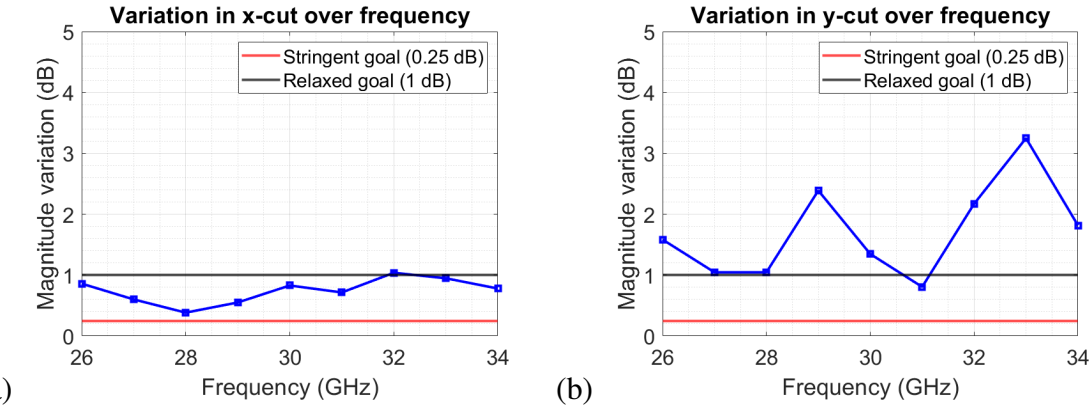

(a) (b)

Figure 5.7: Variation of magnitude over frequency for magnitude cuts viewed in Figure 5.6 for (a) $x-$ and (b) $y-$ planes.

It can be seen that the magnitude is relatively consistent across the QZ, and surpasses the requirements in the $x-$cut. The full-size $y-$ cut does not quite meet the desired requirements. The average magnitude variation across the measured frequencies is 0.74 dB and 1.72 dB in the $x-$ and $y-$ cuts, respectively. Trimming the QZ size in the $y-$plane allows for smaller, better variation. A size of 10 cm yielded a taper of 1.72 dB, then 9.5 cm yielded 1.25 dB, 9 cm yielded 0.9 dB, and 8 cm yielded 0.47 dB. In this way, the QZ size is a tradeoff that can be sacrificed for best performance.

It is probable that a feed antenna with a broader beamwidth would more evenly illu-

minate the reflector and allow for better magnitude variation. It has been concluded in Section 2.2.5, which explored the effect of feed antennas with different beamwidths, that it is difficult to achieve minimal variation in both magnitude and phase. The reason is that a feed with a wider beamwidth covers a larger area of the reflector with even contact and allows for a larger QZ with stable magnitude. However, the wider beamwidth infringes on the reflector rim and introduces additional edge diffractions that are more likely to disrupt the phase. However, that case study was for a reflector without edge treatments such as a blended rolled edge. Thus, it is safe to say that in this instance, swapping the feed antenna for one with a wider beamwidth would not cause as severe a tradeoff in the phase. So, one solution to resolve the slight error in magnitude variation would be using a different feed antenna.

Another possible explanation could be slight imperfections in the calibration of the system. It was found that tilting the reflector by merely 0.05 degrees resulted in a phase change in the QZ of 10 degrees. A slight offset in alignment can have significant repercussions on the serenity of the QZ. While the UR3 is an outstanding and convenient tool, it does not have the precision that professionally made CATRs possess.

It should also be mentioned that there are minor imperfections in the applications of copper tape. For example, the seams between tape strips are unavoidable and can reasonably cause shortcomings in the QZ perfection. Minor bumps and ridges were also inevitable inside the strips of tape. Chapter 3 demonstrated the smoothness of a small sample of copper tape on a flat surface, but a larger curved surface is bound to introduce some issues.

Thus, while favorable results were achieved with the copper-taped reflector, there is room for improvement to realize an even better QZ.

The following section dissects the measurements captured with the silver painted reflector for comparison purposes.

5.2 Silver Painted Reflector Measurements

The silver paint was measured to have a resistance of 1 ohm, which is comparable to the copper tape. Figure 5.8 displays the magnitude and phase of the entire reflector as seen 80 cm away for various frequencies. Figure 5.9 presents the results from the QZ alone.

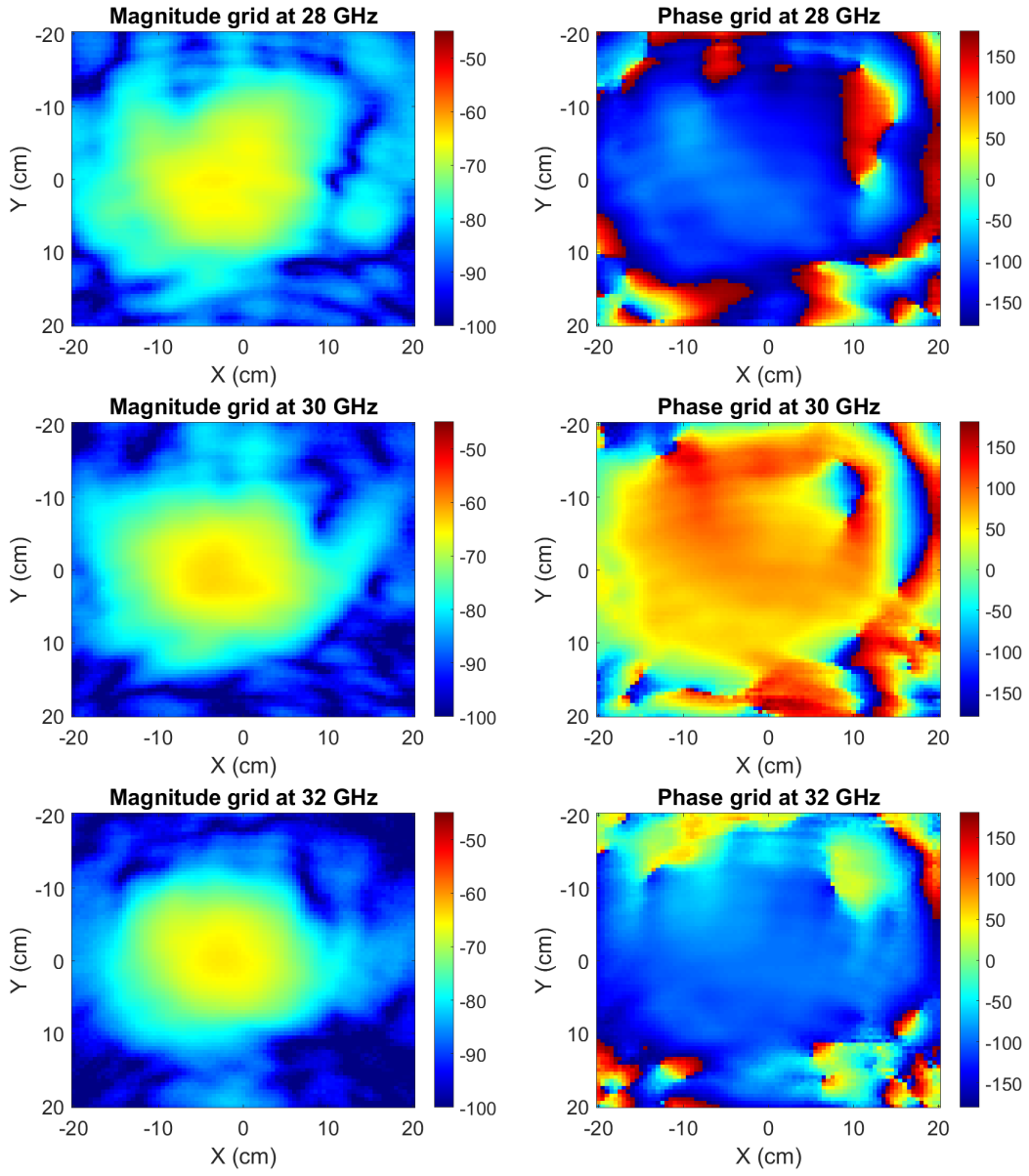

Figure 5.8: Measured magnitude and phase grids with silver painted reflector.

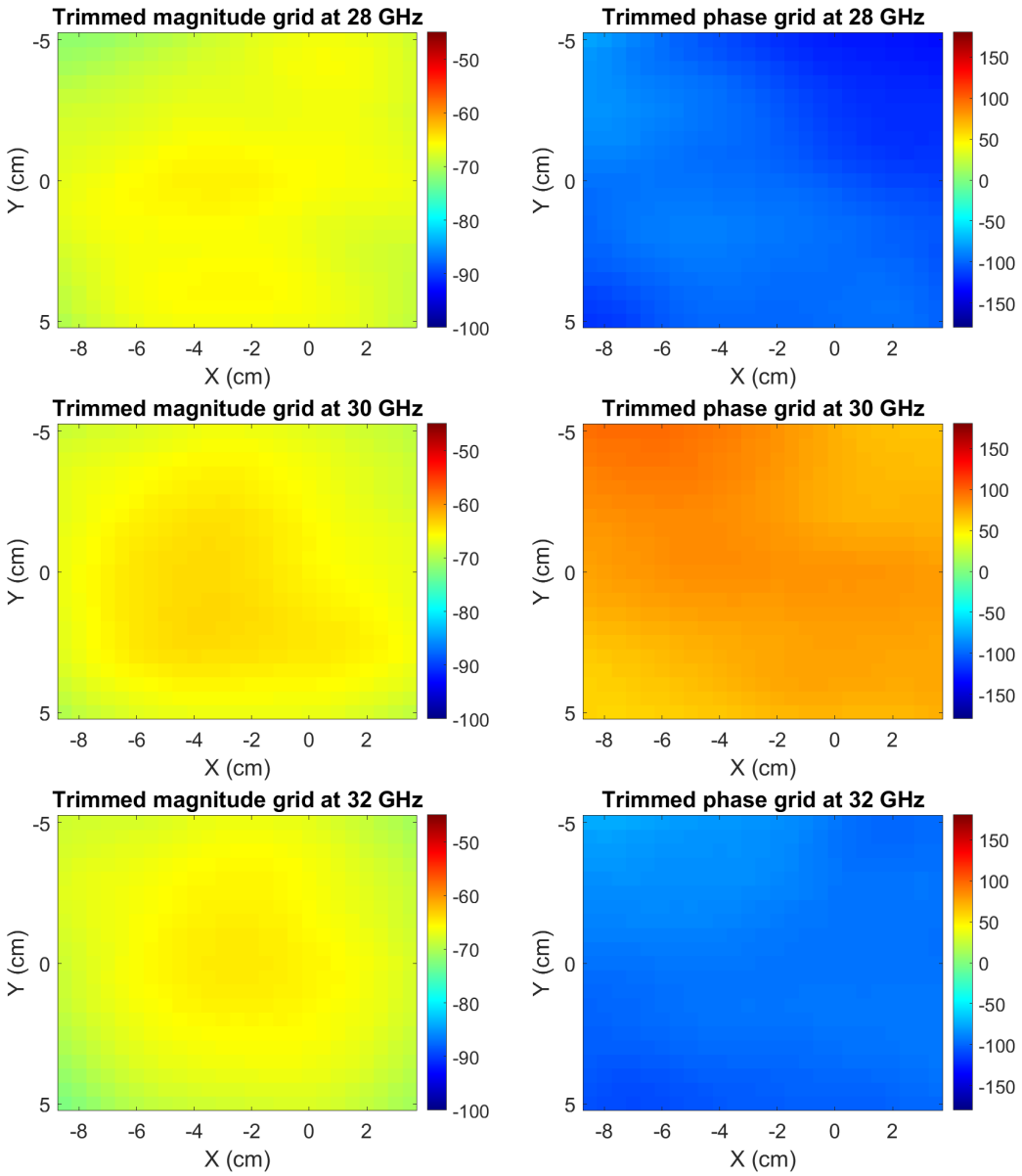

Figure 5.9: Measured magnitude and phase grids of quiet zone (12 cm x 10 cm) with silver painted reflector.

At first glance, compared to the copper taped reflector it can be seen that the QZ is not as crisp. The magnitude is also about 20 dB lower than what was seen with the copper reflector. The epoxy that the silver reflector is coated with is potentially dissipating some of the energy and limiting the reflectivity. Overall, across the QZ a relative consistency is

seen to be maintained.

As presented for the copper taped reflector, the silver painted reflector's phase and magnitude of the $x-$ and $y-$ cuts are shown in Figure 5.10, and the variation of each is calculated in Figure 5.11.

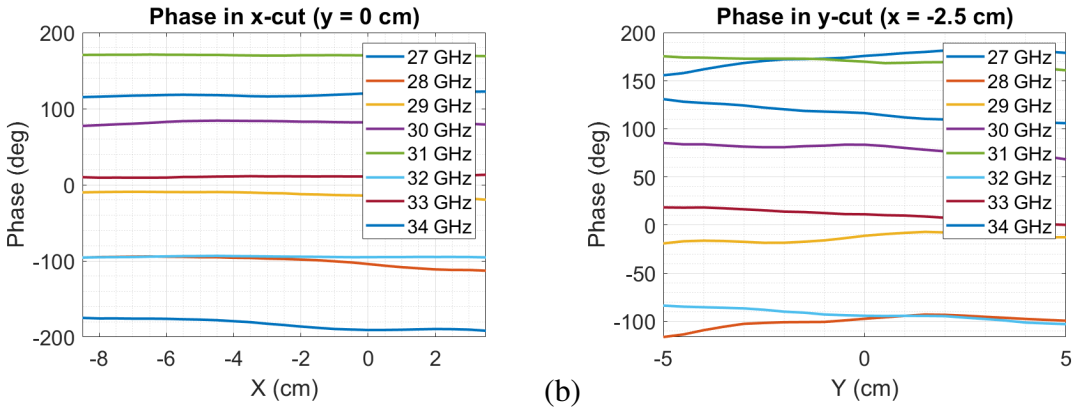

(a) (b)

Figure 5.10: Quiet zone phase cuts of silver reflector in (a) $x-$ and (b) $y-$ planes.

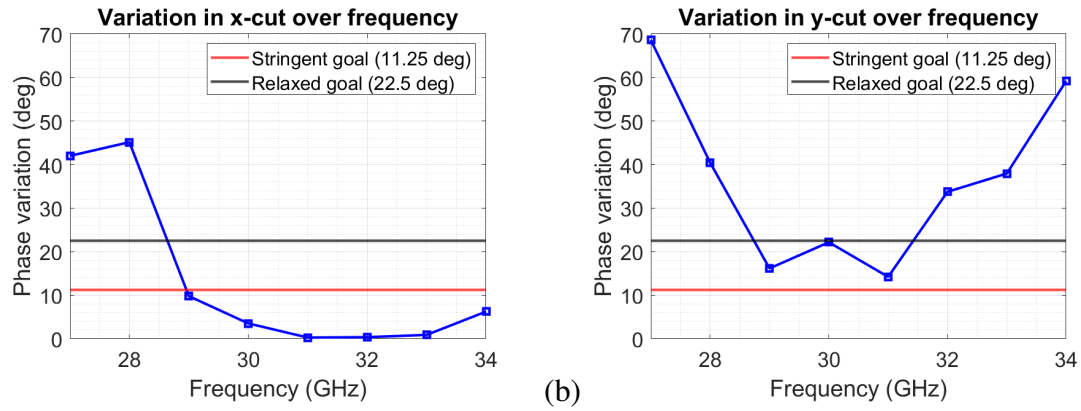

(a) (b)

Figure 5.11: Variation of phase over frequency for phase cuts viewed in Figure 5.10 for (a) $x-$ and (b) $y-$ planes.

It is seen that the $x-$cut has favorable results at 29 GHz and above. The $y-$cuts are best for 29 GHz - 31 GHz, although only the standard far field requirement of 22.5 degrees is met. The average phase variation is 13.52 degrees in $x-$ and 36.56 degrees in the $y-$plane. Figures 5.12 and 5.13 demonstrate this analysis for the magnitude results.

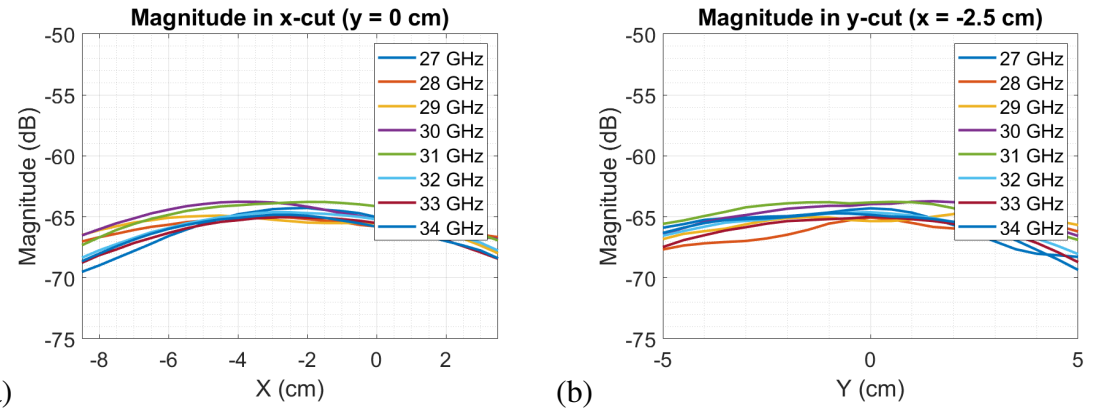

Figure 5.12: Quiet zone magnitude cuts of silver reflector in (a) $x-$ and (b) $y-$ planes.

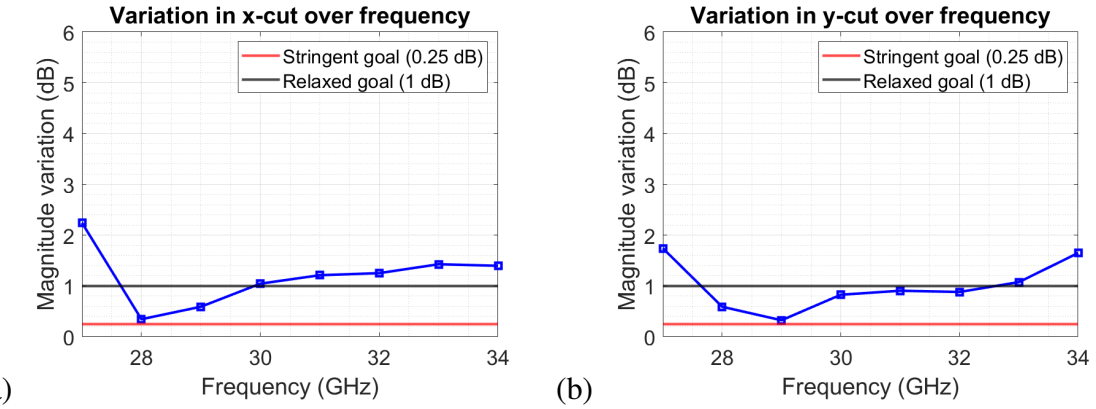

Figure 5.13: Variation of magnitude over frequency for magnitude cuts viewed in Figure 5.10 for (a) $x-$ and (b) $y-$ planes.

The magnitude variation for both planes is promising with an average variation of 1.03 dB and 0.85 dB in $x-$ and $y-$, respectively.

As stated in the previous section, imperfections could be due to limitations in the calibration equipment or blemishes in the surface, and overall improvements might be seen with a different feed antenna. It is also possible that the phase results are not as favorable as seen in the copper reflector due to the reduction in magnitude. As the noise floor is approached, the phase becomes more erratic. This could be easily overcome with the use of an amplifier. Another reason this reflector might not have as pure of phase is that this one

was printed in four pieces and then assembled. This means that the parabolic shape might not be as exact as needed or as accurate as seen with the copper reflector which was printed in one piece.

5.3 Summary

It is established that an excellent QZ can be achieved with the current 3D-printed reflector design. The data is presented extensively in this chapter, but Table 5.1 summarizes the QZ results for each reflector. The copper reflector outperforms the silver in most aspects. Despite possible modifications, it is shown that the reflector design does perform well and surpasses many expectations. This means that the design process of the blended edges in Chapter 3 is demonstrated to be reasonable and that the fabrication process of 3D printing is a valid method for Ka-band measurements. Chapter 6 considers the previous chapters and the results of this chapter to present the conclusion of this work.

Table 5.1: Average QZ phase and magnitude variation across the measured frequency spectrum for each reflector. The QZ is 12 cm x 10 cm.

Reflector	Cut Plane	Magnitude variation	Phase variation
Copper	$x-$	0.74 dB	2.28 degrees
	$y-$	1.71 dB	7.58 degrees
Silver	$x-$	1.03 dB	13.52 degrees
	$y-$	0.85 dB	36.56 degreees

Chapter 6

Conclusion

6.1 Summary of Work

The goal of this thesis was to design, develop, and test an additive-manufactured reflector for a high-frequency compact antenna test range. Traditional methods for mmWave antenna metrology require larger test facilities (far field ranges) or are more computationally taxing (near field ranges). A CATR transforms a spherical wave into a plane wave with all the benefits of far field ranges but at a shorter range. CATRs are advantageous over near field systems because they do not require collecting a complete set of data over the test antenna aperture to evaluate a single far-field pattern cut. This allows for rapid evaluation of antenna performance. This project was embarked on for these reasons.

In this study the amplitude and phase quiet zone requirements of a compact antenna test range were outlined as guidance for the end goal product. Chapter 2 proposed several case studies illuminating the design considerations for different cases including, but not limited to, the ideal feed antenna type and the optimal depth of the reflector dish.

The mathematical theory behind offset parabolic reflectors and rolled edges is significantly studied. Specifically blended edges are extensively explored and analytically explained. The design procedure is outlined step by step with multiple examples included. The design procedure for the final constructed Ka-band reflector is explained including

the total size constraints, minimum radius of curvature requirement, and junction contour shape between the parabolic and blended sections.

Simulation and measured results are presented to prove that the proposal of an additive-manufactured reflector is valid. The surface roughness study presented is unlike any seen in current literature. TICRA GRASP simulations demonstrate the quiet zone variation and gain reduction produced by surface roughness. It is shown that, in certain cases, a reflector's average surface roughness can be up to 25 μm and still operate up to 200 GHz with only a 2 degree increase in phase variation. Several 3D printed materials are examined to quantify their surface roughness. Reflective materials are applied to the samples as is required for a plastic 3D printed reflector to work, and the new surface roughness is scrutinized. With the guiding parameters outlined by the simulations, it is found that the metallic-coated 3D printed objects will operate well into the mmWave bands.

The creation of the reflector is described from birth to realization. First, general trade-offs of the reflector are evaluated and considered, with electromagnetic theory and additional simulations. Second, understanding the mathematical requirements for the parabolic reflectors, rolled edges, and blended edges to then producing a design with this analysis and manufacturing constraints in mind is presented. Then once a design is finalized the surface roughness constraints are defined and the 3D printing solution is confirmed. The manufacturing process is described and the final reflectors are shown.

The rest of the CATR system is highlighted to provide context on how the reflector is integrated into the system and to provide transparency on how the final results are obtained. Chapter 5 presents the preliminary results as a culmination of this work which are analyzed and explained. The final product produces a pure quiet zone with stable magnitude and phase across it. One reflector achieved an average phase variation of 2.28 degrees and 7.58 degrees in the $x-$ and $y-$ cuts, respectively. This is well below the requirements of 11.25 degree variation.

6.2 Contributions

The work presented in this thesis has contributed to the antenna metrology field in several ways. One notable addition to current literature is the novel idea of implementing an additive-manufactured reflector. This is a significant change from traditionally milled metal reflectors. This alternative is substantially less expensive, more convenient, and less wasteful. The 3D printer size limitation is overcome as a method is presented that prints the reflector into sections and adheres them together. Multiple techniques to coat the reflector with a metallic exterior are investigated and shown to be compelling options. The Ka-band design itself is also worthy as new knowledge that can be helpful to others.

Another contribution to current literature is the quantification of the upper bound of frequency for reflectors of different surface roughness. These guidelines proved helpful with the design of the proposed Ka-band reflector and can be helpful to others undergoing a similar process. This is an especially important contribution in the context of the ongoing race towards higher frequencies. Industry and academia alike are propelling to higher frequency spectrums and, thus, demanding the need to accurately and efficiently measure mmWave instruments such as antennas. The surface roughness analysis of this work is not only helpful to this project but can be utilized by others to construct high frequency CATRs in other labs and facilities.

6.3 Future Work

The next step for the presented work would be testing upgrades for the system. Upgrades include different antennas, more absorbers, and improved calibration and alignment capabilities.

Alternative antennas can be investigated to decrease the magnitude variation in the QZ.

From simulation results, it is expected that a less directive feed antenna can realize lower magnitude ripples in the QZ. The literature explains that with the use of reflectors, it is important to situate absorbers behind the reflector. With the current setup, this is not doable. The ideal setup would be housing the system inside a concealed chamber lined with absorbers, rather than in an open room. Another limitation of the current system is that the current positioners of the system do not meet the precision that is seen in professionally manufactured CATRs. This is likely introducing errors in the alignment and calibration that is shown to significantly affect the purity of the QZ. Upgrading the UR3 to a different instrument would allow for more control and better alignment. With system upgrades the limitations of the reflector itself can be better determined.

Although the 3D printing method was effective for the currently manufactured reflectors, the metallic coating strategies could be improved. Further analysis can be done to improve the copper tape application, or perhaps one could explore copper foil as an option to eliminate seams. Copper plating was proven to have more than acceptable surface roughness, but this was not tested on a full-body reflector in this thesis. A future rendition of this project could copper plate the reflector instead of employing copper tape or silver paint.

Lastly, and perhaps most importantly, future work could include testing the current reflectors at higher frequencies. This work proves their validity up to 34 GHz, but system modifications could allow them to be tested up to and beyond W-band.

Therefore, there is potential to build upon the already completed work and maximize the capability of the reflector and system. Much of this venture has been completed and been a success, but improvements can be made to achieve even more favorable results available with this reflector design and at higher frequencies.

References

[1] J. A. Stine and D. L. Portigal, "Spectrum 101: An introduction to spectrum management," 2004.

[2] M. J. Marcus, "Spectrum policy for radio spectrum access," *Proceedings of the IEEE*, vol. 100, no. Special Centennial Issue, pp. 1685–1691, 2012. DOI: 10.1109/JPROC.2012.2187132.

[3] M. Rebato, F. Boccardi, M. Mezzavilla, S. Rangan, and M. Zorzi, "Hybrid spectrum access for mmwave networks," in *2016 Mediterranean Ad Hoc Networking Workshop (Med-Hoc-Net)*, 2016. DOI: 10.1109/MedHocNet.2016.7528417.

[4] A. Bhuyan, M. Ji, X. Zhang, S. K. Kasera, and S. Sarkar, "Secure mmwave spectrum sharing with autonomous beam scheduling for 5G and beyond," in *2022 IEEE 22nd Annual Wireless and Microwave Technology Conference (WAMICON)*, 2022. DOI: 10.1109/WAMICON53991.2022.9786167.

[5] M. D. Foegelle, "Testing mmwave phased arrays for the 5G new radio," in *2019 Antenna Measurement Techniques Association Symposium (AMTA)*, 2019. DOI: 10.23919/AMTAP.2019.8906488.

[6] M. W. Shields, "The compact RCS / antenna range at MIT Lincoln Laboratory," *2009 3rd European Conference on Antennas and Propagation*, pp. 939–943, 2009. [Online]. Available: https://api.semanticscholar.org/CorpusID:14120393.

[7] M. D. Foegelle, "Validation of CATRs for 5G mmwave OTA testing applications," in *2021 15th European Conference on Antennas and Propagation (EuCAP)*. DOI: 10.23919/EuCAP51087.2021.9411217.

[8] C. A. Balanis, *Antenna Theory: Analysis and Design, 3rd Edition*. Wiley, 2005.

[9] Z. Sun, S. Balakrishnan, L. Su, A. Bhuyan, P. Wang, and C. Qiao, "Who is in control? Practical physical layer attack and defense for mmwave-based sensing in autonomous vehicles," *IEEE Transactions on Information Forensics and Security*, vol. 16, pp. 3199–3214, 2021. DOI: 10.1109/TIFS.2021.3076287.

[10] O. Toker and S. Alsweiss, "Mmwave radar based approach for pedestrian identification in autonomous vehicles," in *2020 SoutheastCon*, 2020. DOI: 10.1109/SoutheastCon44009.2020.9249704.

[11] E. S. Gillespie, "A brief history of the compact range and the near-field range," *Proceedings of the 2001 IEEE Radar Conference (Cat. No.01CH37229)*, pp. 436–439, 2001.

[12] A. D. Olver, "Compact antenna test ranges," 1991. [Online]. Available: https://api.semanticscholar.org/CorpusID:108866846.

[13] W. L. Stutzman and G. A. Thiele, *Antenna Theory And Design. 3rd Edition*. John Wiley & Sons, 2012.

[14] T. Cleford. "Let's talk about reflector antennas." (), [Online]. Available: https://swamphen.co.uk/new-blog/2019/4/15/lets-talk-about-reflector-antennas (visited on 08/15/2023).

[15] T. Clelford, *Let's talk about reflector antennas*, Last accessed 16 August 2023, 2021. [Online]. Available: https://swamphen.co.uk/new-blog/2019/4/15/lets-talk-about-reflector-antennas.

[16] J. Huang and J. A. Encinar, *Reflectarray Antennas*. John Wiley & Sons, 2008.

[17] Z. Li, P. Huo, Y. Wu, and J. Wu, "Reflectarray compact antenna test range with controlled aperture disturbance fields," *IEEE Antennas and Wireless Propagation Letters*, vol. 20, no. 7, pp. 1283–1287, 2021. DOI: 10.1109/LAWP.2021.3077739.

[18] C. Granet, M. Zhou, S. B. Sørensen, K. W. Smart, J. S. Kot, and J. Ness, "Reflectarray compact antenna test range concept," in *2019 13th European Conference on Antennas and Propagation (EuCAP)*, 2019, pp. 1–5.

[19] O. Borries, P. Meincke, E. Jørgensen, H. H. Viskum, and F. Jensen, "Design and validation of compact antenna test ranges using computational EM," 2015. [Online]. Available: https://api.semanticscholar.org/CorpusID:209352955.

[20] V. Schirosi, F. Saccardi, A. Giacomini, *et al.*, "Accurate antenna characterisation at VHF/UHF frequencies with plane wave generator systems," 2023. [Online]. Available: https://api.semanticscholar.org/CorpusID:115526796.

[21] W. D. Burnside, M. Gilreath, and B. Kent, "Rolled edge modification of a compact range," *Proc. of 1984 AMTA Sym.*, 4B3–1, 1984.

[22] W. D. Burnside, Dominek, and R. Barger, "Blended surface concept for compact range reflector," *Proc. 1985 AMTA Sym.*, pp. 10–1, 1985.

[23] T.-H. Lee and W. Burnside, "Performance trade-off between serrated edge and blended rolled edge compact range reflectors," *IEEE Transactions on Antennas and Propagation*, vol. 44, no. 1, pp. 87–96, 1996. DOI: 10.1109/8.477532.

[24] T.-H. Lee and W. Burnside, "Compact range reflector edge treatment impact on antenna and scattering measurements," *IEEE Transactions on Antennas and Propagation*, vol. 45, no. 1, pp. 57–65, 1997. DOI: 10.1109/8.554241.

[25] I. J. Gupta, D. G. Brown, W. D. Burnside, and W. Lin, "A method to design blended rolled edges for compact range reflectors," *IEEE Transactions on Antennas and Propagation*, vol. 38, no. 6, pp. 853–861, 1990. DOI: 10.1109/8.55582.

[26] I. J. Gupta, P. Ericksen, and W. D. Burnside, "A serrated edge gregorian subreflector for dual chamber compact range systems," *IEEE Transactions on Antennas and Propagation*, vol. 39, no. 8, pp. 1258–1261, 1991. DOI: 10.1109/8.97369.

[27] I. J. Gupta and W. D. Burnside, "Compact range measurement systems for electrically small test zones," *IEEE Transactions on Antennas and Propagation*, vol. 39, no. 5, pp. 632–638, 1991. DOI: 10.1109/8.81491.

[28] I. J. Gupta, "Analysis of serrated edge compact range reflectors," 2003. [Online]. Available: https://api.semanticscholar.org/CorpusID:221684711.

[29] H. F. Schluper, "Verification method for the serration design of CATR reflectors," 2003. [Online]. Available: https://api.semanticscholar.org/CorpusID:221684711.

[30] E. B. Joy and R. E. Wilson, "Shaped edge serration for improved compact range performance," *Proc. 1987 AMTA Sym.*, p. 55, 1987.

[31] NSI-MI. "Compact range reflectors." (2023), [Online]. Available: https://www.nsi-mi.com/products/compact-range-reflectors (visited on 01/30/2024).

[32] M. Dirix and S. F. Gregson, "Optimisation of the serration outline shape of a single offset-fed compact antenna test range reflector using a genetic evolution of the superformula," in *2021 15th European Conference on Antennas and Propagation (EuCAP)*, 2021, pp. 1–5. DOI: 10.23919/EuCAP51087.2021.9411036.

[33] T. V. R. Krishna, P. Siddaiah, and B. P. Rao, "Performance analysis of CATR reflector with segmented triangular serrated edges," in *2007 IET-UK International Conference on Information and Communication Technology in Electrical Sciences (ICTES 2007)*, 2007, pp. 991–995.

[34] A. Muñoz-Acevedo, M. Sierra-Castañer, and J. L. Besada, "Antenna measurement system operating at W and J millimeter wave bands," in *35th International Conference on Infrared, Millimeter, and Terahertz Waves*, 2010, pp. 1–2. DOI: 10.1109/ICIMW.2010.5612729.

[35] "IEEE recommended practice for antenna measurements," *IEEE Std 149-2021 (Revision of IEEE Std 149-1977)*, pp. 1–207, 2022. DOI: 10.1109/IEEESTD.2022.9714428.

[36] C. Parini, S. Gregson, J. McCormick, and D. Janse van Rensburg, *Theory and Practice of Modern Antenna Range Measurements*. London: Institution of Engineering and Technology, 2014.

[37] S. Gregson and C. Parini, "Examination of the effect of common CATR quiet zone specifications on antenna pattern measurement uncertainties," in *Loughborough Antennas & Propagation Conference (LAPC 2017)*, 2017. DOI: 10.1049/cp.2017.0276.

[38] "IEEE recommended practice for radar cross-section test procedures," *IEEE Std 1502-2020 (Revision of IEEE Std 1502-2007)*, pp. 1–78, 2020.

[39] D. W. Hess, "Introduction to RCS measurements," in *2008 Loughborough Antennas and Propagation Conference*, 2008, pp. 37–44. DOI: 10.1109/LAPC.2008.4516860.

[40] F. Amin, A. Mueed, and J.-d. Xu, "Implementation and results of an RCS measurement system in CATR," in *2012 IEEE Asia-Pacific Conference on Applied Electromagnetics (APACE)*, 2012, pp. 262–267. DOI: 10.1109/APACE.2012.6457673.

[41] Rohde and Schwarz. "Compact 3GPP-compliant OTA chamber for 5G NR mmwave signals." (2023), [Online]. Available: https://www.rohde-schwarz.com/uk//products/test-and-measurement/antenna-test-systems-and-ota-chambers/rs-ats1800c-compact-3gpp-compliant-ota-chamber-for-5g-nr-mmwave-signals_63493-687744.html (visited on 03/31/2024).

[42] T. A. Milligan, *Modern antenna design*. Wiley-IEEE Press, 2005.

[43] N. Aboserwal, C. Balanis, and C. Birtcher, "Conical horn: Gain and amplitude patterns," *Antennas and Propagation, IEEE Transactions on*, vol. 61, pp. 3427–3433, Jul. 2013. DOI: 10.1109/TAP.2013.2256453.

[44] J. J. Jansen, M. M. Jeuken, and C. C. Lambrechtse, "The scalar feed," 1969. [Online]. Available: https://api.semanticscholar.org/CorpusID:122695795.

[45] A. F. Kay, "The scalar feed," *AFCRL Rep. 64 - 347, AD601609*, 1964.

[46] C. W. I. Pistorius, "New main reflector, subreflector and dual chamber concepts for compact range applications," 1986. [Online]. Available: https://api.semanticscholar.org/CorpusID:107891186.

[47] C. W. I. Pistorius and W. D. Burnside, "The design of blended rolled edges for compact range main reflectors," in *5th International Conference on Antennas and Propagation*, 1987, pp. 391–394.

[48] S. Ellingson, I. Gupta, and W. Burnside, "Analysis of blended rolled edge reflectors using numerical UTD," *IEEE Transactions on Antennas and Propagation*, vol. 38, no. 12, pp. 1969–1971, 1990. DOI: 10.1109/8.60989.

[49] G. L. James, G. Tong, and D. A. Ross, "Uniform diffraction solution for a discontinuity in curvature," *Electronics Letters*, vol. 11, pp. 557–559, 1975. DOI: 10.1049/el:19750426.

[50] T. Chu, "First order uniform theory of diffraction analysis of the scattering by smooth structures," PhD thesis, The Ohio State University, 1982.

[51] C. Pistorius and W. Burnside, "An improved main reflector design for compact range applications," *IEEE Transactions on Antennas and Propagation*, vol. 35, no. 3, pp. 342–347, 1987. DOI: 10.1109/TAP.1987.1144101.

[52] A. K. Singh, J. Thakur, and R. K. Samminga, "Surface tolerance analysis of offset reflector antenna in Ku-band," in *2021 6th International Conference for Convergence in Technology (I2CT)*, 2021, pp. 1–6. DOI: 10.1109/I2CT51068.2021.9418130.

[53] S. Adibelli, P. Juyal, and A. Zajic, "On the surface roughness and smoothing in the 3D printed THz reflectors," in *2019 IEEE International Symposium on Antennas and Propagation and USNC-URSI Radio Science Meeting*, 2019, pp. 593–594. DOI: 10.1109/APUSNCURSINRSM.2019.8889264.

[54] S. Zhang and B. Duan, "Random error characterization of nonsmooth parabolic reflector antennas with gore-faceted or discontinuous surface," *IEEE Transactions on Antennas and Propagation*, vol. 69, no. 4, pp. 1922–1930, 2021. DOI: 10.1109/TAP.2020.3026870.

[55] K. Pontoppidan and S. SØrensen Busk, "Shaped beam antenna- reflector surface tolerance effects," TICRA, Kronprinsensgade 13, Copenhagen K, Denmark.

[56] K. Pontoppidan, "Shaped beam antenna- reflector surface tolerance effects," TICRA, Kronprinsensgade 13, Copenhagen K, Denmark.

[57] A. Repjar and D. Kremer, "Accurate evaluation of a millimeter wave compact range using planar near-field scanning," *IEEE Transactions on Antennas and Propagation*, vol. 30, no. 3, pp. 419–425, 1982. DOI: 10.1109/TAP.1982.1142800.

[58] P. Nielson, T. Rubæk, and H.-H. Viskum, *Random surface distortion in GRASP*, 2020. [Online]. Available: https://www.ticra.com/wp-content/uploads/2020/10/Random-surface-distortion-in-GRASP_White-paper.pdf.

[59] J. Ruze, "The effect of aperture errors on the antenna radiation pattern," *Il Nuovo Cimento (1943-1954)*, vol. 9, pp. 364–380, 1952. [Online]. Available: https://api.semanticscholar.org/CorpusID:121735671.

[60] M. Zarghamee, "On antenna tolerance theory," *IEEE Transactions on Antennas and Propagation*, vol. 15, no. 6, pp. 777–781, 1967. DOI: 10.1109/TAP.1967.1139044.

[61] D. Cheng, "Effect of arbitrary phase errors on the gain and beamwidth characteristics of radiation pattern," *IRE Transactions on Antennas and Propagation*, vol. 3, no. 3, pp. 145–147, 1955. DOI: 10.1109/TAP.1955.1144300.

[62] J. Ruze, "Antenna tolerance theory—a review," *Proceedings of the IEEE*, vol. 54, no. 4, pp. 633–640, 1966. DOI: 10.1109/PROC.1966.4784.

[63] Y. Rahmat-Samii, "An efficient computational method for characterizing the effects of random surface errors on the average power pattern of reflectors," *IEEE Transactions on Antennas and Propagation*, vol. 31, no. 1, pp. 92–98, 1983. DOI: 10.1109/TAP.1983.1142978.

[64] J. L. Salazar-Cerreno, Z. Qamar, and N. Aboserwal, "A multipurpose and reconfigurable mm-wave scanner system for accurate measurements of passive/active antenna array, array calibration, radome and material characterization," in *2021 IEEE Conference on Antenna Measurements & Applications (CAMA)*, 2021, pp. 555–559. DOI: 10.1109/CAMA49227.2021.9703579.

[65] C. M. Technologies. "S5243 2-port 44 GHz analyzer." (), [Online]. Available: https://coppermountaintech.com/vna/s5243-2-port-44-ghz-analyzer/ (visited on 02/27/2024).

[66] C. M. Technologies. "CobaltFx FEV-10 frequency extension system, 75 to 110 GHz." (), [Online]. Available: https://coppermountaintech.com/frequency-extension/cobaltfx-fev-10-frequency-extension-system-75-to-110-ghz/ (visited on 02/27/2024).

[67] VELMEX. "Velmex precision motion-control and positioning equipment." (2016), [Online]. Available: https://www.velmex.com/Products/index.html (visited on 02/27/2024).

[68] U. Robots. "UR3e." (2024), [Online]. Available: https://www.universal-robots.com/products/ur3-robot/ (visited on 02/27/2024).

[69] M. V. Group. "Standard gain horns." (), [Online]. Available: https://www.mvg-world.com/en/products/antennas/reference-antennas/standard-gain-horns (visited on 04/01/2024).